2019

PERCEPTION OF WHEELED MOBILE ROBOTS IN AGRICULTURE: PHENOTYPING AND MOBILITY ASSESSMENT

YANDUN NARVAEZ, FRANCISCO JAVIER

Universidad Técnica Federico Santa María

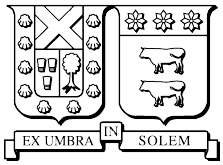

Doctoral Thesis

Perception of Wheeled Mobile Robots in Agriculture: Phenotyping and Mobility Assessment

Author:
Francisco Javier Yandun Narvaez

Supervisor:
Prof. Dr. Fernando Auat Cheein

A thesis submitted in fulfilment of the requirements for the degree of Doctor of Philosophy in Electronics

in the

Department of Electronic Engineering

April 2, 2019

Declaration of Authorship

I, Francisco Javier Yandun Narvaez, declare that this thesis titled, "Perception of Wheeled Mobile Robots in Agriculture: Phenotyping and Mobility Assessment" and the work presented in it are my own. I confirm that:

- This work was done wholly or mainly while in candidature for a research degree at this University.
- Where any part of this thesis has previously been submitted for a degree or any other qualification at this University or any other institution, this has been clearly stated.
- Where I have consulted the published work of others, this is always clearly attributed.
- Where I have quoted from the work of others, the source is always given. With the exception of such quotations, this thesis is entirely my own work.
- I have acknowledged all main sources of help.
- Where the thesis is based on work done by myself jointly with others, I have made clear exactly what was done by others and what I have contributed myself.

Signed: _____

Date: _____

Abstract

Agricultural production must double by 2050 in order to meet the expected food demand due to population growth. Within the technologies employed and developed to achieve this goal, research on development of intelligent automated or semi-automated mobile robots capable to navigate in agricultural scenarios acquiring physiological data about the plants has proven to produce successful results in terms of efficiency and productivity. In these vehicles, environmental perception is a keypoint to obtain information not only about the crops, but also about their surroundings and the mobility status of the robot itself. Within this sensing problem, two perspectives are identified: agricultural and robotics. The first considers the robot sensors as means to measure or estimate diverse parameters of the plants, in a phenotyping scheme. The robotics perspective, on the other hand, aims to use the acquired information for the robot navigation. This Thesis provides a comprehensive study and real applications of both perspectives.

Sensors that can be mounted on a robot and used for crop phenotyping are first reviewed and two specific tests cases are presented. Both provide novel applications for structural and physiological assessment of crops. The first studies the effects of using incomplete data acquired from a 2D laser range finder to estimate the treetop volume of fruit trees. The other application case presents the development and validation of a sensor fusion methodology to get 3D and thermal representations of trees. The final result is a point cloud where each point has a temperature value associated, providing a tool to jointly assess structural and physiological parameters of the tree.

The robotics perspective focuses on the characterizing the terrain and its effects on the mobility of the vehicle. As agricultural environments are in general off-road, traversability of the robot can easily become tough and dangerous. Terrain perception is then studied using descriptive and dynamic approaches. It is proposed a terrain classification system to first descriptively characterize the terrain in front of the robot. As the total cost of the solution is an important matter for commercial adoption, a low cost sensor was employed. The proposed implementation showed to be robust in field testing with changing illumination conditions, yielding high accuracy rates.

The dynamic terrain characterization is addressed by off-line identifying a kinematic model that accounts for non-zero slippage. The parameters of this model are considered as random variables whose posterior distributions are approximated using a Particle Markov Chain Monte Carlo method. Contrary to traditional approaches where punctual estimations are obtained, this point of view can enable a probabilistic motion assessment with uncertainty propagation not only to the robot positioning but also to other variables (e.g., wheel slip velocities). Extensive simulation and experimental tests were used to validate and to compare the proposed methodology with the Integrated Perturbation Error Dynamics approach. Results showed that the proposed methodology provides specially satisfactory results when driving an earthmoving machine through changing terrains.

Acknowledgements

When this adventure began, it was a mixture of emotions and feelings. I left home with my baggage full of dreams and excitement, but also with a little uncertainty of the things that may happen. Over time, the great atmosphere in the work group, along with the people outside work make these uncertainties to disappear and make Chile my new home. Certainly, all the time shared so far have made me grow as professional and human being. In the next few lines I will express my gratitude to people that made this years a really great time.

First of all, I would like to acknowledge my advisor, Prof. Dr. Fernando Auat Cheein for the guidance and support through this postgraduate. In the professional side, he is the best advisor that a student can get. Thank you for sharing your ideas with all the group, we know that your ideas are one of your most valued assets. Also, thank you for expending a lot of time teaching me all of the things that you think a top level researcher have to know about the scientific method and the publication world. I know that some things I have to learn by myself, but your guidance would make everything easier. In the personal side, for me, you are more than an advisor that one can only talk about academic stuff, you are a friend to whom I can talk about my daily life and problems. Thank you for the time you put in this aspect of my education. I am sincerely happy to have been your student and to be your friend.

In these years, I had the privilege to work with fantastic researchers in various topics. I want to thank to Jaime Salvo for his support and guidance in the agricultural stuff, Prof. Miguel Torres-Torriti, for his review and point of view in all the papers we have together, Prof. Andrés Rosales to build the bridge between the Escuela Politécnica Nacional and the UTFSM. I also would like to mention Prof. Joan-Ramón and all the research group in AgroICT & Precision Agriculture of the University of Lleida. The time I spent there was very productive and valuable. In the same way, I am very grateful with Prof. George Kantor and the opportunity he gave me to visit the Carnegie Mellon University and to work with his group. The three months I spent in the US were very interesting, rewarding and productive in several ways.

My friends in Chile are one of the most valued things I have. I know that we will take different roads in life, but the ties we made will last for life. Oswaldo and Javier, we almost started this adventure together and the friendship we built among this years is essential part of the achievement I made. It was always nice talk to you about almost any topic that can come across. I also have to mention Robert, Daniel and Felipe, we all have built a group that is always there for playing soccer, drinking a beer or simply talking about our lives. The Ecuadorian community in the UTFSM has also my affection and gratitude, it was always important to share moments with all of you guys. Thanks also to the Chilean friends I made during this time, your reception to me was specially valuable.

My family has also my gratitude for their support and care during these years. My dad, mom, sisters and brother are cornerstones of all my triumphs. Specially you dad, I miss you everyday. I want to also say a big thank you to my grandma and aunts, Abelita, Nani and Rosi, you are angels that guide my way in life. My nieces and nephews are also important part of my life, thank you little ones.

My beloved wife Carolina has my deepest gratitude and love. Her encouragement and selfless support were very important, especially for the final part of this thesis. I love you!

Finally, I also want to acknowledge the institutions that made this possible. In first place, to the Universidad Técnica Federico Santa María, for granting foreign people to study there. *Don* Federico Santa María Carrera would be proud to see the institution he created as educator of human talent with social vision. Furthermore, the teachers of the university has also my deepest gratitude. I also express my gratitude to the National Commission of Scientific and Technological Research (CONICYT) for the grant CONICYT- PCHA/Doctorado Nacional/2015-21150694. The support of Chile and its people through this grant is sincerely appreciated.

Contents

List of Figures

List of Tables

List of Abbreviations

PA	**P**recision **A**griculture
ToF	**T**ime **o**f **F**light
LiDAR	**Li**gth **D**etection and **R**anging
2D	Two **D**imensional
3D	Three **D**imensional
RGB	**R**ed **G**reen and **B**lue
MRF	**M**arkov **R**andom **F**ield
ICP	**I**terative **C**losest **P**oint
IRGA	**I**nfra-red **G**as **A**nalyser
ICE	**I**mage **C**omposite **E**ditor
MR8	**M**aximum **R**esponse 8 filter bank
ROI	**R**egion of **I**nterest
SVM	**S**upport **V**ector **M**achine
UTFSM	**U**niversidad **T**écnica **F**ederico **S**anta **M**aría
SMC	**S**equential **M**onte **C**arlo
SSM	**S**tate **S**pace **M**odel
iid	**i**ndependent and **i**dentically **d**istributed
a.s.	**a**lmost **s**ure
JSD	**J**oint **S**moothing **D**ensity
IS	**I**mportance **S**ampling
MCMC	**M**arkov **C**hain **M**onte **C**arlo
MH	**M**etropolis **H**astings
EM	**E**xpectation **M**aximization
SMC	**S**equential **M**onte**C**arlo
PMCMC	**P**article **M**arkov **C**hain **M**onte **C**arlo
CPF-AS	**C**onditional **P**article **F**ilter with **A**ncestor **S**ampling
PGAS	**P**article **G**ibbs with **A**ncestor **S**ampling
FR, FL	**F**ront **R**ight, **F**ront **L**eft
RR, RL	**R**ear **R**ight, **R**ear **L**eft
IPEM	**I**ntegrated **P**erturbation **E**rror **M**inimization
cpv	**c**ontact **p**oint **v**elocity

List of Symbols

x	Scalar variable
$\boldsymbol{x}$	Vector-valued variable
Ω	Set of points forming a cloud
δ	Step criterion to segment a point cloud
z_{max}	Maximum value in the z coordinate
z_{min}	Minimum value in the z coordinate
$p\,(t)$	Pitch angle estimated with regression at time t
$v\,(t)$	Voltage measured at time t
p_s	Smoothed pitch estimation
$T\,(x, y)$	Temperature of a pixel located at x,y on a thermal image
T_{max}	Maximum temperature measured
T_{min}	Minimum temperature measured
$I\,(x, y)$	Intensity value of a pixel located at x,y on an image
S	Region of interest in an image
l_i	Label assigned to the ith sample
f	State transition model
g	Measurement transition model
f	State transition density
g	Measurement transition density
$\mu(\boldsymbol{x_1})$	Distribution of an initial state
$\boldsymbol{\gamma}$	Parameter vector
$\xi(\boldsymbol{x})$	Target density
$\delta(\boldsymbol{x} - \boldsymbol{x}^{(i)})$	Dirac delta located at $x^{(i)}$
$w(\boldsymbol{x})$	Weighting function in an importance sampler
$\boldsymbol{x}_t^{(i)}$	Particle i at time t
$a_t^{(i)}$	Ancestor index of particle i at time t
Γ	Vector space spanned by the parameter values admissible for the non-zero slipping model
$\pi(\boldsymbol{\gamma})$	Prior distribution of the parameters
${}^c\boldsymbol{r}_a^b$	Position of a coordinate frame a relative to a frame b, expressed in coordinates of frame c
$\boldsymbol{r}_a^b$	Position of a coordinate frame a relative to a frame b, expressed in global coordinates
δt	Sample time
V	Linear velocity
ω	Angular velocity
Δs	Distance travelled

To my parents, brother and sisters, my achievements are yours.

Chapter 1

Introduction

Agriculture is one of the most important activities in the primary sector of the economy since it provides much of the incomes in many countries. Various years of manual labour contributed to develop empirical techniques to manage the soil and crops during the agricultural cycle (i.e., soil treatment, seeding, growing, crop dosage and harvesting). Traditional agriculture has evolved passing this expertise from one farmer to other, providing successful results from ancient times to present. However, in the last decades, a remarkable shift from this traditional paradigm to a technology-based one has been produced, mainly as consequence of three factors. The first consists in the migration of the labour force from the field to the industry since it provides better working conditions and wages. The second is marked by the evolution of trading standards in the world markets, which requires quantitative metrics to assess the conditions of the crop during the seeding, growth and harvesting. Precisely, the development of new and cheaper sensors brought a solution to this requirement, giving numerical indicators for some important variables of the crops and orchards during all these stages. The last factor is well related to the second one: a continuous increasing in both the competitiveness of the markets and the production rates. This requires, among other things, an efficient way to manage the crops without losing the quality of the products. In this way, the use of sensing devices to estimate the physiological status of the plants (phenotyping) and the conditions of the farming field (e.g., the work environment or the soil) have been widely adopted, at the point that now it is almost a necessity in medium and large farms. The conjunction of the last two points marked the development of remote and proximal sensing approaches, while the first leads the search for solutions in form of automated or semi-autoamted robotic vehicles also called *Service Units*, capable to perform supervision or execution activities in field, mostly in presence of human workers. In fact, the fields of the technology which focuses on studying and proposing enhancements for agriculture sensing and service units, along with the research of a satisfactory coupling of both, are AgroICT (Information and Communication Technologies for Agronomy and the Environment) and *Precision Agriculture*.

1.1 Precision Agriculture Implications

Precision Agriculture (PA) has evolved towards an information approach, whose aim is to acquire as much data from the crop as possible to perform a customized crop management (Mulla, 2013). Thus, PA could be seen like a big control strategy, where the machinery and the farm workers are the actuators that maintain a sustainable and

profitable production. The farmers, on the other hand, are in charge of taking the control actions according to both the production needs and the environmental care. The sensing of the crop or the farm fields allows to collect the information about its status, providing the loop feedback and therefore the loop closure. The latter is a cornerstone of any information process, since it provides the means to acquire data upon which any action can be performed. This interpretation is schematically depicted in Fig.1.1. This thesis studies the coupling of two key elements of the PA control loop:

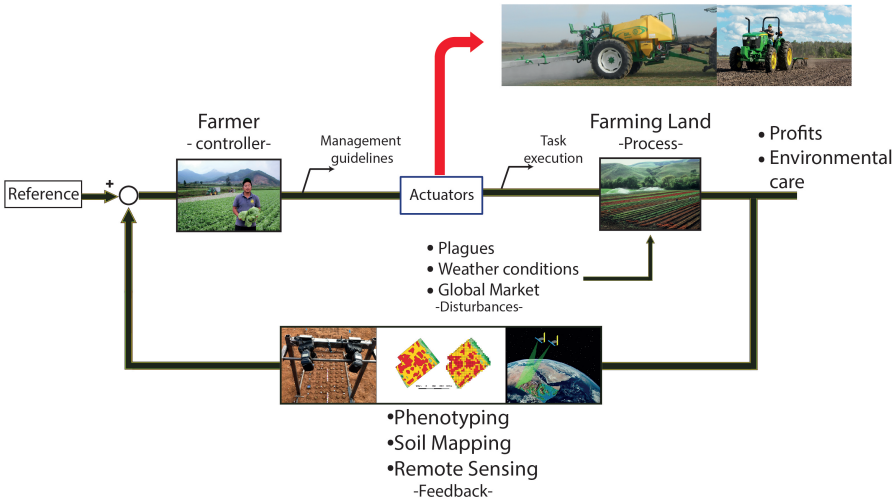

FIGURE 1.1: Interpretation of precision agriculture in a control loop scheme.

the loop feedback (i.e., agricultural perspective), and the perception of the actuators (i.e., robotics perspective). The aim is to provide scene understanding capabilities of plant phenotypting and autonomous navigation for robotised service units. In this context, the problem can be divided twofold: about the vehicle's surroundings -above the ground- (e.g., vegetation and worker detection, phenotyping); and about the terrain on which the service unit moves (e.g., traction and mobility assessment). This demarcation allows to establish a clear partition in the studied and proposed applications, both in the PA-robotics framework. The first one is associated with sensing aimed to agricultural applications; whereas the other is associated with the autonomy of mobile robots driving in off-road agricultural scenarios. In this thesis agricultural and mobility applications are studied separately but employing sensors and sensing systems which can be suitable for both. Furthermore, other sub-systems related to autonomy and navigation (e.g., planning or control) are not studied, but part of the methodologies proposed here are intended to work in conjunction with them.

1.2 State of the Art Review

In the 20th century, mechanization of the agriculture was considered one of the greatest engineering achievements by the US National Academy of Engineering (Reina et al., 2016). While this development was functional in the past, increasing of population, global markets dynamics and other social factors, have made necessary to take a step beyond towards automation. In this matter, perception of automated or

semi-automated machinery is certainly an important point which is being addressed by the scientific community. Following the perspectives described above, the literature reports a diversity of applications from the agronomic and the vehicle mobility point of view. The first are related with methodologies to use sensors and sensing systems for plant phenotyping. The mobility-related, on the other hand, are aimed to study the effects of the terrain on the robot motion, as well as on its performance (e.g., energy consumption or task execution). In the following, most of the important reports in each field are outlined.

1.2.1 Plant Phenotyping - Agricultural Perspective

Precision Agriculture technologies include a wide range of activities such as yield monitoring, geo-referenced and high resolution soil assessment, crop phenotyping, among others. The use of specific methodologies depends on the labour where they will be applied and the resources available. For example, the advantage of using drones for covering larger areas contrasts with the lack of resolution to analyse individual plants or trees. In the PA-robotics framework adopted in this thesis, the application that best suits is proximal crop phenotyping. Sensing devices which can be placed on a terrestrial robot or farming machinery (a service unit, in general) allow to assess the status of the crops and plants in several ways (Gil et al., 2013; Nuske et al., 2014). However, the morphology and physical description (e.g., volume, leaf area index, reflectance) have arisen as widely used parameters for these purposes, as reported by Rosell and Sanz, 2012. The non-invasive and non-destructive framework of crop sensing and characterizing in terms of these two features (morphology and physical description) provides a suitable approach for evaluating the vegetation conditions. Thus, three main applications can be recognized for agricultural phenotyping:

- Structural characterization: the estimation of parameters such as: canopy volume, plant height, leaf area coverage, biomass, among others, leads to take decisions for enhancing the agricultural process. For example, canopy volume has been used to improve the spraying of phytosanitary products (i.e., pesticides and fertilizers) on fruit trees in terms of inputs saving and environmental costs (Chen, Zhu, and Ozkan, 2012; Escolà et al., 2013). Additionally, the leaf area coverage has been used for crop growth monitoring and yield estimation since it reflects many aspects of the physiological processes of vegetation (Mora et al., 2016). In a similar vein, gap fraction of the canopy (sometimes called "porosity") is used as an indicator of the amount of solar radiation received by the vegetation (Welles and Cohen, 1996; Arriagada Pfeiffer et al., 2018). Furthermore, biomass mapping and monitoring provide the means for detecting changes in the plantation status due to storms, drought or plagues (Eitel et al., 2014; Li et al., 2016b). Since bio-energy obtained from specific crops has become one of the most frequently used power sources, estimating its biomass also arises as a productivity evaluation parameter (Kankare et al., 2013).

- Plant/Fruit detection: successful results in automated activities such as pruning, harvesting, seeding, among others, depend on an accurate localization of the object of interest within the environment (see for example the work of Bac et al., 2014 and the references therein). To achieve this aim, several features

and properties of plants and fruits have been used, namely: color, shape and temperature (Gongal et al., 2015). In robotic fruit harvesting, color or temperature are attributes which can be used to identify the product within the canopy (Ji et al., 2012; Gongal et al., 2016) or in the crop field (Foglia and Reina, 2006). Moreover, for automatized robotic pruning, the shape of the stems is the feature which in most cases provides the cutting directives, as reported by Karkee et al., 2014.

- Physiology assessment: the physical response of the canopy to sunlight results in characteristic spectral signatures, which provide insights about the physiological status of the plant. In this way, several indices based on the spectral responses of the crop have been developed to assess parameters such as: nitrogen deficiencies, chlorophyll concentration, water stress, pest infestation, among others(Jones et al., 2009; Du et al., 2016). Additionally, other sensing devices (e.g., Infra-red gas analyzers) provide the means to measure directly a number of physiological parameters of the plants. Much of them require a direct contact with the crop, which results in more accurate readings. However, the measuring process follows an individualized path, which makes this approach time consuming in most cases (Weerakkody and Suriyagoda, 2015).

A broad classification of the sensors based on the previously discussed applications is graphically depicted in Figure 1.2. The versatility of these sensing devices to be mounted in service units with various configurations makes them specially suitable for field applications such as agriculture. In the following, a brief description of their operating principles is provided, as well as the main agricultural applications reported in the literature.

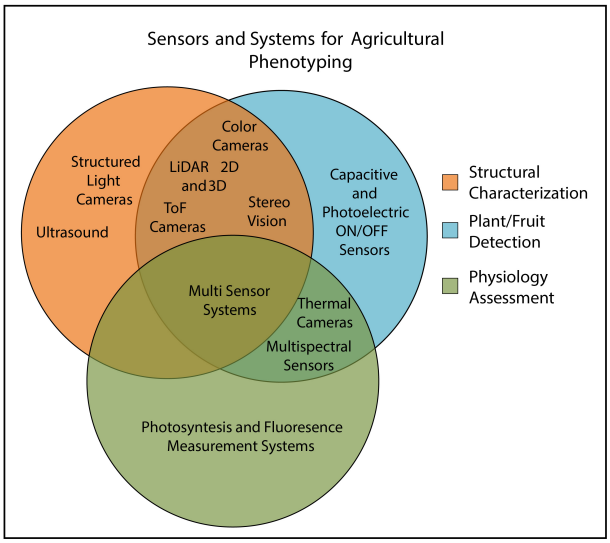

FIGURE 1.2: Applications and sensors for morphological characterization, detection of plants and physiology assessment. (Yandun et al., 2017) © 2017 IEEE.

Range Sensors

- Ultrasound: This type of sensor works by emitting an acoustic pulse of high frequency and short duration which propagates trough the air, impacts to the target and returns in form of echo. Electronics inside the sensor calculates the distance based on the time between the emission of the sound and receiving the echo signal. Ultrasonic sensors were widely used in the past, but the improvement and cost reduction of other sensing technologies have made their use less common. In this scenario, according to Tumbo et al., 2002, there are some important drawbacks that made ultrasonic sensors less competitive when compared with similar sensors (e.g., laser range finders): (i) when impacting against tilted surfaces, the sound diverts causing inaccuracies in the measurements; (ii) the interference produced when using sensors very close to each other, (iii) the measurement resolution, and (iv) the relatively slowness of sampling. However, the main advantages of this sensor are its low price and its robustness against fog and dust.

  Despite of the disadvantages of this sensor, several works report its application to estimate geometric parameters of the crop such as volume, density, height width, among others. Specifically, Palleja and Landers, 2015 proposed a real time system to estimate the canopy density on apple trees and grapevines using four ultrasonic sensors mounted on a tractor. Previous works used the same measurement framework for estimating tree volumes, which provided information to adjust the dosing parameters of automatic spraying machines (Escolà et al., 2011).

- Time of Flight (ToF) Cameras: This type of range sensor provides 3D measurements of distance and intensity by using an array of detectors and a source of light. Due to its capabilities of accuracy, compactness and frame rate these sensors have been used in diverse applications. Concretely, in agricultural research, the structural characterization and detection of plants or fruits have been addressed using these cameras. For example, Chaivivatrakul et al., 2014 and Alenyà, Dellen, and Torras, 2011 used a ToF camera for extracting geometrical variables of the plant that allow the modeling and monitoring of individual leaves. Both research works were carried indoors, in laboratory conditions, since field operation conditions (i.e., sunlight presence) often cause the saturation of the detectors, and therefore a poor measurement performance, as reported by Kazmi, Foix, and Alenyà, 2012.

  Incorporating color information provides important improvements for plant characterization and detection (Fig. 1.3). For example, the fusion of color and depth data to detect red sweet pepper in greenhouses is reported by Vitzrabin and Edan, 2016. The main processing is performed to RGB images; however, depth information was used to improve the detection accuracy, obtaining up to 90.9% of true positive rates when using natural light. Furthermore, Gongal et al., 2016 used depth and RGB cameras mounted in a mobile platform to acquire data in an over-the-row path within apple orchards. The sensing platform provided ideal illumination conditions so that the sensors would have good performance. The main processing of this work is performed on the color images, whereas depth information was used to filter duplicate detections; reporting up to 82%

of detection accuracy. Having color and depth images obtained by different sensors allows an improvement in characterization and detection; however, when both are given by a single sensor, the sensing scheme becomes smoother. In this way, Elfiky et al., 2015 reported the use of a videogaming device (capable of providing color, depth and intensity of reflectance) to obtain a 3D reconstruction and modelling of apple trees.

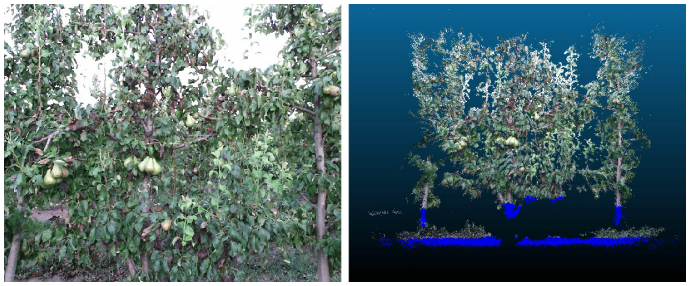

FIGURE 1.3: Color image and its corresponding colorized 3D point cloud acquired with a commercial Time of Flight camera in a pear orchard. The blue points represent the absence of color information due to the limited vertical field of view of the color camera. Image courtesy of the Research Group in AgroICT & Precision Agriculture, University of Lleida, Spain. (Yandun et al., 2017) © 2017 IEEE.

- Light Detection and Ranging (LiDAR): This is a non-destructive laser technology for measuring distances, which has been used in agricultural research to estimate structural parameters of the crop such as volume, leaf area coverage, height, among others (Sanz-Cortiella et al., 2011; Eitel et al., 2014). Within the LiDAR sensors, two types devices can be distinguished: 3D and 2D; however, the latter are more used since they are cheaper and can be employed to get 3D measurements (with the appropriate hardware). Moreover, according to the distance measuring method, there are two types of laser scanners: (i) Time of Flight LiDAR, which employs the time that takes to the laser pulse to travel between the sensor and the target; and (ii) Phase-Shift LiDAR, which uses the phase difference between the incident and reflected laser beams.

  The versatility for acquiring fast accurate measurements and quantifying the spatial variations of the vegetation have positioned LiDAR as a widely used sensing device for agricultural purposes. Terrestrial and aerial applications have been reported to classify vegetation in large scenes or to obtain a geometric description of the crop (Pueschel, Newnham, and Hill, 2014; Koenig et al., 2015). Regarding aerial applications, Fieber et al., 2013 reported the use of a full-waveform airborne laser scanner to classify orange trees, grass and ground based on the backscattering properties of the landscape. Additionally, Allouis et al., 2013 employed readings from a full waveform LiDAR to build allometric models for estimating the stem volume and biomass of individual pine trees. The authors compared these models with others which do not rely on the waveform information and found that this parameter does not have a positive influence in the volume estimations. However, the accuracy of the

biomass estimations was improved. Furthermore, the effects of the flying altitude and sensor configurations in the estimation of specific biophysical forestry parameters (i.e., Lorey's mean height and timber volume) of the canopies by using a small footprint aerial LiDAR are analised by Næsset, 2009. Slight differences in height and volume were found when varying the flying altitude, but they were significant when using multi-echo readings. It is noteworthy that aerial scanning has plenty of research in forestry, since the access for people and ground vehicles is difficult in such environments. Another advantage of this sensing method lays on the capability to characterize large portions of land with few samples or trials. Nevertheless, this quality becomes a drawback when the aim is to analyse the canopy beneath the treetop of the orchard. In such cases, terrestrial approaches are more suitable.

A number of research works report the use of point clouds obtained from 2D or 3D terrestrial LiDAR to infer structural information of the canopy, such as the volume, area, leaf density, branch dimensions, among others. Some of them took place in laboratory or controlled environments emphasizing the data processing techniques or the validation of new LiDAR-based technologies (Kankare et al., 2013; Du et al., 2016; Hétroy-Wheeler, Casella, and Boltcheva, 2016). However, once the method is validated in laboratory, the challenge lies in performing field experimentations. In order to sense large areas of the farm fields, laser scanners are usually placed on automatized or manually driven platforms, which allow the scanning of entire crops efficiently. In this way, a localization system, along with a 2D LiDAR mounted on such vehicles can be employed to generate a 3D point cloud of the environment, which can in turn be used to determine the structural variables of the canopy (Fig. 1.4). For example, the leaf area coverage of plum trees was estimated by Pforte, Selbeck, and Hensel, 2012, who used data from a 2D LiDAR placed in a tractor which offered a top view of the orchard . The results were compared with camera-based estimations, showing a strong correlation between both sensing systems. However, when comparing with hand-measured values, the correlation decreased in some extent, which implies that the proposed methodology could only partially describe the leaf area of the trees. Moreover, Sanz et al., 2013 described the relationship between canopy volume and leaf area density, both estimated from 3D data acquired applying the previously described measurement framework to vineyards, apple and pear trees. A non-linear relationship was obtained via logarithmic fitting of volume and leaf area estimations, obtaining a mean correlation coefficient of 0.87, and as high as 0.98 for the best case.

The use of moving 3D laser scanners have also been addressed for tree modelling. Particularly, Livny et al., 2010 reported the geometric modelling and reconstruction of urban trees skeletal structures. The authors used a method based on a series of global least squares optimizations in order to fit the points to the resulting graphs, and thus automatically reconstruct the skeletal structure of the trees. In contrast, placing the laser scanners (especially 3D LiDAR) at fixed positions also allows the inference of important characteristics of trees or field farms. Specifically, Koenig et al., 2015 used a full waveform 3D LiDAR for detecting post harvest grown in a winter barley farm. Using the reflectance of the field, the authors corrected the range measurements and obtained up to

99% accuracy. Further, Greaves et al., 2015 employed 3D data to estimate the biomass of low-stature Arctic shrubs. Regarding forestry applications, the detection of tree structural parameters (e.g., trunk diameter, leaf density) and biomass using LiDAR-based scanning systems mounted on a tripod have been studied with promising results (Kankare et al., 2013).

Due to the versatility and good performance of LiDAR sensors, several improvements (much of them still in development) have been proposed. Particularly, the most novel, and still under research is the so-called Hyperspectral LiDAR (HL). This equipment is intended to join the benefits of the classical laser scanners with the capability of recognize multiple wavelengths (Lin, 2015). The use of this sensor to agricultural applications have been studied by Wei et al., 2012, where it is used a HL to assess the status of vegetation in controlled environments. Results demonstrated the potential of using this type of LiDAR in spectral analysis of vegetation. Further, the estimation of parameters like nitrogen content (usually performed with spectral cameras or spectrometers) is possible with HL, as shown by Du et al., 2016 for rice leaves.

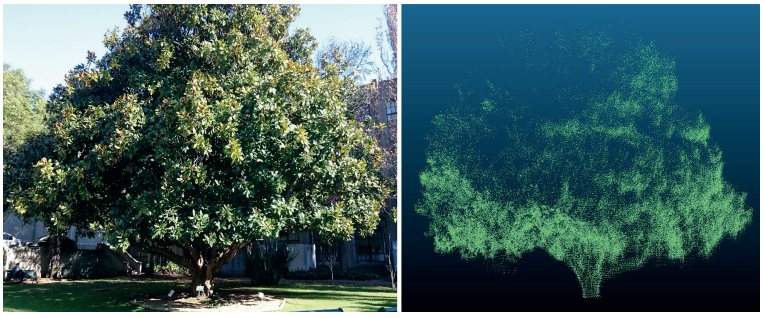

FIGURE 1.4: Color image of an ornamental tree and its corresponding 3D point cloud acquired with a moving 2D LiDAR. (Yandun et al., 2017) © 2017 IEEE.

Artificial Vision Sensors

- Structured Light Cameras: These sensors provide accurate measurement of distances by projecting an IR pattern over the scene and inspecting the distortion of the pattern received back. Since structured light cameras are intended to work indoors, agricultural research are mostly employed in laboratory conditions or greenhouses (Li et al., 2015). A leaf segmentation approach was employed by Chéné et al., 2012, who used data from a commercial structured light camera (originally designed for videogaming purposes). This work also provides several crop monitoring applications of the leaf segmentation method proposed. Furthermore, the same sensor has also been used for detecting structural parameters including size, height and volume. Concretely, the characterization of sweet onions and cauliflowers is proposed by Wang and Li, 2014 and Andújar et al., 2016, respectively. Results shown good consistency and accuracy in both cases, proving to be suitable methods for quality assessment and harvesting directives. However, in both works is stated that illumination conditions seriously affect the sensor performance. In addition, Rosell-Polo

et al., 2015 presented a complete description of the application of structured light cameras for a variety of agricultural and livestock purposes. This work provides a complete characterization of these sensors in changing illumination conditions (typical of farm fields), obtaining an inverse relationship between the number of points acquired and the illuminance received by the sensor.

- Color Cameras: Color cameras have been widely used in agricultural detection and characterization. From the color information provided, additional parameters such as texture and geometrical features can be also obtained, which have proved to be suitable in certain applications (e.g., detection, positioning, guidance). However, the main drawback of using this type of sensors is the influence of the varying ambient lighting conditions, especially in outdoor environments. Despite this fact, when the conditions are suitable, they have proved to perform well in field conditions. For example, the detection of fruits or vegetables within the canopy using color cameras can be applied in automated harvesting tasks. In this context, a recent work reported the use of a number of segmentation techniques based on color features and shape to detect immature green citrus (Zhao, Lee, and He, 2016). The results of this work showed an accuracy of 83.4% in the detection of 308 units, which is promising taking into account that the dataset was acquired with different illumination conditions. Furthermore, a real time guidance system for apple harvesting was developed by Ji et al., 2012. In this work, color and shape features extracted from color images were used along with a supervised classifier, which resulted in 89% of successful detections. Additionally, a color camera with artificial illumination was used by Nuske et al., 2014 to present a system capable of detecting berries in a vineyard, for later estimating the yield of the crop. Results showed a high amount of true positive detections and the yield prediction with an error of maximum 11.5%.

  Other classification and characterization activities also report the use of color cameras as the main sensing device. For example, a camera placed on an aerial vehicle was used by Fieber et al., 2013 to classify the land into orange trees, grass and ground, providing the ground truth for the main experiment which used a laser scanner. Furthermore, Arnal Barbedo, Jayme Garcia Vieira Koenigkan and Teixeira Santos, 2016 presented a method for identifying plant diseases, based on color histograms of the training images and a supervised classifier. Maturity of fruits can also be assessed by using color images, as shown by Sekhar Nandi, Tudu, and Koley, 2014 for mangoes.

  Three dimensional reconstruction of the environment is mostly addressed by using stereo vision systems. However, using a single camera and image registration algorithms (e.g., structure from motion) can provide 3D information of the environment. Specifically, Miller, Morgenroth, and Gomez, 2015 described the estimation of height, diameter and volume of linden, walnut and maple trees from images acquired with a single hand-held camera. The authors report acceptable accuracies when comparing with hand measured values, proving the suitability of the proposed approach for assessing the structural parameters of small trees. Additionally, a camera placed on a manually driven platform was used by Jay et al., 2015 to estimate height and leaf area of different plant

species. The results were compared with destructive hand-measured values, obtaining a strong linear correlation. Nevertheless, the main drawback of these registration algorithms lies in the need of static structures to be reconstructed, since slight displacements (e.g., wind moving the trees or plants) of the objects cause poor 3D alignments.

- Stereo Vision: This is a sensing system capable of providing a 3D color reconstruction of the environment, by using two or more monocular cameras in a fixed configuration. The level of description varies depending on the resolution of the camera; however, high resolution images results in a large amount of data to be stored, which make real-time applications a challenging task. The outcome of this measurement system is a 3D point cloud that renders the scene, similar to the approaches that use a color camera and a depth sensor together. In this way the applications in agricultural research are similar to those described earlier, by estimating structural parameters, representing the morphology of the plants and detecting plant or fruits. With this respect, Kazmi et al., 2014 reported the comparison of time of flight cameras and stereo vision systems for leaf imaging purposes under different illumination conditions. Fruit detection applications have also been studied using stereoscopic vision, as reported by Wang et al., 2013, for red and green apples. The authors used image processing techniques based on the color information to detect the fruits in individual images. Depth information was used to remove duplicates based on the distance between two estimations. Results showed good accuracy, reporting errors of 3.2% when detecting red apples and 1.2% for green apples. Additionally, an example of blossom detection within the canopy of peach trees is reported by Nielsen, Slaughter, and Gliever, 2012, obtaining an accurate positioning.

- Thermal Cameras: Temperature have proven to be an important parameter for some agricultural activities like crop diagnosing and fruit detection. For example, Fig. 1.5 shows the thermal characterization of an ornamental tree, which can provide means to segment the tree from the rest of the scene, and later assess the status of the canopy. Furthermore, the plant temperature has been recognized as an indicator of plant water availability (Baluja et al., 2012), which would allow the development of site-specific irrigation technology based on the temperature of the plant. The relationship between temperature of the leaves and water stress or transpiration in the plant using thermal cameras have also been addressed, as reported by Jones et al., 2009. However, in the same work it is stated that the relation is not one to one since the modification in those physiological parameters of the crop also depends on other variables such as: ambient temperature, quality of the air and soil, etc. Hence, the water stress diagnosis of the crop requires the application of a multi-sensor approach.

  Another use of thermal cameras is for fruit detection. Fruits absorb and irradiate the solar radiation in a different way compared with leaves and trunks, which allows to design accurate classification methods. Specifically, Wachs et al., 2010 used a thermal camera along with RGB imagery to detect green apples by applying image processing approaches. The authors reported an accuracy up to 74% when using together thermal and color camera images in the processing. Within this framework, one of the most important applications of

FIGURE 1.5: Color image of an ornamental tree and its thermal view. (Yandun et al., 2017) © 2017 IEEE.

fruit recognition on trees is the development of automated harvesting systems, as the reported by Ji et al., 2012, for red apples. In addition, thermal imaging also represents an attractive solution to identify human operators or animals, especially when they are partially occluded or hidden in high vegetation (Reina et al., 2016).

- Multi- and Hyper- Spectral Cameras: Absorption and reflection of radiation in certain bands of the electromagnetic spectrum are well related with a number of physiological variables such as, water stress, chlorophyll content, nitrogen deficiencies, among others. For example, the chlorophyll pigment absorbs light in the red (long wavelength) and the blue (short wavelength), whereas the green light is reflected. Furthermore, the reflectance in the mid-infrared (MIR) band is influenced by the water content of the crop. This reflectance information of the canopy can be measured by spectrometers and cameras. However, the additional spatial information also provided by a camera makes it more suitable for vegetation analysis. According to the span of the electromagnetic spectrum covered and the resolution and quantity of the bands that they are capable of measure, these sensing devices can be catalogued as multi-spectral (MS) and hyper-spectral (HS). Multi-spectral imagery can quantify the reflectance of the scene in a few broad bands, which are not necessarily contiguous, for example: Visible (VIS, 400-700 nm wavelength), Near Infra-Red (NIR, 700-1000 nm wavelength), Short Wave Infra-Red (SWIR, 1000-2500 nm wavelength), among others. On the other hand, hyper-spectral cameras allows a sort of continuous measurement of the spectrum, providing reflectance readings in contiguous narrow bands. In this context, Fig. 1.6 illustrates this difference between MS and HS imaging. Another important difference between these sensing systems lies in the amount of information to be processed. The level of spectral detail obtained with HS cameras produces larger quantities of data.

  Satellite, aerial and terrestrial methodologies have been employed to collect MS and HS imagery for a number of applications (Slaughter et al., 2008; Kross et al., 2015). From this spectral information several broad and narrow band indices

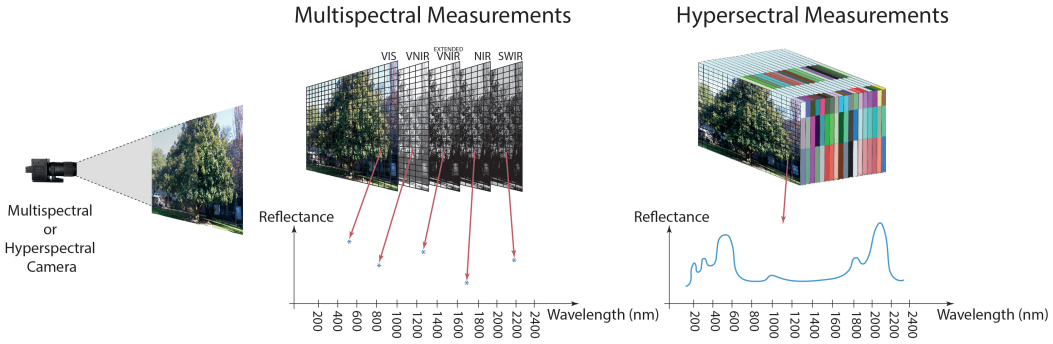

FIGURE 1.6: Schematic representation of the measurements provided by multi-spectral and hyper-spectral cameras. MS imagery allows to determine reflectance in discrete broad bands of the electromagnetic spectrum, whereas HS imagery provides spectral information for narrow and contiguous bands. (Yandun et al., 2017) © 2017 IEEE.

have proved to be suitable for evaluating specific physiological aspects of the canopy. A complete list of such indicators, its definition and the variables that they measure is detailed by Mulla, 2013. Multi-spectral imagery along with aerial methods have been very popular to evaluate the status of the canopy using these indices. Water variability, vigour chlorophyll detection, crop yield, nitrogen stress and weed infestation are some of the aspects that have been evaluated using unmanned aerial vehicles (Baluja et al., 2012; Zaman-Allah et al., 2015; Torres-Sánchez et al., 2013).

Despite the good results obtained when using MS data, in some cases it can not provide conclusive information about the status of the vegetation. This is mainly because certain characteristics of the canopy are more correlated with its response in narrow bands, which are obtained with HS data. However, due to its high dimensionality, the bands that do not contribute with information are usually excluded from analysis by using statistical (e.g., Principal Component Analysis) (Deventer et al., 2015) or Machine Learning techniques (Romero, Gatta, and Camps-valls, 2015). In this way, a number of works report the use of hyper-spectral vegetation indices for PA. Water and plant stress, pest infestation and soil properties are some of the characteristics that can be assessed employing HS imagery (Hillnhütter et al., 2011; Zarco-Tejada, González-Dugo, and Berni, 2012; AghaKouchak et al., 2015). In the same vein, Martinelli et al., 2015 reviewed the recent works about agricultural applications of HS imagery.

Multi-spectral and hyper-spectral information acquired with terrestrial methodologies have similar agricultural applications as explained before (e.g., nitrogen uptake levels, weed detection, pest infestation), as reported in various scientific works (Svensgaard, Roitsch, and Christensen, 2014; Corti et al., 2015). However, fruit localization and quality evaluation are specific applications which can be better addressed using proximal sensing. For example, Okamoto and Lee, 2009 used a motorized HS camera to detect green citrus. The results obtained high true positive detections for fruit located in the periphery of the canopy (up to 100%) and promising true detections when the fruit was occluded by the leaves of the trees (up to 79%). In addition, Li et al., 2016a presented a system

capable to detect skin imperfections in peaches. The sensing system consisted on a HS camera pointing to the fruit in a chamber illuminated by halogen lights. The results showed accuracies greater than 86% when classifying 9 types of peach skins. These spectral sensing systems could be used for yield estimation or to be part of harvesting units.

Figure 1.7 shows the evolution of range and vision sensing systems in the last fifty years, and their main contributions. Surprisingly, thermal and multispectral sensing are “old" solutions that were already proposed in the late sixties. Recently, the decreasing in the technology costs and the availability of powerful processing systems have arisen new interest and opened new applications including PA. The most recent sensors are structured-light cameras that represented a huge leap forward due to their high performance/cost ratio.

FIGURE 1.7: Evolution in the use of range and artificial vision sensors for morphological characterization and fruit/plant detection. The years report the first use of these sensing systems for agricultural purposes. (Yandun et al., 2017) © 2017 IEEE.

Table 1.1 provides a summary about the phenotype feature that can be measured or estimated using the sensors and sensing systems reviewed.

1.2.2 Descriptive Characterization of the Terrain - Robotics Perspective

The diversity of soil types present in off-road environments makes the roads usually consisting in low-traction, deformable and steep-hill terrains, which can quickly degenerate the quality of the positioning and compromise the task execution. For any vehicle to drive along a feasible, safe and efficient path, recognizing the terrain beneath it and the effects on its movement is crucial. In the context of autonomous or semi-autonomous service units, dynamic and descriptive methodologies can be adopted. This Section focuses on the last approach, which mainly consists in classifying the terrain in certain categories or representing the geometric properties of the soil surface as ground planes or elevation maps. To this aim, range and artificial vision sensors are the most suitable devices, as reported in the literature and reviewed below.

Range Sensors

- Time of Flight (ToF) Cameras: Characteristics of compactness and frame rate have made these sensors used for terrain classification, obstacle detection or

TABLE 1.1: Sensing systems commonly used to estimate most of the important phenotype features

Feature Type	Phenotype Feature	Appropriate Sensor/Sensing System
Morphological	Leaf area coverage	2D-3D LiDAR, ultrasonic, stereo vision, color cameras
	Foliage Density	2D-3D LiDAR, ultrasonic, stereo vision, structured light cameras
	Stems shape and size	2D-3D LiDAR, stereo vision
	Plant height	2D-3D LiDAR, ultrasonic, color and structured light cameras
Physiological	Nutrient content	HS LiDAR, MS and HS cameras
	Water stress	Thermal, MS and HS cameras
	Biomass	MS and HS cameras
	Fruit Maturity	Color, thermal, MS and HS cameras

traversability assessment, in general (De Cubber and Balta, 2015; Santamaría-Navarro et al., 2015). For example, Yu et al., 2014 used range and intensity measurements from a ToF camera to obtain geometric descriptors of the terrain in laboratory conditions. Subsequently, a supervised learning algorithm allowed to detect rocks, slopes and negative obstacles, obtaining accuracies above 90%, when testing in an artificial sandy environment.

Since color is not available in classic ToF cameras, various studies propose a sensor fusion scheme to include RGB data in order to enhance traversability through obstacle detection (Benet, Rousseau, and Lenain, 2016; Zins, 2017). As an alternative, devices combining range, color and intensity data have arisen recently as a suitable option. Furthermore, the cost-benefit relation of such devices has made researchers to study its applications for mobile robots (Aguilar and Morales, 2016; Hernández-Aceituno et al., 2016). For instance, Zeltner, 2016 employed color, depth and infrared data from a Kinect 2.0 along with a deep neural network and a clustering algorithms first segment images in regions of interest. Subsequently, each section was classified as drivable or no drivable based on the movement of the objects in presence of an air stream. Furthermore, a similar version of Kinect was employed by Woods, Guivant, and Katupitiya, 2015 to classify six types of terrains. Depth information was used to stablish a geometric model based on a Piece-Wise Multi-Linear surface approximation. Texture features obtained from this model were later employed in a supervised classification scheme to obtain the corresponding labels. An average accuracy of 92.3% is reported when testing outdoors under soft sunlight illumination.

Despite of the advantages of these sensors and the promising results reported

before, drawbacks in terms of receptor saturation due to sunlight, short range and resolution limits its applicability in rough conditions (Fankhauser, Bloesch, and Rodriguez, 2015).

- LiDAR: Robustness and versatility of these devices in field conditions made them specially popular in off-road vehicles. Applications including obstacle detection, terrain classification and generation of occupancy maps or elevation models have been addressed by using 2D or 3D laser range sensors (Reina, Milella, and Worst, 2015; Fernandez, 2010; Meng et al., 2018). Several 2D LiDARs mounted on a self driving car were part of the first robot to win the Defense Advanced Research Projects Agency (DARPA) challenge, as reported by Thrun et al., 2006. A probabilistic map generated in a fusion scheme allowed to classify terrain in front of the robot as occupied, free and unknown. Such map, along with the other systems of the robot, autonomously drove it through the Mojave desert in the United States for more than 6 hours. In fact, ambient complexity and uncertainty in measurements or models have made probabilistic maps widely used tools for traversability assessment of unmanned vehicles (Broten, MacKay, and Collier, 2012; Sock et al., 2014).

  Given the characteristics of these sensors, plenty of the applications are oriented to characterize the morphology of the terrain or its components. However, most of LiDAR devices also measure the intensity of the received signal, which is used to categorize different zones in aerial approaches. In ground applications, this characteristic have also been exploited in a small extent, as reported by Laible, Khan, and Zell, 2013. Four types of terrain were classified using a fusion of a 3D laser scanner and a RGB camera. Range, intensity and color values are employed as input features for a random forest algorithm, obtaining classification accuracies above 80% when testing outdoors.

  Despite of the results reached with such range sensors, they have shortcomings that make them not suitable in certain cases that include presence of fog, excessive dust, smoke, or specular properties of the surfaces. Further, a "finer" classification of the terrain in various categories is difficult to obtain, as reported by Andújar et al., 2013.

- Radar: This type of range sensors are quite similar to LiDARs. However, the operating principle of radars make them suitable when operating in presence of substantial dust or other visual obscurants. This robustness to ambient conditions come at the expenses of considerable increase in the sensor cost. For this reason, few research works report applications with radar sensors. Nevertheless, they are used for scene understanding mainly to detect traversable or non-traversable regions of the soil surface (Reina, Underwood, and Brooker, 2011).

Artificial Vision Sensors

- Color Cameras: Most of the applications using color cameras are appearance-based. Texture and two-dimensional geometry features obtained from images is mainly employed for terrain classification. For example, Ono et al., 2015

distinguished various classes of traversable or non traversable regions by employing grayscale images of a camera mounted on a space rover. For agricultural purposes, the same issue was also addressed by using the same sensor (Ball et al., 2016). Moreover, Zou et al., 2014 compared different approaches for terrain classification from visual information. The authors extracted different texture and color descriptors of images captured from moving robots in outdoor environments. The results showed that using certain descriptors and learning algorithms with 2420 samples provided robustness to moderate changes in illumination.

Spreading of machine learning methodologies using data acquired with color cameras also increased the amount of research work in autonomous robot navigation in the last years. Supervised and self supervised approaches using visual cameras are usually employed, specially for planetary exploration (Brooks and Iagnemma, 2012; Ono et al., 2015; Otsu et al., 2016). Lack of in-situ information in this application, make the use of self supervised methodologies a practical approach. In contrast, terrestrial applications do not present this drawback, hence it is possible -and in some cases necessary- to use available a-priori information in order to anticipate the upcoming navigation behaviour of the vehicle (Muller et al., 2013).

Usage of color cameras for other activities different from terrain classification is also reported in a small extent. Traversability metrics were derived from inertial sensors and subsequently associated with moment-based features in the images in the work of Guo et al., 2011. Later, a path planner employed outputs from a supervised classifier trained with these features to determine the optimal route in a rocky environment. Other image-based characteristics (i.e., terrain roughness, discontinuity and hardness) that account for robot traversal difficulty were also extracted by Howard and Seraji, 2001. These features were then combined using a fuzzy logic framework to form a traversability index. Results showed that the proposed methodology leads to a successful assessment of terrain segments based on such index.

- Stereo Vision: In this case, texture and two-dimensional geometric characteristics also include distance information. Thus, obstacle detection and terrain classification can be addressed using a single sensor. Color and texture details along with distance features are usually employed as inputs to learning methodologies in various off-road scenarios (Fleischmann and Berns, 2016; Ross, 2016). Generally, the image-based descriptors are used for scene classification, while the distance information contributes to complement or refine the output. For example, Shneier et al., 2008 used the images from color cameras for terrain classification, while range data was used for obstacle detection. Thus, appearance-geometric models are constructed to assess the traversability of the terrain in front of the robot. The processing capabilities of current computers have made deep learning strategies very popular. Self driving cars employ a vast amount of data to train models that "generalize" navigation capabilities for various terrains (Ramos et al., 2017; Song et al., 2018).

- Multi-spectral Cameras: Spectral information in thermal, near infra-red (NIR) or narrower bands contribute with additional cues to highlight certain features

of the terrain. While there is a large amount of research work using these sensors in remote sensing and agricultural applications, there are few reports on multi- and hyper- spectral image analysis for robot navigation. For example, Winkens, Sattler, and Paulus, 2017 used hyper-spectral imagery in the NIR band to evaluate the terrain in front of a standard car. Drivable, rough and obstacle regions were classified using a Random Forest algorithm, obtaining up to 70% accuracy.

Thermal cameras have also been used for descriptively characterize the terrain. As a proof of concept, González, López, and Iagnemma, 2017 investigated the relationship between soil strength and moisture, thermal inertia and traversability in wet and vegetated soils in different lighting conditions. Results showed that it is possible to recognize wet-sand, dry-sand and vegetated areas using the proposed approach. In the same vein, Cunningham, Nesnas, and Whittaker, 2015 assessed the relation between soil strength and traversability by using thermal imagery. Authors found that thermal inertia was correlated with the traction properties of the soil. Thus, they were able to differentiate between safe, compact and hazardous loose soil.

Hybrid Devices and Other Sensors

In some scenarios (specially in off-road environments) the limitations of using only one type of sensor limits the capabilities to perceive the surroundings. Range sensors are mostly limited in presence of dust and fog, while changes in lightning can seriously affect visual devices. Multi-sensor approaches can overcome the individual limitations of each device, providing robust and accurate solutions in real operation conditions. For instance, Häselich et al., 2013 used a fusion of color and three dimensional laser information to distinguish between 5 terrain classes. Various features obtained from this data were calculated and subsequently applied to a probabilistic learning approach based on Markov Random Fields (MRF). The proposed system was tested in field with a mobile robot, obtaining accuracies greater than 95%, but real-time operation can not be performed when employing features from the two sensors. In addition, combination of LiDAR, stereovision, radar and thermography for detecting obstacles and traversable ground was studied by Reina et al., 2016. This work investigated diverse learning algorithms to combine data from these sensors in an off-line processing scheme.

Inertial sensors are also reported to be used for terrain classification. They are usually part of a sensor fusion scheme, where inertial measurement units are combined with cameras or range sensors to refine the classificaiton (Coyle, 2010; Brooks and Iagnemma, 2012; Otsu et al., 2016). However, the use of accelerometers alone as vibration sensors for terrain classification purposes have been studied, as reported by Weiss, Frohlich, and Zell, 2006. In this work, z-acceleration values from a sensor placed on the body of the vehicle was used to obtain custom features which allowed to train a supervised classifier and subsequently, to distinguish between six types of terrain.

1.2.3 Dynamic Characterization of the Terrain - Robotics Perspective

Complementary to descriptively characterize the soil surface, it is also necessary to estimate and/or to predict the dynamic effects underlying in the interaction robot-terrain. For example, slipping and skidding situations (which are the most evident effects of the terra-mechanic interaction between the vehicle and the terrain) are likely to occur in agricultural environments (as the one shown in Figure 1.8). The modelling and characterization of this phenomena can be employed in several ways, namely: to improve the positioning system of the robot, to allow an efficient management of the vehicle inputs (e.g., battery or fuel) or to avoid and detect immobilization or trapping conditions. Various of these applications have been studied for planetary exploration, nevertheless, they have not been fully addressed for agricultural purposes. Along with the use of sensing devices, this application often requires of kinematic

FIGURE 1.8: Earthmoving machine navigating on a typical agricultural off-road scenario. Terrain variability, vehicle characteristics and lack of GPS signal induce uncertainty in movement predictions and slip detection. Robot positioning and wheel slippage can thus be considered as random variables in the navigation process.

and/or dynamic models to take the relation between soil and robot variables into account. Depending on its fidelity and accuracy, the complexity (computational and mathematical) increases along with the amount of sensory information required. According to Taheri et al., 2015, terra-mechanics models for wheeled robots are divided in three categories: empirical, semi-empirical and physics-based. Empirical models are the result of laboratory or field test experiments. After several trials the mobility of the vehicle is related with various measurable parameters of the wheel-terrain interaction by means of curve fitting techniques. This methodology allows to obtain mathematical expressions to describe the required strength necessary to traverse specific terrains, for particular driving conditions (Pacejka, 2005; Hegazy and Sandu, 2013). For this reason, the extrapolation to new tire configurations or operating conditions, in general, is not possible. It is noteworthy that most of these

researches are funded by military organizations, however, some works are reported to be applied in other activities. Particularly, Brixius, 1987 presented a traction model that includes the effect of wheel slip for bias ply tires of agricultural machinery. The equations presented there relate the wheel torque, motion resistance, net pull and tractive efficiency to wheel load soil strength, tire geometry and deflection. This relations were later used in simulations to predict the performance of commercial tractors.

Regarding the physics-based models, they provide more general and accurate estimations by incorporating physical principles and analytical methods. The degree of complexity varies depending on how deep the physical interactions are modelled, which directly increases the complexity (mathematical and computational) and the accuracy obtained (Wakui and Terumichi, 2011; Smith and Peng, 2013). However, the most used methods to model the interactions between the vehicles and the terrain are based on semi-empirical approaches. In this way, the computational effort and complexity are reduced by relating the vehicle and tire kinematics with empirical deterministic models already available. These approaches in general consider a single contact point and two types of tyres interacting with the soil surface: rigid and flexible. The latter have higher complexity since the deformation of the wheel in contact with the terrain must be taken into account. However, all of these models relate the shear stress and displacement, lateral and longitudinal slip, sinkage, among other mechanical parameters of the soil-wheel interaction with the model of the vehicle, and the vertical and horizontal forces experimented by the wheel (Ishigami et al., 2007; Wong and Asnani, 2008).

While a dynamic analysis of the robot motion is more faithful, it is also more complex and computationally expensive. For this reason, kinematic models to account for the "gross" effects of the wheel-terrain interaction (e.g., lateral and longitudinal slip on the vehicle body) have also been developed (Rogers-Marcovitz and Kelly, 2010). Concretely, Seegmiller, 2014 claims that his kinematic models accounting for slip can perform as well as a dynamic formulation.

Forces and other variables obtained from the models discussed above are employed later in deterministic kinematic and dynamic models for the robot motion. Thus, position or velocity of the robot can be accurately estimated (Ishigami, Kewlani, and Iagnemma, 2009; Ishigami, Kewlani, and Iagnemma, 2010). At this point, sensory information allows to calibrate or identify certain parameters that regularly change depending on the characteristics of the terrain. One of the most relevant and practical works in this matter was developed by Iagnemma and Dubowsky, 2004. Parameters from the he Bekker-Wong terra-mechanical model (Bekker, 1956; Wong, 2001) were identified based on simplified equations developed by the authors. Other works also report the use of a mixture of kinematic and dynamic modelling for mobility prediction tasks. For example, Ordonez et al., 2017 first calibrated a kinematic model which was used in complement to a terra-mechanical model for efficient energy motion planning. Furthermore, the same calibration apporach was used by Rogers-Marcovitz and Kelly, 2010 to identify a kinematic model that accounted for the slipping effects on the movement of various robots.

In the following, applications of the most used sensors in this matter will be reviewed.

Vision Sensors

- Visual Cameras: Robot motion variables (e.g., pose or velocity) inferred from visual approaches have proved to be useful for estimating lack of traction rocky and loose soil surfaces (Fraundorfer and Scaramuzza, 2012; Gonzalez et al., 2013). For example, Song et al., 2008 used optical flow and a sliding mode observer to estimate slip and velocity in a research rover. Indoor experiments showed consistency in position estimations of the robot when compared with the ground truth. However, all the experiments were conducted in laboratory, which limits its applicability in conditions field conditions. In addition, Reina et al., 2010 used a color camera detect the trace of the wheels in sandy terrains. With this information, the authors estimated the slip angle estimated, which allowed to correct the odometry of a space rover.

  Geometry and appearance information inferred from stereo imagery allows to correlate also the morphology of the terrain with wheel skidding or longitudinal and lateral slip. Thus, not only perception but also prediction strategies have been developed using this type of sensor. As an example, Angelova et al., 2007 used visual odometry and encoder readings to estimate slip which later was correlated with the geometry of the terrain. At the same time, visual data served to classify the soil surface in six types, namely: sand, soil grass, gravel, asphalt and wood-chip. This information, along with inertial measurements were used in a supervised classification scheme to learn a predictive slip model for those terrains. However, the main drawback of this study comes from the issues of this sensor in presence of changing illumination. Moreover, a large amount of training data is required to obtain robustness for outdoors navigation.

- Thermal Cameras: This sensing approach is less common for dynamic characterization. However, as complement to their terrain classification approach, Cunningham and Whittaker, 2017 used thermal properties of granular terrains to improve slip predictions for the Curiosity rover. A mixture of experts allowed to learn the correlation between thermal inertia and high-slipping sandy regions.

Inertial and Other Sensors

- Inertial Sensors: Using these devices alone for estimating the vehicle motion is usually non appropriate because of the drift and offset accumulations obtained when integrating gyroscopes and accelerometers readings (Iagnemma and Ward, 2009). In contrast, they have proved to be appropriate when used in sensor fusion schemes (Iagnemma et al., 2004; Lee, Shirr, and Cho, 2009; Oonk et al., 2014). In fact, various works reviewed up to this point employ inertial measurements at some point to infer information about the effects of the terrain in the robot movement. For instance, Kim and Lee, 2013 used propioceptive sensors including IMU, encoders and motor current to estimate a soil resistance coefficient and slip ratio. This information was later employed to identify optimal control parameters in grass, gravel and sand, which later could be applied to ensure optimal robot maneuverability in those terrains.

- Electric Current: Sensing electric current consumption of the motors is an indirect manner to measure torque. These sensors are usually mounted in experimental test-beds consisting of a single actuated wheel moving on different types of terrain (Ishigami et al., 2007; Shamrao et al., 2018). While most of the applications of such testing devices is biased towards planetary exploration, terrestrial research is also being developed. For example, Kim and Lee, 2018 proposed a control algorithm based on optimization of slip and traction for diverse type of terrains. Development tests were conducted in grass, dry sand and gravel with the single wheel test-bed using torque, drawbar pull and normal load measurements. The control strategy was later validated in a research vehicle, with successful slip compensation results.

Despite of the large amount of work about this topic, there are some remaining gaps to be filled. A key issue to deal with is the accurate, unbiased estimation and the propagation of measurement uncertainty in the robot motion model. Clearly studying this aspect have not yet been addressed by machine learning or traditional approaches. The last usually provide punctual estimations based on linearisation, Gaussian noise assumptions or custom robot modelling (Lindsten, 2013). Machine learning approaches, on the other hand, are non-parametric methodologies in which the uncertainty propagation through the learning process is not clearly defined (Gal, 2016). There are few works that aim to probabilistically estimate the robot motion or identify parameters in a kinematic or a dynamic model and subsequently progapate the uncertainty through all the variables related with the robot motion. The recent work of Shamrao et al., 2018 proposed a particle filtering approach to estimate parameters of a wheel-soil interaction model. This research work contributes with a first attempt to use bayesian techniques in complex non-linear an non Gaussian models. However, it provides only laboratory experimentation with little information about the propagation of uncertainty in other variables related with the robot motion. Precedents in system identification strategies based on statistical inference and Markov Chains theory and Bayesian inference have proven to deal with these issues in other scientific areas. For example, Solin et al., 2018 used Gaussian process to model the magnetic field indoors. This non-parametric approach also allowed to predict the magnetic field in locations where measurements were not available. Experimental results showed the practical applicability of the proposed method, which also was capable to propagate the uncertainty throughout the learning process. Additionally, Schön et al., 2015 identified a model of ice varves (i.e., annual layers of sediment or sedimentary rock) thickness using various probabilistic methods. They allowed to determine not only the model parameters but also to obtain their posterior distributions. It is interesting to note that the underlying distributions employed in this work were not Gaussian and the model was non-linear.

1.3 Hypothesis and Objectives

The previous discussion about the work developed by other authors, allowed to recognize various points in the state of the art that need further research, namely:

- Satellite and aerial applications provide satisfactory results to assess big amounts of vegetation with few samples. However, when the aim is to analyse a portion of the crop or individual trees, they present important drawbacks (e.g., obtaining views of the crown, or not enough spatial resolution).
- Structural and physiological assessment of crops are still studied individually, with specific applications for each case. Integration of both is still a remaining gap in the state of the art.
- The time required to scan the grove is an important parameter to improve the farm productivity. However, few works aim to get accurate estimations, improving the overall sensing time.
- Most of the proposed approaches for descriptive terrain characterization does not take into account the final cost of the solution. While satisfactory results are reported in various works, it is necessary a trade-off between cost and high accuracy in field conditions.
- Off-road mobility assessment by slippage prediction and detection is usually performed with parametrized models. Estimation of such parameters is often done with deterministic or machine learning techniques. This approaches offer punctual estimations with few information about the posterior distributions of the estimated variables (when considering other than Gaussian distributions). Thus, error propagation or a probabilistic assessment of robot slippage and mobility is not possible.
- An integral work relating both faces of PA technologies (agricultural sensing and navigation of service units) in a PA-robotics scheme has not been proposed.

1.3.1 Hypothesis

Perception for service units in agricultural environments plays a key role for navigation and task execution. Linking both enables a PA-robotics framework, which considers the ambient awareness of the vehicle not only for navigation or control but also for the vegetation assessment. This relationship between agricultural and robotics applications allowed to extend the hypothesis presented in the thesis proposal as follows:

- Proximal sensing using terrestrial methods could overcome common drawbacks of aerial approaches in a variety of groves. Thus, phenotyping applications can be developed using sensors which can be placed on any agricultural vehicle. Concretely, structural and physiological characterizations can be combined by means of LiDAR and thermal sensor fusion. Accordingly, the collected information can be further used as a tool for the farmer to take proper actions on the grove. It also can be experimentally shown that given the proper conditions, the scanning methodology and data processing can be used to estimate particular structural variables, decreasing the sensing time of the crop.
- Low cost sensors can be employed to get accurate terrain classification results in field conditions.

- Slippage is one of the effects of the wheel-terrain interaction. Parametrized models relating the robot movement and slippage can be probabilistically identified using bayesian estimation and probability theory. In addition to get the most probable values, it is possible to get the posterior pdf of the parameters, as well as other variables of the robot motion.

1.3.2 Objectives

The main objective of this thesis is to provide a comprehensive framework which links sensing applications for crop phenotyping and mobile robot perception. This link is given by the use of sensors and sensing systems which can be placed on an automated or semi-automated vehicle navigating in agricultural environments. The specific goals that allow to reach the proposed objective and to address the previously stated hypotheses are:

- To propose agricultural applications that employ sensors that can be mounted on a mobile robot for getting a structural and physiological characterization of the vegetation.
- To study the effects in the accuracy of the estimation of structural variables from the canopy (i.e., treetop volume) when using only partial data acquired with a laser scanner.
- To use a low cost sensor for terrain classification achieving high level of accuracy rates in field conditions.
- To study and implement a methodology for probabilistic model identification with room to analyse not only parameter posterior distributions, but also traversability-related variables (i.e., wheel slip).

1.4 Thesis Structure

This Chapter presented the problem formulation, along with basic ideas to introduce the intricate relation between sensing applications for both precision agriculture and robotics. To sustain the hypotheses, it also presented a complete review of the state of the art for both applications: agricultural and mobile robots perception in off-road environments. Chapter 2 presents two case studies for plant phenotyping using a proximal sensing approach intended to be coupled with robotic vehicles in field operations. In Chapter 3, the robotics perspective of this thesis is first addressed. A methodology for terrain classification using a low cost sensor mounted on a research robot is developed and evaluated. Experimentation includes extensive field tests with ambient conditions similar to those found in a common agricultural environment. In complement, Chapter 4 details a probabilistic slip model identification method, providing thus a dynamic terrain characterization approach. Following the practical focusing of this thesis, experimental results in field are also detailed. Finally, Chapter 5 details the overall conclusions of this research work.

Chapter 2

Application of Sensing Systems to Crop Phenotyping - Case Studies

Mounting one or various sensors in robotic platforms provides a great versatility for phenotyping tasks including disease detection, water stress, crop monitoring, harvesting, among others. This Chapter describes practical applications on robotic sensing for two of these activities: canopy volume estimation and temperature stress assessment. Both comprise important physiological and environmental parameters that reflect the crop status and quality. Canopy volume and shape has a special significance because it combines in a single variable, the width, height, geometric shape and the structure of the trees, as reported by Sanz et al., 2013. Leaf temperature, on the other hand, is a meaningful parameter since it is a main factor of the physiological process of the plants. It maintains adequate levels of photosynthesis and transpiration, depending on the water status of the soil, atmospheric conditions, and the tree architecture among other factors (Wang, Vinocur, and Altman, 2003; DaMatta and Cochicho Ramalho, 2006).

The Chapter is organized as follows: Section 2.1 details the methodology and experimental tests for canopy volume estimation. In addition, evaluation on the use of partially scanned data is described as a way to decrease the measurement time. In complement, Section 2.2 describes the overall approach to get a 3D and thermal representation of fruit trees. It also describes the corresponding field testing within an avocado farm. Finally, Section 2.3 summarizes the contributions of the case studies presented in this Chapter.

2.1 Case Study I: Treetop Volume Estimation

This application studies the effects on the accuracy of the volume estimation of trees when using partial data from the canopy. To this aim, four computational methodologies based on LiDAR readings: convex hull, segmented convex hull, a cylinder based approach and an occupancy grid approach. The main objective in this case study is to compare and to evaluate the estimations obtained with each methodology when canopies are partially scanned, thus avoiding the need of visiting all the alley-ways in the grove. Therefore, consumption of the service unit resources can be reduced, improving the efficiency of the overall scanning process.

Convex hull approach

The convex hull approach is based on the work developed by Auat Cheein and Guivant, 2014. It finds the points that belong to the closest convex set that contains all the points from a given point cloud. The main features of this technique can be summarized as follows:

- It finds the smallest convex set that contains the entire cloud of points. The points of the convex hull set can be considered as the corners of a rigid body that contains all the points and a volume can be associated to it. In fact, it can be shown that the convex hull approach provides of an upper bound for treetop volume estimation (Auat Cheein and Guivant, 2014).
- As the number of points in the cloud tends to infinity, the volume of the convex set associated with such cloud tends to its minimum.
- Convex hull has been proved to work in real time implementations.

2.1.1 Segmented convex hull approach

This methodology takes into account the advantages of the previous approach, but restricted to a portion of the point cloud. In this way, it overcomes the overestimation problem of the first approach. Briefly,

- Let Ω be the point cloud to be analysed, and z_{min} and z_{max} the minimum and maximum values, respectively, of the z- coordinates of the points from Ω.
- Let δ be a step criterion in such a way that $z_{max} - z_{min} = n \times \delta$ where n is a positive integer.
- Then, the convex hull associated with each segment is calculated from $\Omega : \forall p \in \Omega : z_{min} \times n \times \delta \leq p_z < z_{max} \times (n+1) \times \delta$, with $n = 1, 2, \ldots, \frac{z_{max} - z_{min}}{\delta}$, and p_z denoting the z-coordinate of any point in Ω.
- The final volume is estimated by adding all the partial volumes associated with each segment.

2.1.2 Cylinder-based modelling approach

The cylinder-based approach is based on the fact that treetops (from commercial intensive groves) usually show some symmetry on their morphology (e.g., the olive grove shown un Fig. 2.1). According to Chilean farmers, apple, olive, peach and avocado trees (the main fruit tree crops in Chile) also show this symmetry on their crowns. Accordingly, the cylinder-based approach uses this characteristic as a hypothesis. Following the notation introduced in the segmented convex hull approach,

- Let $\Omega_{\delta,i} \in \Omega : i \times \delta + z_{min} \leq p'_z < (i+1) \times \delta + z_{min}$, where $i = 0, 1, 2, \ldots, n-1$.
- For each segment, its center of mass is calculated. Such center of mass then becomes the center of the cylinder. Its radius is the longest distance from the center of mass to any point from $\Omega_{\delta,i}$. Thus, the point cloud is divided in segments through the z axis.

As it can be seen, similarly to the previous method, the selection of δ is a designer criterion. It was set to 0.2m.

FIGURE 2.1: Typical olive grove. Trees are often symmetric with respect to their stems, which can be beneficial to use partial scans for estimating structural variables. (Auat Cheein et al., 2015) © 2015 Elsevier.

2.1.3 3D occupancy grid approach

Occupancy grid approaches are commonly used in 2D and 3D robotic mapping. In this case, a 3D occupancy gridding was used for clustering the point cloud obtained from the scanned canopy. The applied approach is presented by Choset et al., 2005, in which each cell is a cube whose size is determined by the a predefined length of its edge. All cells are disjoint between each other. The total volume of Ω is estimated by adding the volume of all the generated cubes.

2.1.4 Field Testing

The four methods were evaluated with point clouds obtained from real fruit trees orchards. The measuring methodology, as well as the sensing system employed has been developed, tested and previously published by Rosell-Polo et al., 2009 and Sanz et al., 2013. The volume estimation and all subsequent data processing and evaluation employed the Matlab R2014b programming environment (MathWorks Inc., Natick, MA, USA).

Data acquisition

The orchards used in the test were arranged in rows of Blanquilla pear trees, forming a continuous wall of vegetation. A mobile terrestrial laser scanning system using a SICK LMS200 LiDAR sensor was developed for the study. The LiDAR sensor is able to scan in 2D (one single plane), from 0 to 180 deg and with a maximum range of 8 m. It was mounted vertically (as shown in Fig. 2.2) in order to obtain vertical slides of the canopy cross-section profiles as the vehicle navigates the environment. Alongside the distance value, the sensor provides the first echo and the intensity of that returned beam with no chance to analyse the full returning signal.

FIGURE 2.2: Two views of the developed scanning system based on the SICK LiDAR. (Auat Cheein et al., 2015) © 2015 Elsevier.

Figure 2.3 shows a 3D reconstruction of the environment, using raw data and the open access software Cloud Compare. It shows different views of the orchard, as the scanning system was navigating through it. In order to obtain the 3D reconstruction of the environment, the guidelines of Rosell-Polo et al., 2009 were employed to properly build the navigated orchard. In order to obtain the point cloud shown in Fig. 2.3, the developed scanning system first had to map its left side and then its right side as will be described later. Additionally, the distance between two consecutive stems is approximately 2 m, and the length of the system vehicle/scanner is approximately 4 m. Features labelled as doors, correspond to artificial structures manually located in the grove to be used for improving correspondence in data matching processes. Further details regarding the agricultural environment and the data set used in this work can be found in the work of Sanz et al., 2013.

Measurement Methodology

The dataset used in this work corresponds to the point cloud shown in Fig. 2.3, following the vehicle navigation shown in Fig. 2.4. Thus, the system first scanned the row from one side and then from the other side. The measurements were located in a global coordinate frame using point cloud matching techniques following the methodology proposed by Sanz et al., 2013. Briefly,

1. The LiDAR sensor works synchronously acquired 3D information from the environment. At this point, it is to be mentioned that consistency of the 3D reconstruction stage is not addressed in this case of study.

2. The four approaches for estimating the canopy volume presented here (the convex hull, the segmented convex hull, the cylinder-based modelling and the 3D occupancy gridding approach) are able to process batches of 3D data. Therefore, the algorithms will obtain their corresponding estimations whether if 3D data from the entire orchard or just from a particular tree is employed. Since not only the volume of a treetop is important, but also its geometry and density, the batch processing stage was segmented. The system collected data for 2 m of motion of the scanner (which corresponds to the distance between two consecutive stems).

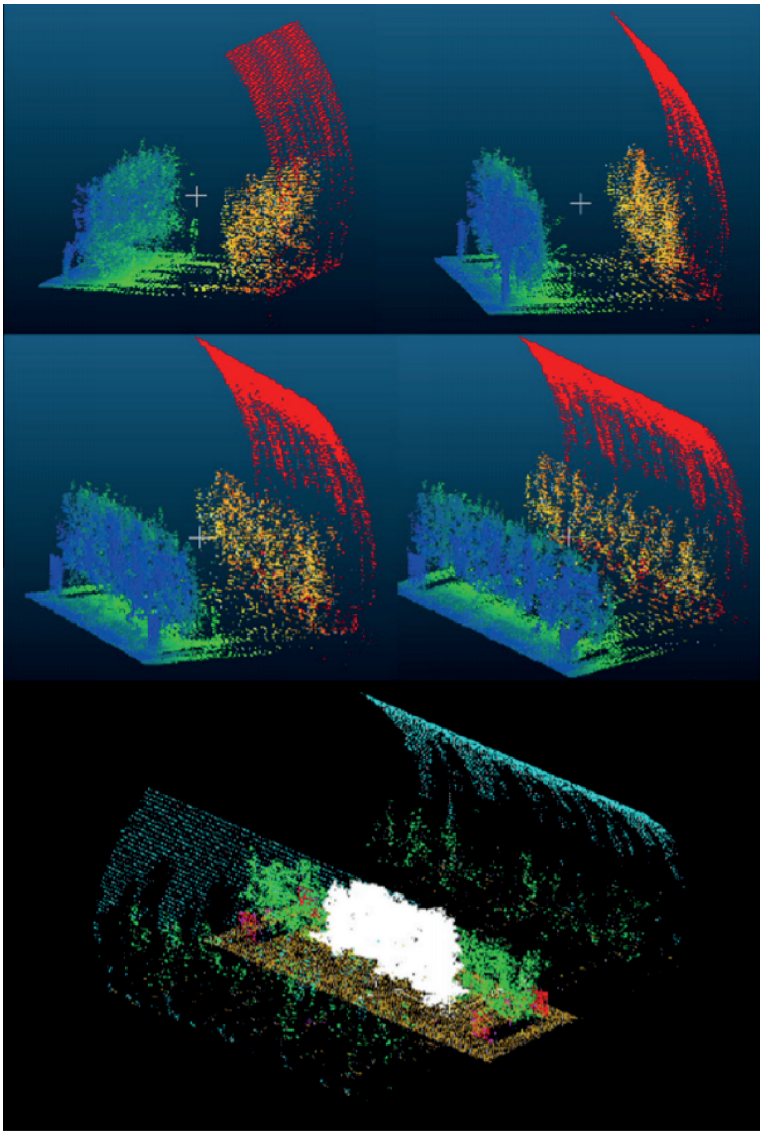

FIGURE 2.3: Three dimensional point cloud obtained with the scanning system shown in Fig. 2.2. (Auat Cheein et al., 2015) © 2015 Elsevier.

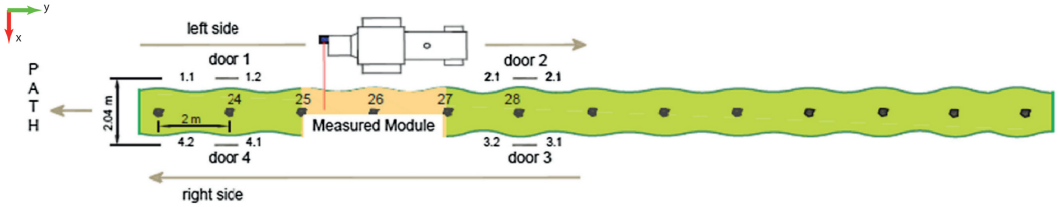

FIGURE 2.4: Navigation path of the scanning system through the orchard. (Auat Cheein et al., 2015) © 2015 Elsevier.

3. Once collected, the 3D raw data is pre-processed. The points associated with the ground were first rejected using Cartesian clustering algorithms (as the ones shown by Milellla, Reina, and Underwood, 2015. In addition, only the points associated with the closer row were processed (thus, points at a distance further than 3 m, are rejected. This is possible since the alley-ways width was

approximately 2.5 m).

2.1.5 Experimental Results

Fully observed canopies

The white coloured portion of data shown in Fig. 2.3 corresponds to the inner 3D data batch shown in Fig. 2.5. It can be noted that according to the convex hull method, the estimated volume was 17.47 m^3; according to the segmented convex hull, the estimated volume was 10.08 m^3; the cylinder based modelling approach estimated the volume in 28.40 m^3. Finally, the 3D occupancy grid approach estimation was 12.48 m^3. It is clear that the cylinder-based modelling approach offers the highest volume estimation values when compared with the others, for the same data batch. In addition, both the cylinder-based and the convex hull approaches offer convex modelling of the row. However, one single point separated from the cloud might produce differences of several orders of magnitude in the estimation process. For example, in the first 3D batch of data, shown in Fig. 2.5 (located at the bottom of the row view), the volume estimation of the cylinder-based modelling is almost twice the value obtained by the convex hull approach. In the same context, the segmented convex hull approach has similar estimation results when compared with the 3D occupancy grid for all the 3D batches of data. However, its resolution is one of the main drawbacks of this technique as will be shown later.

Partially observed canopies

Figure 2.6 shows the orchard characterization using only the 3D batch data acquired from the right side of the row (i.e., the first navigation of the scanning system). As in the fully observed canopy case, only the white coloured region of the orchard shown in Fig. 2.3 was evaluated. For the convex hull approach, the estimated volume was 15.47 m^3; for the segmented convex hull approach, 7.26 m^3; for the cylinder based modelling, 16.73 m^3; whereas for the 3D occupancy grid approach, 8.84 m^3. The results obtained here are of the same order of magnitude than the ones obtained in the previous section. In average, and for the case study presented here, the volume of partially observed canopies is estimated with up to 75% of correspondence, when compared with the fully observable case. Thus, one of the main advantages of using the implemented methods for characterizing canopy volumes of orchards is the fact that it is no longer needed to sense both sides of rows.

Table 2.1 summarizes the volume estimations for the entire orchard. The third column corresponds to the partially scanned canopies from both right and left LiDAR readings (from the alley-way point of view). The fourth column represents the average estimation correspondence (between the left side and right side LiDAR readings and the fully scanned canopies). As can be seen, both the 3D occupancy grid modelling and the segmented convex hull approaches offer the worst volume estimation for partially observable treetops . They were able to determine only the 69% (approximately) of the volume obtained with the full data set. It is worth mentioning that if the partial volume estimation is doubled (for example, for the segmented convex hull approach, if the left-side estimation is doubled to get the volume of the entire orchard) then the volume is approximately overestimated 38%, which is consistently

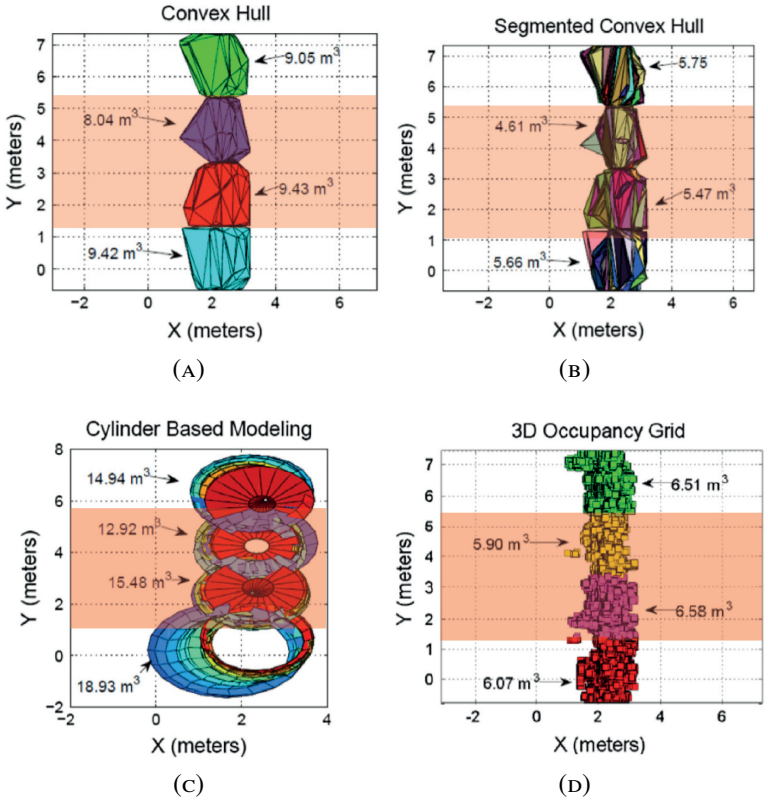

FIGURE 2.5: Volume estimation of a fully observed canopy for the convex-hull (A), segmented convex hull (B), cylinder based modelling (C) and the 3D occupancy grid (D). The red-shadowed regions correspond to the white coloured points shown in Fig. 2.3. (Auat Cheein et al., 2015) © 2015 Elsevier.

worse than the previous estimation. On the other hand, the cylinder-based modelling and the convex hull approach show the best volume estimation for partially scanned rows. Nevertheless, the main drawback of these approaches lies in the drastically increasing of the estimation when points far from the cluster are present. This issue can be overcame using filtering techniques to discard outliers.

TABLE 2.1: Comparative analysis of treetop volume estimation between fully and partially scanned orchards. (Auat Cheein et al., 2015) © 2015 Elsevier.

	Fully scanned canopies (average, m^3)	Partially scanned canopies (average, m^3) (left–right side)	Average estimation correspondence (%)
Convex hull	36.94	31.08–32.03	84
Segmented Convex hull	21.29	14.71–13.97	69
Cylinder-based modelling	62.27	54.31–55.18	87
3D occupancy grid	25.06	17.05–17.12	68

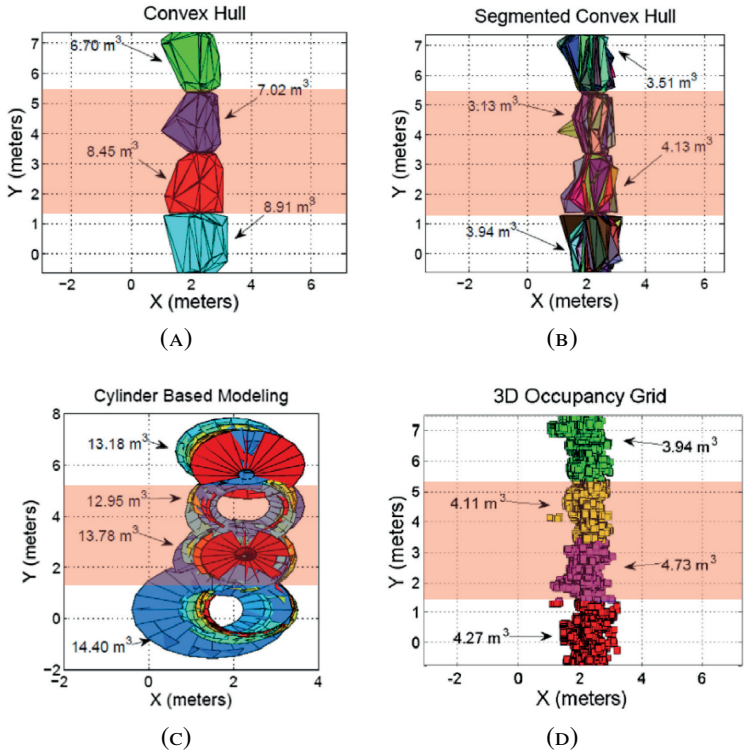

FIGURE 2.6: Volume estimation of a partially observed canopy. (A–D) show the results for the four methodologies for estimation. The red-shadowed regions correspond to the white coloured points shown in Fig. 2.3. (Auat Cheein et al., 2015) © 2015 Elsevier.

2.2 Case Study II: Thermal and LiDAR for 3D heat mapping of avocado trees

This case of study describes the hardware and algorithms employed to get a three dimensional thermal reconstruction of avocado trees. Common sensing approaches in this matter use imagery acquired with drones or satellites. However, both are restricted by the spatial resolution of the images, which always correspond to top views of the canopies, leaving the orchard sides disregarded. To overcome this issue, this Section presents the design and evaluation (including hardware and software) of a portable ground-based system for manual thermal and geometrical characterisations of an orchard. While a static mounting of the device is presented as prototype, its design allows an straightforward mounting on any vehicle/robot. The presented system merges thermal images with LiDAR-based range readings, providing to the user a three dimensional tool to visualize the thermal behaviour of the grove. Additionally, the system performance was compared with an LI-6400 Infra-red Gas Analyser (IRGA) portable photosynthesis system (LI-COR, Lincoln, NE).

2.2.1 Sensing System

The mounting device is a manually-operated commercial tripod shown in Fig. 2.7. Its characteristics of low weight and small dimensions allowed to make the system portable. The sensors (LiDAR and thermal camera) were placed on the plate of the tripod in a way that all the sensors were aligned with its vertical axis. The frame supporting the sensors (i.e., the head of the tripod) could be moved around a horizontal axis to make the tripod's head perform a pitch rotation. It is worth mentioning that roll and yaw rotations were blocked on the tripod, thus allowing only pitch variations. A spirit level was used to ensure that the tripod plate was horizontally aligned with the ground. Additionally, the structural details of the tripod used in this work are detailed in Table 2.2. Regarding the sensors, the range readings were acquired using the

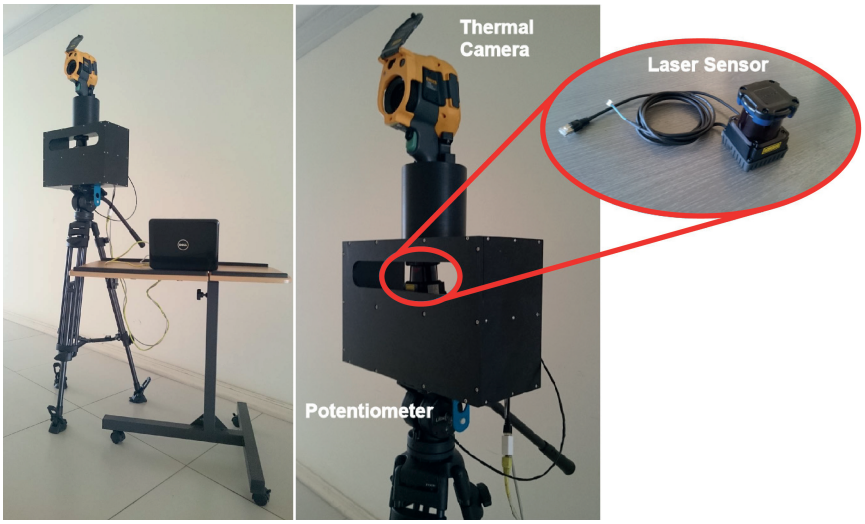

FIGURE 2.7: Placement of sensors on the commercial tripod. Left figure shows the hardware setup, and right figure shows the sensors (IR camera and LiDAR) mounted on the tripod. (Yandun et al., 2016b) © 2016 Elsevier.

TABLE 2.2: Structural characteristics of the sensing system. (Yandun et al., 2016b) © 2016 Elsevier.

Tripod Tilt Angle	from -80^o to $+90^o$
Tripod's plate height [1]	1.03 m
LiDAR height [1]	1.21 m
Camera height [1]	1.50 m
System weight	11.55 kg

[1] Measured from horizontal ground with the tripod supports completely retracted.

HOKUYO UTM-30LX-EW laser scanner (HOKUYO Automatic Co., Japan), which is well suited for outdoor measurements. Its maximum range is 30m, with a 270^o field of view, angular resolution of 0.25^o and 3mm of accuracy. The thermal camera is a hand held type Fluke Ti400 (Fluke Corporation, USA). The image has a resolution

of 320 × 240 pixels, spanning 24 ^{o}C × 17 ^{o}C of field of view (horizontal, vertical). The temperature range cover from -20^{o}C to 1200^{o}C, with an accuracy of ±2^{o}C. To estimate the angular position of the sensors while collecting the data by manually handling the tripod, a potentiometer was attached to the transverse axis of the tripod (at its head). This potentiometer converted the pitch variations ofthe head ofthe tripod into a voltage signal, which is received by a micro-controller and later synchronously recorded along with each LiDAR scan in order to have pitch information

2.2.2 Thermal and LiDAR fusion

The architecture of the implemented software is schematically summarized in the Figure 2.8. Data processing and final visualization of the results were performed using the Matlab R2014b programming environment. Additionally, the free software Image Composite Editor (ICE) from Microsoft Corporation was used to process the thermal images. Each stage in Fig. 2.8 is explained as follows:

- A second degree polynomial of the pitch variations as a function of the voltage was obtained via linear regression using experimental data. The model obtained is described in Eq.2.1, where $p(t)$ and $v(t)$ denotes the pitch angle and the voltage data, respectively, at each sample time t.

$$p(t) = a \times v(t)^2 + b \times v(t) + c \tag{2.1}$$

  The remaining pitch processing consisted of smoothing the estimations through a moving average filter (p_s), described in Eq. 2.2, where M represents the number of points used to calculate the average (M was set to 10)

$$p_s(t) = \frac{1}{M} \sum_{i=0}^{M-1} p(t_{k-i}) \tag{2.2}$$

- Each LiDAR scan is then associated with a pitch estimated value, which allowed to obtain a 3D data point cloud from the environment (for each scan and for a single view). Then, readings corresponding to angles outside a predefined field of view in front of the laser (same as camera horizontal aperture) were rejected automatically. This provided an initial rough correspondence between the laser and camera data.

- Additionally, the set of thermal images acquired manually when rotating the tripod, were stitched using the software ICE in order to obtain a single thermal picture of the tree for a single view (i.e., for a single tripod location).

- Once the thermal and laser data are available, a merging stage was performed by the *T+3D Single Frame algorithm* described in the next Section.

- Subsequently, all the *T+3D* single frames were matched in order to get a point cloud representing the full orchard characterisation where each Cartesian point has a temperature value associated with it. Partial reconstruction of the tree is also allowed, selecting specific frames to be registered. However, in this case,

a 360 degree view of the orchard was adopted for each experimentation, as it will be shown later.

- The global reference system of the sensors is positioned at the first location of the tripod in the environment. All later readings are referenced to that point.

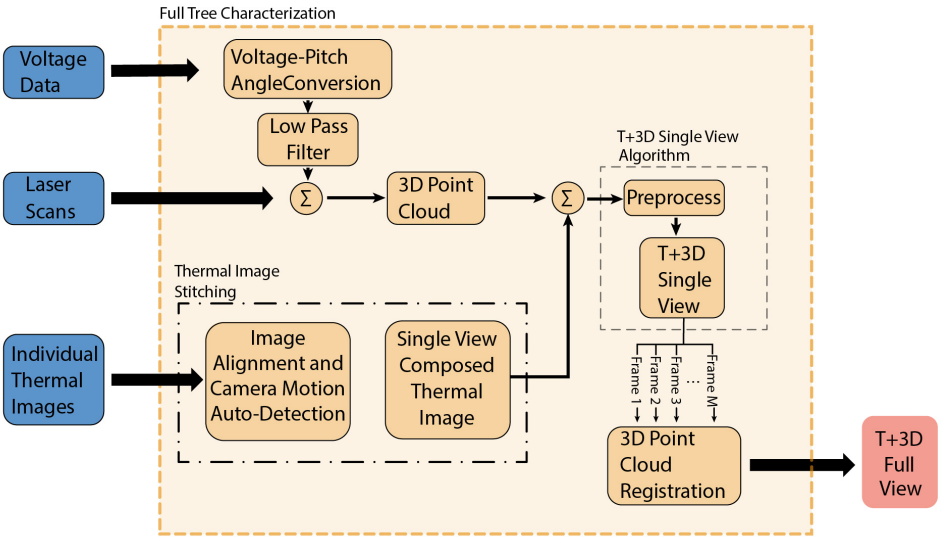

FIGURE 2.8: Software architecture for the T-3D characterisation. (Yandun et al., 2016b) © 2016 Elsevier.

Fusion of exteroceptive information: T+3D single frame

Raw data from the range measurements was first processed in order to classify the points that are more likely to be part of the tree. To achieve this, a Mahalanobis-distance based classifier was used (Fraser et al., 2003), which takes into account the sparsity (related to height and width) of each dimension of the tree. The training data consisted of a set of point clouds corresponding to typical trees (avocado trees for our experimental tests). Thus, points whose distances to training data are smaller than a previously defined threshold were considered part of the tree, otherwise they were rejected. Regarding the thermal images, the region that corresponds to the orchard was segmented by means of a process consisting of three steps. In the first step, a rough manual selection of the tree was required. Later, this selection was used as an initial state for an active contour algorithm (Chan and Vese, 2001), which allowed a refined segmentation of the foreground (tree) and the background in the image. Subsequently, the temperature of each pixel that belongs to the tree was obtained using the transformation described in Eq. 2.3.

$$T(x,y) = I(x,y) \times \frac{T_{max} - T_{min}}{255} + T_{min} \tag{2.3}$$

where $T(x,y)$ is the temperature of a pixel located at position x, y in the thermal image, I is the intensity value of that pixel, which ranges from 0 to 255 (one-byte grayscale image), $T_{min} = 5^oC$ and $T_{max} = 40^oC$ correspond to the predefined temperature range of the thermal camera.

Once thermal and spatial information were processed separately, the fusion algorithm was applied. It maps the points previously classified as tree to an occupancy grid with the same resolution and dimensions of the segmented thermal image. In this way, the grid and the image have the same number of cells/pixels. Following, the temperature of each pixel that belongs to the tree was associated with the cells of the grid, according to their position in the image. This mapping process was done in batches of points, for different values of depth. It is noteworthy that this algorithm relies on an accurate tree segmentation and classification from the thermal image and the point cloud, respectively. Accuracy is highly dependent on the covariance propagation of the measurements and the processing as shown by Auat Cheein and Guivant, 2014.

The above technique was performed for each view, providing thermal data for all laser scans of the trees. This information was later processed in order to characterise the entire orchard, using the algorithm presented in the following Section.

T+3D Full View Reconstruction

To obtain a complete view of the tree, all single view frames must be referred to a common global reference frame. Using a GNSS antenna to geo-reference the data might simplify this task. However, as stated earlier, the occlusion of the GNSS signal in many agricultural environments lead to the need of implementing an alternative way to solve the localization problem. In order to fully characterise the orchard in absence of GNSS signal, an Iterative Closest Point (ICP) algorithm was implemented (Choi et al., 2012). It first estimates the translation and rotation of each single view and then applies those transformations to get a point cloud of the entire tree. To perform the matching in an efficient way, the searching of the closest point was done using the *Nearest Neighbour Search* algorithm with the input data sorted as a K-D tree (Elseberg et al., 2012). The processing of each view was done consecutively, i.e. the i^{th} frame was transformed into the reference of the previous one. Since the ICP methods are highly dependent on the locations where data was acquired, two tripod locations were apart maximum one meter from each other. The latter was empirically deduced, since the ICP algorithm might become inconsistent when two different scans do not share enough common information (Chetverikov, Stepanov, and Krsek, 2005; Salvi et al., 2007). After the processing stages, a single cloud point representing the entire orchard is obtained as a full T+3D image, where each point has a temperature value associated.

2.2.3 Laboratory Validation

In order to validate the thermal and spatial correspondence of the system, several trials on an ornamental plant were performed. Twelve representative leaves from the plant were randomly selected: 4 from the top (T), 4 from the middle (M) and 4 from the bottom (B) sides. For each one, up to 9 trials every thirty minutes were done, as the plant was exposed to a commercial 250 watts infra-red lamp in laboratory conditions. This methodology ensured a stable ambient temperature and a long term experimentation. At each trial, the *T+3D* reconstruction was obtained, as well as the temperature from each representative leaf using an *EXTECH* 421305 K-type thermocouple (Extech Instruments Corporation, USA). It is worth mentioning that

the thermocouple required approximately 1 or 2 minutes of transient response, to give a stable measurement. Given the previous context, the validation of the system was performed in two ways: spatial and thermal. For the spatial validation, the fact that some leaves had more heat radiance from the lamp and could be easily distinguished was exploited. For this reason, leaves 2 and 3 from the top (2T, 3T in Fig. 2.9), and leaf 3 from the middle (3M in the same figure) of the plant showed to be warmer than the rest of the canopy. Figure 2.9 shows the outcome of the system, which matches the corresponding leaves with their temperature, representing the points of that leaves as hot sectors in the canopy. Moreover, the reconstruction led to recognize each testing leaf in the point cloud by visual inspection. For the thermal validation, single

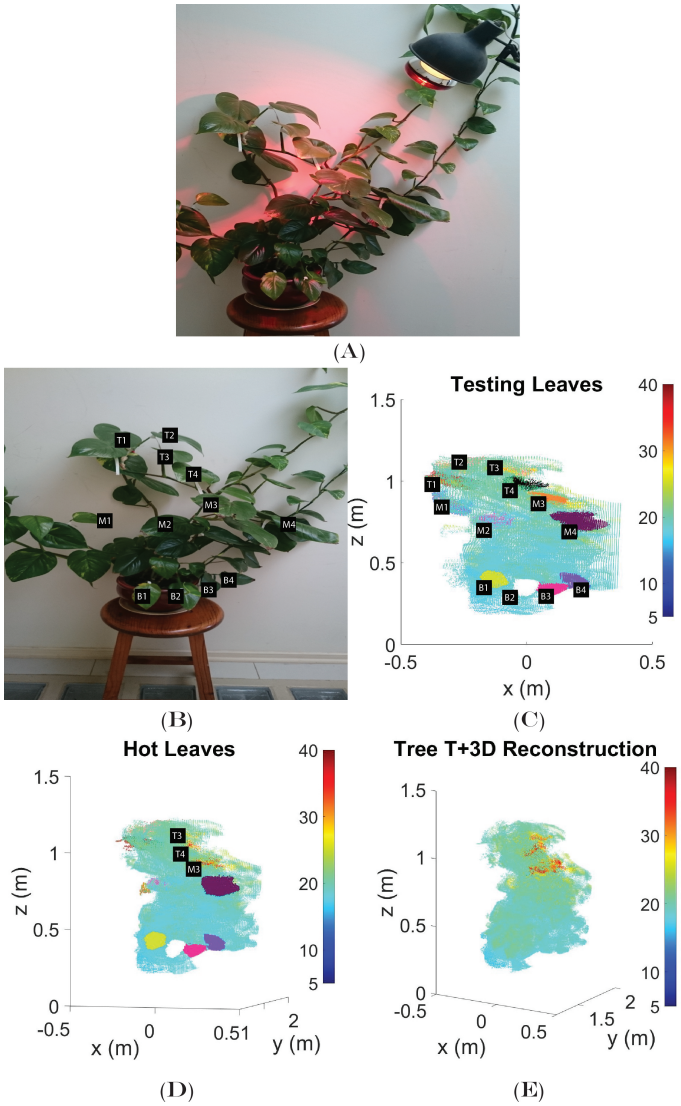

FIGURE 2.9: Thermal and geometrical characterization of the testing plant. RGB image of the experimental plant (A), labelling of the sample leaves (B), sample leaves visually detected within the point cloud (C), leaves with higher temperature due to direct light illumination (D), resulting thermal and geometrical characterization of the plant (E). Points reaching the wall behind the plant and leaves were manually filtered. (Yandun et al., 2016b) © 2016 Elsevier.

images of each leaf with the camera were additionally acquired. Subsequently, the temperature of a central sector of each sample was obtained by means of the camera manufacturer proprietary software (*Smart View*). This allowed to obtain a set of representative temperatures of each leaf, which were compared to the thermocouple measurements. For the assessment of the thermal data, the boxplots of the two datasets were obtained (Fig. 2.10). It can be graphically noted that both measurements show a similar behaviour. Furthermore, the mean and standard deviation of the differences between the thermocouple and camera readings are 1.48^oC and 1.26^oC, respectively, which are acceptable values between these two sensing methodologies. The spatial

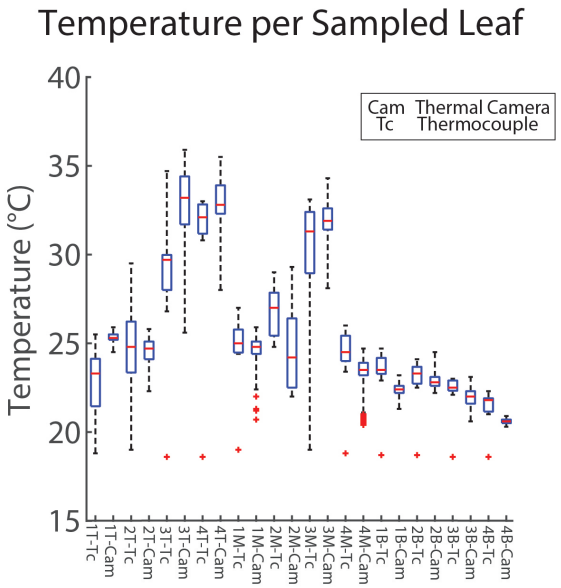

FIGURE 2.10: Statistical behaviour of the temperature measurements of the sampled leaves after nine trials. Temperature results shows consistency between the thermocouple and the sensed temperature. (Yandun et al., 2016b) © 2016 Elsevier.

and thermal results of the laboratory tests allowed us to validate the system and conclude that it is suitable for thermal and three dimensional reconstruction of plants.

2.2.4 Field Testing

The field tests were performed in two ways: using a single tree and a entire row of avocado trees. The plantation under study was located in the township of La Cruz, in the Valparaiso Region, Chile ($32^o49'51.2"$ S, $71^o14'24.7"$ W). The crop was being monitored by the Chilean National Institute of Agricultural Research (INIA in Spanish) using RGB and NIR imagery from the *Fatsat Charlie* satellite. The individuals used for this work were well irrigated five-year old leafy trees of the Hass variety, planted each 3 meters in a row pattern, with a separation between rows of 5 meters.

The ambient conditions during field experimentation varied from a cloudy morning to clear sky in the afternoon. That day, the sun rose at 06:30 am, but the scanning of the eastern side of the single tree started at 11:00 am and ended at 12:00 pm. The

western side, on the other hand, was scanned from 12:00 pm to 13:00 pm. Further, the alley data acquisition started at 13:30 pm and ended at 16:00 pm. The average ambient temperature (T_{amb}) in those schedules according to meteorological data provided by INIA was 18.35^o, 21.50^o, and 23.20^o, respectively.

T+3D fusion: single view (individual tree)

The tree under evaluation is shown in Figure 2.11. Data acquisition consisted of taking seventeen *T+3D* single frames in order to completely round the tree. The tripod was located facing the canopy at a distance of approximately one meter to ensure that the tripod movement let the laser beam reach the top leaves. This distance was defined making a first scan and then manually verifying in the resulting point cloud that the entire tree was scanned. Figure 2.12 shows the results of the fusion algorithm for

(A) (B) (C)

(D) (E) (F)

FIGURE 2.11: Several snap-shots from east to a west of the tree under evaluation. Each image corresponds to the resulting *T+3D* frames shown in Fig. 2.12: frame 2 (A), frame 4 (B), frame 7 (C), frame 9 (D), frame 13 (E) and frame 15 (F). The location of the frames respect to the tree are the same as depicted in Fig. 2.14b. (Yandun et al., 2016b) © 2016 Elsevier.

six frames. It is interesting to note that the eastern side of the tree (frames 1-9) is colder respect to the western side (frames 10-17). This outcome reflects the climatic

conditions of the experimentation day along with the direct insulation received by the tree, since the first nine frames were acquired in the morning, whereas the remaining frames were acquired in the afternoon.

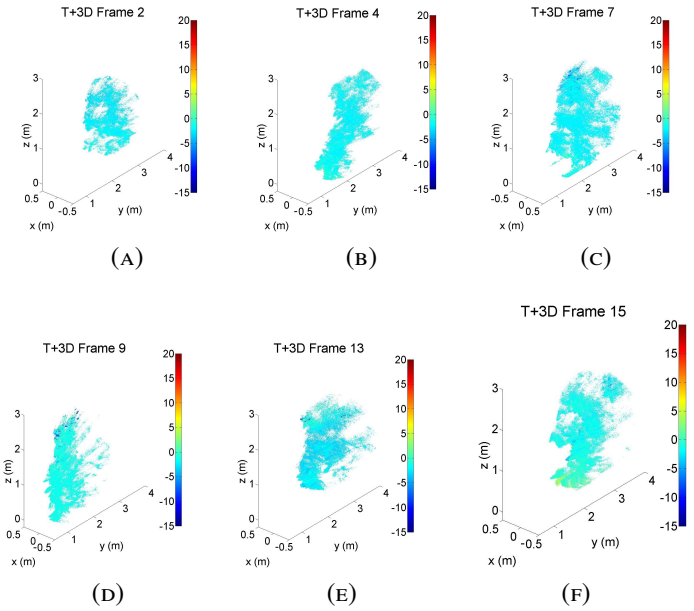

FIGURE 2.12: Resulting *T+3D* for single views, shots from east (A) to west (F). Frames 1 to 9 correspond to the eastern side of the tree, whereas the remaining frames correspond to the western side. The location of the frames respect to the tree are the same as depicted in Fig. 2.14b. The temperature scales show the difference of the punctual temperature estimations with the ambient temperature. (Yandun et al., 2016b) © 2016 Elsevier.

It is important to note that some sectors in the point cloud have a higher (bottom) or colder (top) temperature. This is produced by mixed pixels from the soil or the sky, which were misclassified in the thermal images. However, this phenomenon appears only in particular frames and an analysis of the temperature distribution in the frame shows that these points are outliers, and can be neglected. In this context, Figure 2.13 presents the temperature distribution as a boxplot for each frame, which is used to identify the outliers, and the representative temperatures for each case. This Figure, is later used for comparing the output using the data of the LICOR instrument. Each box in Fig. 2.13 corresponds to a single *T+3D* reading. Frames 1-9 correspond to the east side of the tree, whereas frames 10-17 correspond to the west side of the tree.

T+3D fusion: full view

In order to fully characterise the single tree, 17 frames were needed; whereas the scanned avocado alley required a total of 41 frames. The total number of scans required for obtaining a complete characterisation, varies depending on the size of the individual tree or the alley. As stated in Section 2.2.2, the distance between locations of the tripod for each scan was maximum one meter. This constraint made the number of frames needed to fully round the tree a variable value (i.e. a bigger

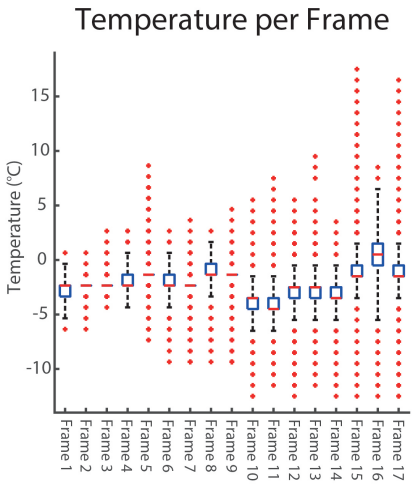

FIGURE 2.13: Behaviour of the temperature in each face of the tree. The location of the frames respect to the tree are depicted in Fig. 2.14b. Temperature scale shows the difference of the punctual temperature estimations with the ambient temperature. (Yandun et al., 2016b) © 2016 Elsevier.

tree would require more frames to obtain a full view, since all the tripod locations are always separated a maximum distance of one meter). Figure 2.14b depicts a top view of the tree and shows the positions where the tripod was placed. The experiment started at frame 1 (red dot) and subsequently the tripod was moved around the tree in a counter-clockwise path.

The output of the system is presented as a 3D interface, which offers a complete morphological characterisation of the tree/row. This information can be later used to perform a spatial analysis of the tree characteristics (e.g. leaf area index, treetop volume estimation). Furthermore, the system incorporates a color code for the temperature behaviour in the orchard and the temperature of each point in the cloud. These two characteristics provide a coarse and fine analysis tool for the thermal status of the plant.

Figure 2.14 shows the full *T+3D* characterisation of a single avocado treetop. In this case, each point of the cloud has associated the difference between the average ambient and measured temperatures. For the eastern side, this value was -1.75 ± 0.95^oC ($T_{amb} = 18.35^oC$), whereas for the western side was -2.39 ± 1.93^oC ($T_{amb} = 21.50^oC$). These results are expected, since when the ambient temperature increases, the leaves responds in different ways according to its physiological status, causing a greater dispersion in the difference between the ambient and measured temperatures.

Performance comparison with a *LICOR 6400*

The researchers of INIA periodically perform a leaf thermal analysis in avocado groves using a photosynthesis measurement IRGA LICOR 6400 device. Therefore, the results of the proposed system were compared with the ones provided by the LICOR 6400 on the same tree and during the same trial shown in Fig. 2.12. Since each leaf was analysed individually, six leaf samples from each side were taken: six from

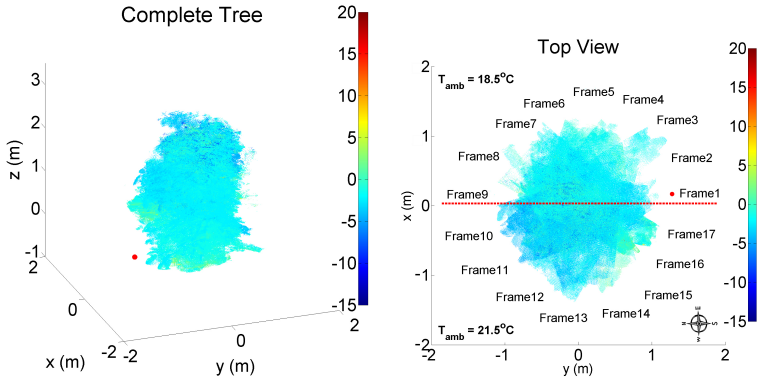

(A) (B)

FIGURE 2.14: Resulting *3+TD* view for the complete tree. The colorbars show the difference between ambient and canopy temperatures. Additionally, the solid red dot represents the first frame whereas the remaining frames are counted counter-clockwise. The red dashed line, in the top view, approximately separates the eastern and western side of the tree, with the average temperature indicated for each case. (Yandun et al., 2016b) © 2016 Elsevier.

the west side of the tree and six from the east side as we were scanning the selected tree. The samples were selected randomly between the leaves located in the periphery of the tree, exposed to the sunlight, healthy and without discolouration. Each measurement required approximately 10 minutes of preparation and the batteries of the device allowed for two hours of operation. Figure. 2.15 shows the results obtained by the LICOR 6400 in terms of boxplots which allow a statistical interpretation of the temperature measurements. In Fig. 2.16 the temperature results obtained by

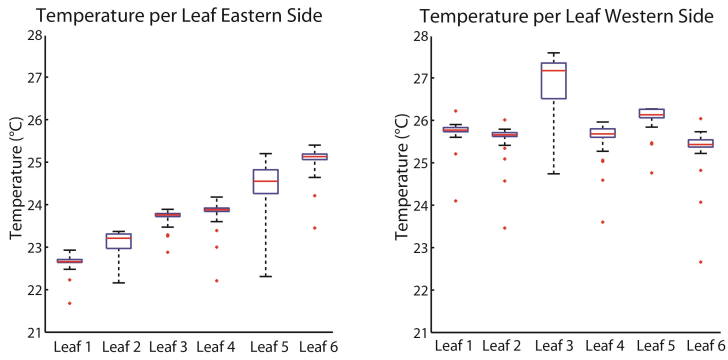

(A) (B)

FIGURE 2.15: Boxplots of the temperature results obtained by the LICOR 6400 for both east and west side of the canopy. The eastern side of the tree was scanned with the proposed system and the LICOR device in the morning, with an average ambient temperature of $18.35^{o}C$. The western side, was analysed in the afternoon when the average ambient temperature was $21.50^{o}C$. (Yandun et al., 2016b) © 2016 Elsevier.

the LICOR 6400 (left) and the proposed system (right) per each side of the tree

are compared. It is to be noted that the results obtained by the LICOR 6400 are biased about 5^oC. As can be seen in Fig. 2.14, the proposed system did not register temperatures above 24^oC as the LICOR 6400 did. It is important to mention that according to weather readings during the experimentation period, the average ambient temperature did not exceed 19.4^oC and 23.7^oC, for the morning and afternoon, respectively. Therefore, we discarded the possibility of having measured the outer leaf temperature with the LICOR instrument. Instead, and according to its user manual, the chamber in which the leaf is captured by the device is not at ambient temperature, but at the device's inner temperature. Thus, the transpiration results that can be obtained using the LICOR 6400 do not correspond to the transpiration at ambient temperature of the plant. The latter could open new research and application lines for this case of study.

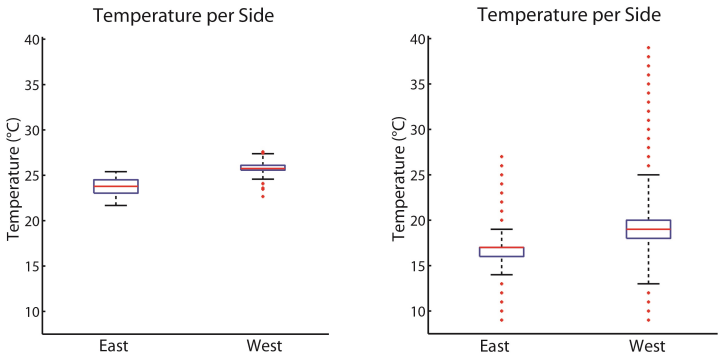

(A) (B)

FIGURE 2.16: Boxplots of the temperature results obtained by the LICOR 6400 (2.16a) and the proposed system (2.16b) for both east and west side of the canopy. The eastern side of the tree was scanned with the proposed system and the LICOR device in the morning, with an average ambient temperature of 18.35^oC. The western side, was analysed in the afternoon when the average ambient temperature was 21.50^oC. (Yandun et al., 2016b) © 2016 Elsevier.

2.2.5 Full Alley Reconstruction

As a long term use of the system, Fig. 2.17 shows a snap-shot of the avocado grove where the experimentation took place (Fig. 2.17a) and the corresponding full *T+3D* reconstruction of the alley (Fig. 2.17b). As can be seen the proposed system is able to thermally and geometrically reconstruct part of the alley without using GNSS receivers.

2.3 Contributions

The two case studies presented in this Chapter provided novel applications of sensing for crop phenotyping. In addition to study three methodologies for canopy volume estimation (a topic widely studied in the literature), the first case study also aimed

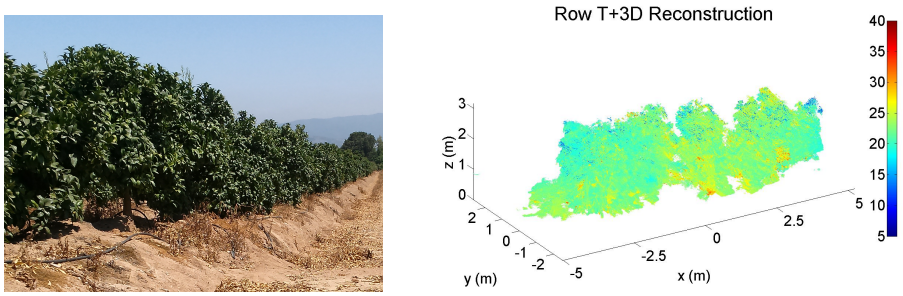

(A) (B)

FIGURE 2.17: Snap-shot of the avocado grove (A) and full T+3D reconstruction of an entire alley (B). (Yandun et al., 2016b) © 2016 Elsevier.

to improve the overall scanning time. Taking advantage of the symmetry of pear trees, it was found that accuracy does not decrease in a big extent when scanning only one side of the crop row. Thus, the partial knowledge of the crown could lead to a more efficient management of the service unit's resources (e.g., it would not need to traverse all alley-ways in the grove).

The second case study presented a new sensor integration technology for thermal and morphological characterization of fruit groves. The proposed system joined LiDAR and thermal information to build a 3D point cloud where each point has a temperature associated. This innovative tool is intended to be used by a farmer to analyse water stress, volume or leaf area coverage in the vegetation.

The publications derived from the research work presented in this Chapter are:

- Auat Cheein, F. et al., 2015. Real-time approaches for characterization of fully and partially scanned canopies in groves. Computers and Electronics in Agriculture, 118, pp.361–371.

- Yandun, F. et al., 2016. LiDAR and thermal images fusion for ground-based 3D characterisation of fruit trees. Biosystems Engineering, 151, pp.479–494.

Chapter 3

Image Analysis for Terrain Classification

Descriptively characterizing the terrain allows the robot to know beforehand the upcoming terrain and to discern whether a region is traversable or not, based on the latest information acquired by the sensors (Ho, Peynot, and Sukkarieh, 2013). Furthermore, satisfactory results in typical agricultural activities including seeding, fertilizing, or ploughing require the robot to be capable of distinguishing the upcoming terrain (Ball et al., 2016). This Chapter describes the use of infra-red and color data acquired from a low cost sensor to classify the terrain in front of a mobile robot using image processing and machine learning methodologies. In addition to propose a low cost solution, the methodology presented aims to overcome certain issues which arise when working in field (e.g., illumination conditions or vibration). Thus, a solution that balances robustness and cost is designed and evaluated. Five types of terrain were recognized: sand, grass, pavement, gravel and litterfall & straw- covered.

This Chapter is organized as follows: Section3.1 describes the approach used for image processing along with the architecture of the system. Section 3.2 introduces the basic ideas of support vector machines, and how it can be used to address a multi-class problem. Finally, in Section 3.3, the experimental tests and their corresponding results are detailed.

3.1 Image processing for feature extraction

Image processing theory provides a wide variety of descriptors to obtain a specific and detailed information about an image or its content. Available algorithms include speeded-Up robust features (SURF), scale-invariant feature transform (SIFT), features from accelerated segment test (FAST), Binary Robust Independent Elementary Features (BRIEF), oriented FAST and rotated BRIEF (ORB), local binary patterns (LBP), among others (Bishop, 2006). With a certain amount of processing, all of them are suitable for terrain classification purposes, as reported in the literature (Zou et al., 2014). However, the approach adopted in this thesis is based on the way that humans distinguish between different terrain types: perceiving their texture. Since color is an important, but not determinant characteristic (specially in field conditions), infra-red images are employed, leaving color only as an additional feature in the detection. As will be shown later, robustness in real operation conditions is achieved, with reduced computational cost. For this application, the texture description methodology proposed by Varma et al., 2009 was employed. Figure 3.1 shows

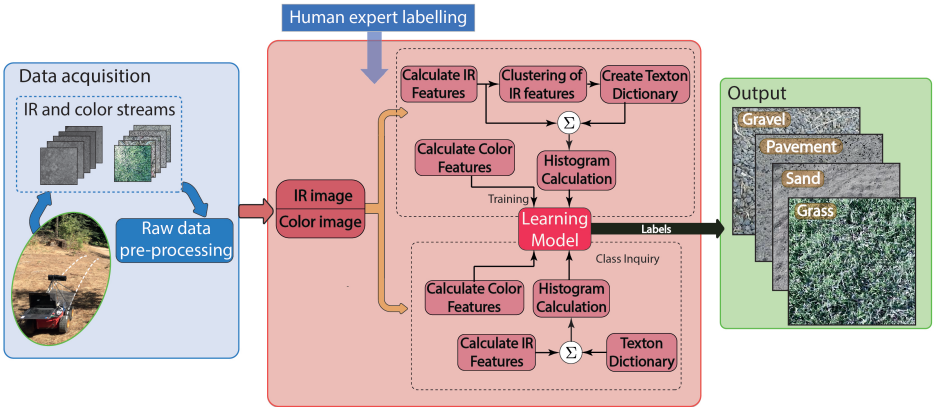

FIGURE 3.1: Block diagram of the terrain recognition system. (Yandun et al., 2018) © 2018 Elsevier.

a diagram that summarizes the overall terrain recognition system. All of the blocks depicted there are detailed in the following Sections.

3.1.1 Texture Characterization - Local Descriptors

Texture description can be achieved by identifying its distinctive pattern present in the image. Thus, it is necessary to get local descriptors for each pixel using not only its intensity, but also the values of its neighbours. Following this idea, various methods mainly based on filter responses have been proposed Varma and Zisserman, 2005. To achieve illumination and viewpoint invariances, various filter banks can be employed (Leung and Malik, 2001; Schmid, Schmid, and Schmid, 2001). However, to also get rotational invariance in a lower dimensional space, the maximum response (MR) 8 filter can be employed. This filter bank consists of a Gaussian, a Laplace of Gaussian, an edge and a bar filters, the last two at 3 scales and 6 orientations per scale, as shown in Figure 3.2. The filtering output is obtained by keeping the maximum responses of the edge and bar filters across all orientations, which allow to achieve rotational invariance (Varma and Zisserman, 2002). While this filtering approach is suitable

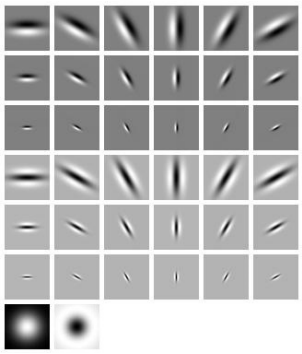

FIGURE 3.2: Maximum Response 8 filter bank. From top to bottom: An edge filter at 6 orientations and 3 scales, a bar filter at 6 orientations and 3 scales. The last row shows Gaussian and Laplacian of Gaussian filters. (Yandun et al., 2016a) © 2016 Elsevier.

in theory, implementation is challenging specially for large images. Convolving

the image with the 38 filters involves a computational cost that limits a practical application. To overcome this issue, the equivalent patch-based concept presented by Varma et al., 2009 was used instead. It is reported to achieve the same local description results of the filtering approach. This alternative methodology considers that textures can be considered as realizations of Markov Random Fields (MRF), as described by Li, 2009. Formally, given a rectangular region of interest (ROI) S, and a set of m random variables defined in S which can take values $f = \{I_1, I_2, ..., I_m\}$ (e.g., pixel intensities), for a MRF it can be written:

$$p(I_i|I_{S-\{i\}}) = p(I_i|I_{N_i}) \tag{3.1}$$

where I_i is the value of pixel i, $I_{S-\{i\}}$ represents the values of all pixels in S except i, and I_{N_i} stands for the set of pixel values in the $N \times N$ pixel neighbourhood (excluding the pixel i). Thus, the local description of a single pixel can be represented by the raw intensities of an $N \times N$ square neighbourhood of that point.

3.1.2 Feature Engineering

Features are the main characteristics serving as inputs to the learning algorithm. They have to highlight the special characteristics of each class. Practically, any information within the available data can be used with this purpose. For example, intensity value of pixels in an image, filtering outputs or results from algebraic operations performed to the data. In practice, features from different sources normally have different dimensionality, which is a problem since larger-valued features would fade the others. To overcome this issue, all values are often normalized so that they are equivalent from the learning point of view. This feature engineering methodology is essential in the "old" paradigm of machine learning, where they are designed using the practitioner experience. In contrast, in the -relatively- new learning trends using deep neural networks, the most relevant features are automatically detected and characterized internally by the algorithm (Bishop, 2006).

In this thesis, the “old” learning paradigm of feature engineering is employed, mainly for two reasons: the type and amount of information available. Using deep neural networks or similar methods usually implies large training datasets of color images. Further, designing a deep architecture to take full advantage of the available data (infra-red, color and depth) is an entire research area which goes beyond this work.

To describe the feature formulation, it is first necessary to introduce the concept of *texton*. A *texton* is a cluster center in the texture descriptor space. For a single class, local descriptors from all pixels in the image (or images) are clustered using the k-means algorithm. The K centres obtained as a result are the *textons* which define a single class. This representation can be intuitively interpreted since texture can be considered as repetitive patterns within the image. Thus, the cluster centres correspond to the most representative descriptors of the given pattern.

Subsequently, the *textons* from each class are stacked in a single array forming a dictionary. Finally, a single image provides a feature vector of its class in form of a histogram, which is built by labelling each texture descriptor per pixel with the closest *texton* in the dictionary. In other words, the feature space is created by

n^{th}-dimensional vectors ($n = K \times number\ of\ clases$) representing the frequency of occurrence of each dictionary element in the descriptor space of the image.

In parallel to the previous processing, color information was employed to create an additional small feature vector. To this aim, the original RGB image was first converted to the -Comission Internationale de l'Éclairage (CIE) 1976- L*a*b* colorspace (Schwiegerling, 2004). The L* and b* components were left out for two reasons: i) to attenuate the effects of the lightning conditions, and ii) it was found in the development stage that they did not contribute to distinguish between classes. Thus, only the mean and variance values of the a* component were employed. In addition, the proportion of green in the image was calculated as: $\frac{G}{R+G+B}$, where R, G and B are the sum of intensity values per pixel for the R, G and B channels, respectively. When using depth streams in the validation tests, depth feature vectors consisted of four statistical measurements of roughness: mean, root mean square, skewness and kurtosis, as calculated by Marinello et al., 2015.

To complete the feature generation these descriptors (either depth or color) have to be aggregated to the texture feature vectors to form the input training and testing data in a multi-class support vector machine (SVM) classifier.

3.2 Multi Class Learning

Labelling a query sample as one of different classes is a multi class learning approach. At difference from multi-label classification, only one label can be assigned/predicted for a single instance. While various of the algorithms in the state of the art naturally deals with this problem (e.g., k-nearest neighbours or decision trees), others are formulated in a binary way . In this thesis, a support vector machine (SVM) learning approach was adopted since it is robust to outliers and it has proven to work well with features in high dimensional spaces (Kecman, 2005; Ben-Hur and Weston, 2010). Further, SVM have shown the capability to generalize well in even with small and medium training datasets (Mountrakis, Im, and Ogole, 2010).

3.2.1 Binary SVM

Support vector machines comprise a methodology for supervised learning with a mathematical approach, rather than a heuristic one. The main idea is based on the assumption that input data consists of linearly separable patterns. Given a set of training examples of two different classes, the training algorithm finds an optimal hyperplane that maximizes the margin dividing both classes.

Formally, assuming that the problem is linearly separable, the classification can be addressed using a hyperplane (in a n dimensional space) of the form:

$$\boldsymbol{W}^T \boldsymbol{x} + b = 0 \tag{3.2}$$

where $\boldsymbol{x} \in \mathbb{R}^n$ corresponds to training or testing datapoints and $\boldsymbol{W}^T$ is the normal vector to the hyperplane . The training dataset is defined as the N pairs of input vectors and their corresponding value/label: $\mathcal{D} = \{(\boldsymbol{x_1}, l_1), (\boldsymbol{x_2}, l_2), \ldots, (\boldsymbol{x_N}, l_N)\}$, with $l \in \{-1, 1\}$. Query points of the testing set are classified depending on whether they lie

"above" or "under" the plane 3.2. The model is then built stating an optimization problem which finds a plane that maximizes the separation between the classes.

Consider the closest data point $\boldsymbol{x_{near}}$ to the plane, its distance can be computed geometrically. Given a point belonging to the plane $\boldsymbol{x_p}$, such distance is the projection of $\boldsymbol{x_{near}} - \boldsymbol{x_p}$ on $\boldsymbol{W}$ (recall that $\boldsymbol{W}$ is orthogonal to the plane). Thus,

$$d = |\frac{\boldsymbol{W}}{||\boldsymbol{W}||}\left(\boldsymbol{x_{near}} - \boldsymbol{x_p}\right)| = \frac{1}{||\boldsymbol{W}||} \tag{3.3}$$

where the plane equation was used and the fact that $|\boldsymbol{W}^T\boldsymbol{x_{near}} + b| = 1$. The last result comes from the fact that rescaling $\boldsymbol{W}$ and b does not modify the plane nor its distance to $\boldsymbol{x_{near}}$. In this case, considering that all points are aimed to be correctly classified, they satisfy the constraints

$$l_n(\boldsymbol{W}^T\boldsymbol{x} + b) \geq 1, \qquad for\ n = 1, 2, \ldots, N \tag{3.4}$$

Finally, the model is obtained by maximizing $d = \frac{1}{||w||}$, which is equivalent to solve

$$\underset{\boldsymbol{W},b}{\arg\min} \quad \frac{1}{2}||\boldsymbol{W}||^2 \tag{3.5}$$

subject to the constraints given by 3.4. Note that including the factor $\frac{1}{2}$ does not alter the minimization results. It is included for convenience to later solve the problem, which is in fact a quadratic programming optimization. Further details about the solution of this problem can be obtained in Bishop, 2006 and the references therein.

This formulation makes of SVM a non-probabilistic binary linear classifier. Thus, any likelihood or confidence score about the classification can be obtained with the original setting, in contrary to other methods (e.g., neural networks). Finally, when working in non-linear problems, SVM allows to employ the *kernel trick*, which consists in mapping the input data into a higher dimensional space where it may be linearly separable (Hwanjo and Sungchul, 2012).

3.2.2 Multi Class SVM

To use a SVM approach in a multi-class learning, the most common strategy is to split the problem into small binary classifiers. There are two main heuristics to perform this reduction: one vs the rest and one vs one.

One versus the rest strategy consists in training a single classifier per class: the actual samples from a specific class are positive examples, while the rest (of all remaining classes) are considered negative. Thus, if C different classes are learned, there will be C classifiers. This approach requires that each classifier produce a score to obtain a single label. Otherwise, discrete class labels can led to ambiguities when various classifiers provide positive predictions for the same sample. Since SVM do not provide a likelihood or prediction confidence, such score can be the distance of the query point to the hyperplane. In this way, the label from the classifier with the major distance will be selected. Despite of being widely used in various learning applications, this strategy has to important drawbacks: i) the score among classifiers

is not guaranteed to be in the same scale, and ii) since the amount of negative training examples is bigger for each classifier, the learned model is unbalanced, in general.

One versus one approach, in the other hand, trains a classifier for each possible combination of two classes. This produces $C(C-1)/2$ classifiers from which a final label is obtained using a voting scheme. At prediction time, the query sample is given to all the classifiers, and the class with the majority of positive detections is selected as final output. Similarly to the one vs one approach, an ambiguity arises when a class receives the same amount of votes, however, the same score technique can be employed to break the tie.

In this work, the *one vs one* multi-class approach of the SVM algorithm was epmloyed due to its balanced training characteristic and applicability for various sizes of datasets, as shown by Hsu and Lin, 2002.

3.3 Experimental Results

To test the proposed system, the second generation of the Kinect device (Microsoft Corporation, USA) was employed. The sensor provides infra-red (IR), color and depth streams at a maximum of 30 frames per second. In order to measure infra-red reflectance and estimate depth, it uses an IR camera with 512×424 pixel resolution. On the other hand, the color camera has a 1920×1080 pixel resolution. Infra-red measurements are based on active sensing, whereas depth is estimated based on a time of flight principle. It basically consists in measuring the amount of light received by synchronized detectors working in a complementary mode. This configuration provides increased noise rejection and better accuracy when compared with its predecessor. In addition, the sensor has a built-in ambient light rejection that detects if a pixel is over saturated and resets the reflectance value measured by such pixel (Lau, 2013). These characteristics make the sensing device versatile and robust enough in a variety of outdoor applications.

Two experimental scenarios were used to validate and test the system: static and real-dynamic operation. The static setup was employed to acquire the development dataset (i.e., training and testing data to establish and evaluate the approach). It consisted in placing the camera facing downwards to grab fixed depth, IR and color frames. For each terrain type studied, 820 frames per class at different illumination conditions were collected. Once the system was tested and validated, the sensor was mounted on the mobile robot Pioneer 3-AT from Mobile Robots Llc, in such a way that it was pointing downwards and forward, obtaining a view of the terrain in a range of 0.15 m to 0.9 m in front of the robot, as shown in Fig.3.3. For this reason, it was chosen to assign one label per image, since the dimensions of the space covered by each one did not allow to obtain representative patches of different terrains.

Field experiments to acquire the development dataset and subsequently run the trials with the robot were performed in three locations: i) the Botanical Garden of Viña del Mar, located at -33.048093^o latitude and -71.500135^o longitude; ii) the Sporting Club of Valparaíso, located at -33.024568^o latitude and -71.532815^o longitude; and iii) the Technical University Federico Santa María (UTFSM) central campus, located at -33.034796^o latitude and -71.595564^o longitude. These experimental locations included agricultural landscapes that together contained all the terrain types under evaluation. The trials were performed from 9 a.m. to 5 p.m. in summer and fall,

FIGURE 3.3: Experimental setup employed to test the proposed approach using a mobile robot driving through agricultural fields. (Yandun et al., 2018) © 2018 Elsevier.

obtaining shadowed and strongly illuminated scenes, as shown in Fig. 3.4. During this period, the robot was manually driven at maximum linear and angular speeds of 0.5 m/s and 2.44 rad/s respectively, acquiring and processing the IR and color streams at a frequency of 2 Hz.

FIGURE 3.4: Several snapshots of the robot driving through the experimental locations. Illumination varied from cloudy to clear sky conditions. (Yandun et al., 2018) © 2018 Elsevier.

The development and testing datasets were acquired at different illumination conditions and orientations, which caused various artefacts in the raw images, specially when excessive sunlight was present in the scene. To overcome this issue and to deal with the image boundary errors introduced by the sensor (Lachat et al., 2015), the raw images were cropped to retain only a central region of 300×300 pixels. In addition, the missing information in specific pixels was replaced with the average intensity value of its neighbours.

The first stage of the experimental tests consisted in evaluating the classification performance as function of the variables given by the sensor. To this aim, the development dataset (acquired with the static setup) was used. It consisted of 520 and 300 images for training and testing, respectively. This stage also included a 10-fold cross-validation of the classification model obtained. Table 3.1 shows the performance of the proposed approach for different combinations of IR, color and

depth streams, along with the features employed for each case. As can be noted, IR and color streams yielded the best results, whereas depth information did not contribute to improve the classification rates.

TABLE 3.1: Comparison of classification accuracy rates when employing different sensor streams to characterize the terrains. (Yandun et al., 2018) © 2018 Elsevier.

Characteristic	Features	Accuracy (%)
Infra-red	Texture description	92.57
Colour	Texture description of grayscale image	81.20
Depth	Texture description	34.61
Infra-red + color	Texture description of IR image + color features	95.40
Infra-red + depth	Texture description of IR image + depth features	89.13
Color + depth	Texture description of grayscale image + depth features	80.61
Infra-red + color + depth	Texture description of IR image + color features + depth features	91.04

In addition, Figure 3.5 shows the confusion matrix for the best validation case. The far right column shows the accuracy for the output terrain types, whereas the row at the bottom shows the accuracy for each true class. Finally, the cell at the right bottom shows the overall accuracy of the classification. The most *conflictual* terrains were sand and pavement since some images from pavement were very similar to sand, specially from the color point of view. However, the general performance of the proposed approach was accurate enough to test it under real conditions.

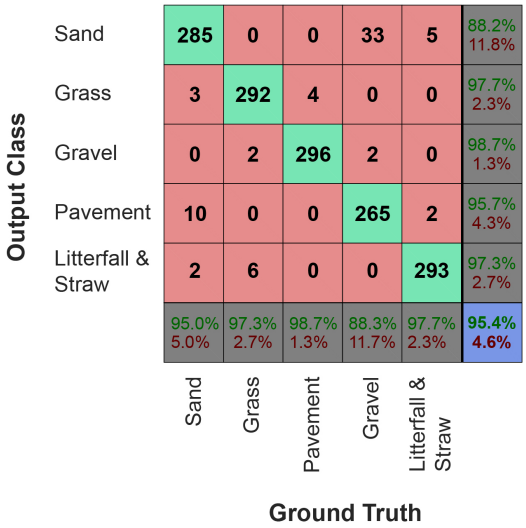

FIGURE 3.5: Confusion matrix for the best validation test. Only IR and color information from the sensing device was employed, yielding satisfactory detection rates. Two terrain types are often misclassified due to its visual similarity from the color and IR images. (Yandun et al., 2018) © 2018 Elsevier.

Once the proposed methodology was validated, the robot was driven through the three experimental landscapes a total of 17 times. In these trials, an average of 1000 frames were acquired in each drive of the robot. They were subsequently manually

labelled to obtain the ground truth. In addition, and to provide an illustration of the data acquired by the sensor, Fig. 3.6 shows a 3D-color reconstruction of partial paths followed by the robot. Part of the measurements are noisy due to sunlight incidence and vibration of the vehicle, but in general, the paths are visually well rendered.

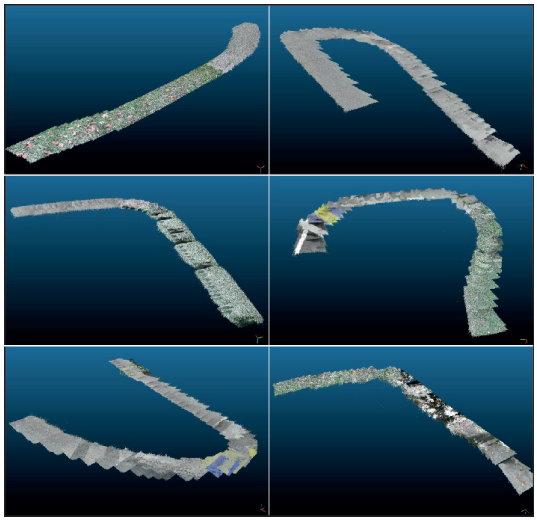

FIGURE 3.6: Three dimensional reconstructions of partial paths followed by the robot in different testing locations. The robot was manually driven on different roads in order to cover all the terrain classes classified in this work. In addition, the sensing device showed robustness when working outdoors, which allowed the scenes to be properly rendered. (Yandun et al., 2018) © 2018 Elsevier.

In order to evaluate the classification performance, 5 statistics including accuracy (acc), precision (prec), recall (rec), specificity (spec) and F-score (Fs), were calculated. They were obtained as described by Fawcett, 2006 and measure, in a complementary way, the quality of the true positive and true negative detections, taking into account all the classification outputs. The results in terms of these metrics, along with the distance covered for each testing trial are summarized in Table 3.2. As can be noted, reduced performance is exhibited for some trials. A deeper analysis of the images in each one showed important variation in true positive and false negative detection rates, which is mainly product of artefacts produced due to the camera movement. However, in general, the proposed methodology to classify terrain types based only on their appearance, with data acquired by a low cost sensor showed potential, even in presence of changing illumination and real driving conditions.

In addition to the previous results, Fig. 3.7 shows a confusion matrix that summarizes the outcomes obtained for all trials. In general, the proposed approach is able to achieve an accuracy of 83.00%, with reduced false positive and false negative detections for various terrain types in the field. However, the interclass similarity problem for pavement and sand observed in the validation stage is also exhibited in this case. Furthermore, sand and litterfall & straw also present this problem, which was not perceived in the validation stage. A close look into the images of these terrain types showed that some sandy locations were visually similar to litterfall & straw. Moreover, the most important reason to this outcome is the excessive black pixels

TABLE 3.2: Performance statistics for experiments conducted with the robot in real working conditions. A total of 17 trials were run within the three experimental locations, obtaining an overall of 15836 images. (Yandun et al., 2018) © 2018 Elsevier.

Trial	Accuracy	Precision	Recall	Specificity	F-score	Distance(m)
1	0.80	0.80	0.80	0.95	0.80	144.63
2	0.76	0.76	0.76	0.92	0.76	121.46
3	0.77	0.77	0.77	0.94	0.77	87.63
4	0.80	0.80	0.80	0.93	0.80	173.57
5	0.91	0.91	0.91	0.98	0.91	325.70
6	0.92	0.92	0.92	0.98	0.92	124.93
7	0.72	0.72	0.72	0.91	0.72	98.69
8	0.86	0.86	0.86	0.97	0.86	119.3
9	0.92	0.92	0.92	0.98	0.92	132.31
10	0.96	0.96	0.96	0.98	0.96	107.80
11	0.79	0.79	0.79	0.95	0.79	163.00
12	0.87	0.87	0.87	0.97	0.87	168.22
13	0.82	0.82	0.82	0.95	0.82	136.11
14	0.98	0.98	0.98	0.98	0.98	286.40
15	0.73	0.73	0.73	0.91	0.73	146.46
16	0.87	0.87	0.87	0.96	0.87	424.95
17	0.82	0.82	0.82	0.95	0.82	477.05
mean	0.83	0.83	0.83	0.95	0.83	Total Distance: 3238.21 m

with null information obtained in numerous images. Despite of these issues, the overall performance of the proposed terrain classification can be considered satisfactory, given the testing conditions and the low cost sensing hardware employed.

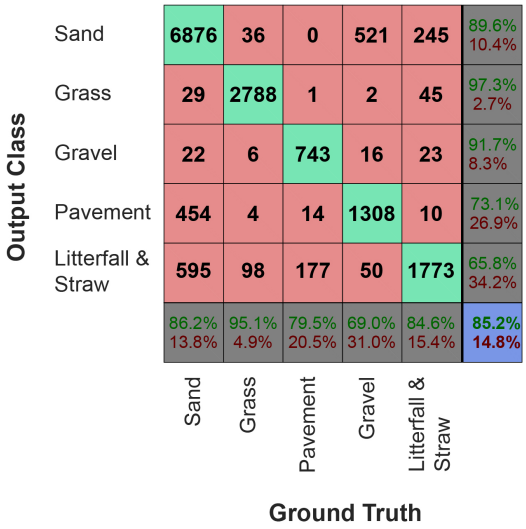

FIGURE 3.7: Confusion matrix that summarizes the overall performance of the proposed terrain classification methodology. It includes results of all tests (15836 images) conducted with the mobile robot through diverse agricultural scenes. Interclass visual similarity tends to decrease the classification performance, but in general, the terrains are correctly identified. (Yandun et al., 2018) © 2018 Elsevier.

In order to illustrate the path followed by the robot, along with the labels obtained

from the proposed approach, Fig 3.8a and Fig. 3.8b show a georeferenced and subsampled outcome for specific trials ran in two locations. They correspond to 65 labels from trials 6 and 15 which originally contained 647 and 870 frames, respectively.

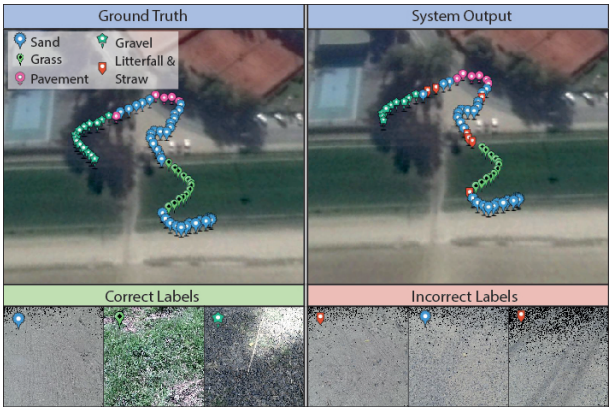

(A)

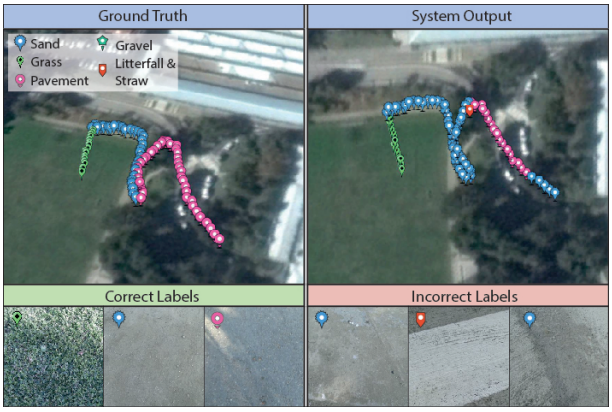

(B)

FIGURE 3.8: Georeferenced and subsampled outcome of the terrain classification system for two trials. The bottom row shows RGB images of the terrain captured by the sensing device, along with coloured markers representing the output of our classification system. The ground truth for these images are (from left to right): sand, grass, gravel, sand, pavement, sand (A); and grass, sand, pavement, pavement, pavement and pavement (B). (Yandun et al., 2018) © 2018 Elsevier.

All the experiments employed an on-board computer with a 2.20 Ghz Core i5 processor and 4 GB of RAM. With these characteristics, the processing time in average was 14.83 min per class for the training stage (with the extended dataset) and 0.51s per image in the labelling stage. Since training the algorithm can be done offline before operating in field, and considering that the labelling time is acceptable for vehicle moving at low speeds, the proposed approach is valid from the computational effort point of view. In addition, the memory required to store the learned model, as well as the texton dictionary is only 2 Mb, which would be important when employing low-performance computers with limited storage memory.

Finally, when comparing the proposed approach with previous works, various pros and cons were observed and they are summarized in Table 3.3.

TABLE 3.3: Comparison of the presented approach with others that employ different sensors and methodologies for terrain classification. (Yandun et al., 2018) © 2018 Elsevier.

	Approach			
	Proposed Time of Flight IR description	Radar/ Laser	Stereo Vision	Self Learning
Pros	Requires a small dataset to be robust in changing illumination conditions.	Various works provide an statistical traversability analysis.	Can also include slip prediction.	Do not need large training datasets.
	Reduced cost.	Large field of view.	Large field of view.	Are versatile when facing new terrains
	Overall accuracy higher than 85% using more than 15 000 images (more than 3.00 km of driving).	Robust in changing illumination conditions.	A geometric description of the terrain is available.	Some works provide a statistical traversability analysis
	A geometric description of the terrain can also be obtained.		Various terrains can be detected in the same image.	
Cons	Reduced field of view.	A finer classification in various terrain types can not be achieved.	Processing time is not suitable for online operation in some cases.	Rely on propioceptive information, which limits prediction capabilities.
	Only one label is obtained per image.	Cost is high for radar and 3D laser scanners.	Sensitive to changes in illumination.	Processing time is not suitable for online operation in some cases.
	Computation time needs requires improvement.	Lack of color or spectral information.	Overall accuracy up to 76.4% using 1500 images for testing.	

3.4 Contributions

The research work presented in this Chapter studied an image processing technique to classify five types of terrains. At difference with other related work in the same topic, using IR and color information yielded high accuracy rates (>80%) when testing outdoors in presence of changing illumination. Another point that makes this work particularly innovative is the use of a low cost sensor for data acquisition. The resulting system is intended to contribute to the traversability assessment of the surrounding terrain agricultural machinery for supervision and inspection. Furthermore, it can be used by a control system to obtain an efficient management of the vehicle resources.

The publications derived from the research work presented in this Chapter are:

- Yandun, F. et al., 2016. Classifying Agricultural Terrain for Machinery Traversability Purposes. In AGRICONTROL 2016: The 5th IFAC Conference on Sensing, Control and Automation for Agriculture. Elsevier, pp. 457–462.

- Yandun, F. et al., 2018. Terrain classification using ToF sensors for the enhancement of agricultural machinery traversability. Journal of Terramechanics, 76, pp.1–13.

- Prado, J. et al., 2018. Overcoming the Loss of Performance in Unmanned Ground Vehicles due to the Terrain Variability. IEEE Access, 3536(c), pp.1–17.

Chapter 4

MonteCarlo Methods Applied to System Identification of Nonzero Slipping Mobile Robots

As stated in Chapter 1, an integral perception system of a mobile robot navigating on off-road environments requires also a dynamic characterization of the robot movement. To complement the phenotyping and the descriptive applications described before, this Chapter describes a methodology to address such characterization with a particular point of view: parameters of nonzero slippage models are considered as random variables. In contrast with classic identification approaches in this matter, this assumption does not rely on assuming specific distributions (e.g., Gaussian). Further, it allows to obtain a probability measure of the estimations and subsequently propagate the uncertainty not only to the robot positioning, but also to the slippage-related variables.

As reviewed before, the terrain-wheel interaction and its effects on the robot movement are normally modelled using dynamic approaches. Levels of accuracy and reliability of the motion prediction/estimation depends of the model complexity. Having high fidelity models usually comes at expenses of an important computational load, as well as the requirement of more sensed information from the vehicle (e.g., torque, motor current, wheel sinkage). Kinematic approaches, on the other hand, are less accurate since they do not take into account the traction limits or inertial effects. However, with specific formulations (as the one described in this Chapter), the terra-mechanical effects of the terrain on the robot movement can be considered by predicting/modelling lateral and longitudinal slippage. Thus, in order to develop and test the proposed methodology for probabilistic system identification, a kinematic modelling was adopted. However, the theory and practical applications described in this Chapter can be extended for dynamical models to estimate parameters such as soil cohesion, sinkage moduli, sinkage exponent or angle of internal friction.

This Chapter is organized as follows: Section 4.1 introduces some basic concepts of probability and secuential monte carlo (SMC) methods, which are the basis of the formulation employed. Subsequently in Section 4.2, various identification strategies are described, highlighting their advantages and disadvantages. The kinematic model employed in this work is detailed in Section4.3. Special practical details about the implementation are described in Section 4.4. Finally, simulation and experimental results are presented in Section 4.6 and Section 4.7, respectively.

4.1 Markov Chains and Monte Carlo Methods

In probability theory, Markov Chains are models which can be used to describe various phenomena in nature and engineering processes (Golightly and Wilkinson, 2011; Marzband et al., 2017). Monte Carlo methods, on the other hand, provide a practical way to obtain numerical results in complex problems arisen when working with such applications (e.g., particle filters, condensation or survival of the fittest). Thus, combination of both comprise a practical solution for a number statistical inference problems. This Section describes the principal concepts of each one and its use together in the methodology called Particle Markov Chain Monte Carlo. For a thorough treatment of the ideas and concepts explained here, the reader is referred to (Robert and Casella, 2004; Andrieu et al., 2003; Doucet and Johansen, 2009; Sarkkä, 2013), and the references therein.

4.1.1 The Monte Carlo Approach

Monte Carlo methods are computational algorithms employed to solve integration and optimization problems, which are either intractable or complex mathematically. For example, consider the state space model (SSM):

$$\boldsymbol{x}_{t+1} = \mathsf{f}_t(\boldsymbol{x}_t, \boldsymbol{\omega}_t) \tag{4.1}$$

$$\boldsymbol{y}_t = \mathsf{g}_t(\boldsymbol{x}_t, \boldsymbol{v}_t) \tag{4.2}$$

where $\{\boldsymbol{x}_{t+1}\}_{t\geq 1} \in \mathbb{R}^n$ is a latent process only observable trough the measurement process $\{\boldsymbol{y}_t\}_{t\geq 1} \in \mathbb{R}^m$. Functions $\mathsf{f}_t(\cdot)$ and $\mathsf{g}_t(\cdot)$ are in general non linear and possible time varying equations modelling the state transition and measurement process, respectively. Additionally, the uncertainty in both models, $\boldsymbol{\omega}_t$ and $\boldsymbol{v}_t$, are considered as additive independent and identically distributed (i.i.d.) white sequences with known distributions.

A typical problem is to estimate the state at time t, given noisy measurements of the process. Considering that the state transition or the measurement model are not perfect and the state is markovian (see Section 4.1.2), the state and measurements can be stated as realizations of proper probability density functions (PDF) as follows:

$$\boldsymbol{x}_{t+1} \sim f(\boldsymbol{x}_{t+1}|\boldsymbol{x}_t, \boldsymbol{\gamma}) \tag{4.3}$$

$$\boldsymbol{y}_t \sim g(\boldsymbol{y}_t|\boldsymbol{x}_t, \boldsymbol{\gamma}) \tag{4.4}$$

with $\boldsymbol{x}_1 \sim \mu(\boldsymbol{x}_1)$. The probability density functions $f_t(\cdot)$ and $g_t(\cdot)$ encode the probability associated to the state and measurement transitions. Both functions may also depend on some values (possible unknown) of the parameter vector $\boldsymbol{\gamma}$.

When using linear and Gaussian state space and measurement models, an exact-optimal solution for the state estimation problem is the Kalman Filter (Sarkkä, 2013). However, in highly non-linear models with unknown distributions, obtaining analytic solutions is not typically possible. It is noteworthy that throughout this Chapter, the term filtering will be employed to refer the methodology to address an estimation problem. In a Bayesian setting, the generalized filtering problem can be addressed

by the recursive estimator given by equations 4.5 and 4.6:

$$p_{\boldsymbol{\gamma}}(\boldsymbol{x}_t|\boldsymbol{y}_{1:t}) = \frac{p_{\boldsymbol{\gamma}}(\boldsymbol{y}_t|\boldsymbol{x}_t)p_{\boldsymbol{\gamma}}(\boldsymbol{x}_t|\boldsymbol{y}_{1:t-1})}{p(\boldsymbol{y}_t|\boldsymbol{y}_{1:t-1})} \tag{4.5}$$

where $p_{\boldsymbol{\gamma}}(\boldsymbol{y}_t|\boldsymbol{x}_t)$ corresponds to the new information given by the measurements (*likelihood*). The term $p_{\boldsymbol{\gamma}}(\boldsymbol{x}_t|\boldsymbol{y}_{1:t-1})$ is the *posterior* distribution, described by Eq.4.6. The denominator $p(\boldsymbol{y}_t|\boldsymbol{y}_{1:t-1})$ is only a normalization constant, given it does not depend on the state. This step corresponds to the *measurement update* of the filter and it represents the estimations using the current measurements (a posteriori).

$$p_{\boldsymbol{\gamma}}(\boldsymbol{x}_{t+1}|\boldsymbol{y}_{1:t}) = \int p_{\boldsymbol{\gamma}}(\boldsymbol{x}_{t+1}|\boldsymbol{x}_t)p_{\boldsymbol{\gamma}}(\boldsymbol{x}_t|\boldsymbol{y}_{1:t})d\boldsymbol{x}_t \tag{4.6}$$

where $p_{\boldsymbol{\gamma}}(\boldsymbol{x}_t|\boldsymbol{y}_{1:t})$ is the *prior* information given by Eq. 4.5, and $p_{\boldsymbol{\gamma}}(\boldsymbol{x}_{t+1}|\boldsymbol{x}_t)$ is the posterior distribution defined by the state transition model. This step is known as *time update* and represents the current state calculated in base of the past estimate given by Eq. 4.5. To avoid cluttered notation, in both measurement and time update expressions, the (possible) dependency of the distributions on the parameter vector $\boldsymbol{\gamma}$ is indicated as an underscore. Furthermore, the dependence of these functions to control inputs, is omitted for the same reason, but it can be straightforwardly included, if necessary.

Computing Eq. 4.6 involves integrating on a high dimensional space, which can also have a complicated functional form. In these situations, Monte Carlo methods can be used to draw samples from Eq. 4.6 by generating samples from the underlying random variable $\boldsymbol{x}_t|\boldsymbol{x}_{t-1}$ and calculating a sample average.

As can be noted in this example, the *time update* equation correspond to calculate an expectation over the posterior distribution (Eq. 4.5). More generally, consider a random variable $\boldsymbol{x}$ distributed according to the pdf $\xi(\boldsymbol{x})$ (known as target density), which is defined in some space X . The problem addressed by Monte Carlo methods is the calculation of the expected value

$$\mathbb{E}[\zeta(\boldsymbol{x})] = \int \zeta(\boldsymbol{x})\xi(\boldsymbol{x})d\boldsymbol{x} \tag{4.7}$$

for some particular function $\zeta(\boldsymbol{x})$. If one can get N i.i.d. samples $\{\boldsymbol{x}^{(i)}\}_{i=1}^{N}$ from $\xi(\boldsymbol{x})$, it is possible to define an empirical approximation of the target distribution

$$\xi(\boldsymbol{x}) \approx \frac{1}{N}\sum_{i=1}^{N}\delta(\boldsymbol{x} - \boldsymbol{x}^{(i)}) \tag{4.8}$$

where $\delta(\boldsymbol{x} - \boldsymbol{x}^{(i)})$ denotes a Dirac Delta function with point mass located at $\boldsymbol{x}^{(i)}$. Plugging this expression in Eq. 4.7 results in

$$\int \zeta(\boldsymbol{x}\xi(\boldsymbol{x})d\boldsymbol{x} \approx \int \zeta(\boldsymbol{x})\frac{1}{N}\sum_{i=1}^{N}\delta(\boldsymbol{x} - \boldsymbol{x}^{(i)}) = \frac{1}{N}\sum_{i=1}^{N}\zeta(\boldsymbol{x}^{(i)}) \tag{4.9}$$

which is a Monte Carlo estimator of Eq. 4.7. Among its diverse statistical properties,

three are the most important: i) it is unbiased, ii) it has finite variance, and iii) the law of the large numbers guarantee almost sure (a.s.) convergence when $N \to \infty$ (Graham and Talay, 2013).

It is noteworthy that the assumption of feasibility to get samples from the target distribution is strong. Generally this distribution is not available or known, which in fact is an issue to address. However, sampling from unknown or complex distributions is the objective of the techniques discussed in the following. Basic techniques including rejection and importance sampling are first detailed, since they can be used along with more sophisticated methods such as Markov Chain Monte Carlo (MCMC).

Rejection Sampling

This sampling technique is useful when the target distribution $\xi(\boldsymbol{x})$ is known up to a proportionality constant (i.e., $\xi(\boldsymbol{x}) = \tilde{\xi}(\boldsymbol{x})/\kappa$). This is a typical problem found in Bayesian estimation problems, as the one formulated in Eq. 4.5. Exact draws from the target distribution can be obtained by using an accept/reject procedure applied to samples generated by a (known) proposal distribution $\bar{\boldsymbol{x}} \sim q(\boldsymbol{x})$, satisfying $\tilde{\xi}(\boldsymbol{x}) \leq q(\boldsymbol{x})Z$, with $Z < \infty$.

Briefly, consider a variable sampled from an uniform in the unit interval $u \sim \mathcal{U}_{[0,1]}$, a new draw from the proposal $\bar{\boldsymbol{x}}$ is accepted if $Zq(\boldsymbol{x})u \leq \tilde{\xi}(\boldsymbol{x})$. Otherwise $\bar{\boldsymbol{x}}$ is rejected and the procedure is repeated until N samples are generated. The overall method summarized in Algorithm 1 guarantees to generate i.i.d. samples from $\xi(\boldsymbol{x})$ (Robert and Casella, 2004). Furthermore, a graphic interpretation of the methodology for rejection sampling is also depicted in Fig. 4.1.

Algorithm 1 Rejection Sampling

Initialize:
    Set $k = 1$
while $k < N$ **do**
    Sample $\bar{\boldsymbol{x}} \sim q(\boldsymbol{x})$
    Sample $u \sim U_{[0,1]}$
    if $u \leq \frac{\tilde{\xi}(\bar{\boldsymbol{x}})}{q(\bar{\boldsymbol{x}})Z}$ **then**
        Accept $\bar{\boldsymbol{x}}$
        $k = k + 1$
    else
        Reject $\bar{\boldsymbol{x}}$
    end if
end while

This sampling technique is useful in some situations, but is limited in many others. The most complicated requirement to fill is to find a bound Z for which $\tilde{\xi}(\boldsymbol{x}) \leq q(\boldsymbol{x})Z$ for all the possible values of $\boldsymbol{x}$. This issue is specially tough in state spaces with large dimensionality. Furthermore, if Z is chosen too big, the acceptance probability decays severely, resulting in large iterations (the sampler stays long time in the while loop in Algorithm1) required to generate N samples.

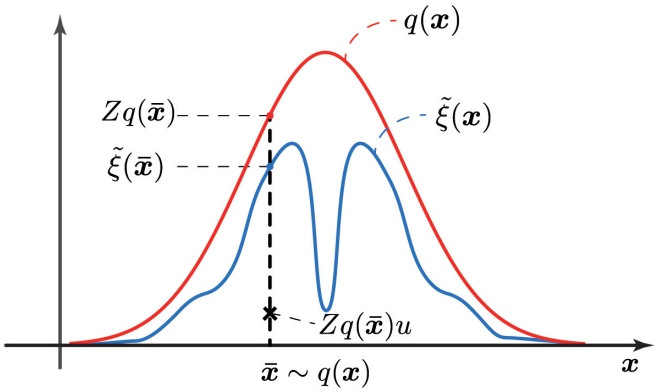

FIGURE 4.1: Graphical representation of rejection sampling. A new sample $\bar{\boldsymbol{x}}$ is generated independently and uniformly over $q(\boldsymbol{x})Z$ (all the area under the red curve). If $\bar{\boldsymbol{x}}$ turns to be also below the blue curve, the sample is accepted to be a drawn from $\xi(\boldsymbol{x})$, otherwise it is rejected. In the case depicted here, $\bar{\boldsymbol{x}}$ is indeed an accepted sample.

Importance Sampling

Similarly to rejection sampling, this method also allows to sample from unknown target distributions $\xi(\boldsymbol{x})$ using known proposals $q(\boldsymbol{x})$. However, instead of rejecting certain samples, all of them are accepted, but weighted according to their fitting with the target distribution. This formulation allows to solve complex integration problems of the form given by Eq. 4.7. As mentioned in the previous method, in Bayesian estimation and learning it is common to work with target distributions known up to proportionality. Then, Eq. 4.7 can be rewritten,

$$\mathbb{E}[\zeta(\boldsymbol{x})] = \int \zeta(\boldsymbol{x}) \frac{\tilde{\xi}(\boldsymbol{x})}{\kappa q(\boldsymbol{x})} q(\boldsymbol{x}) d\boldsymbol{x} = \frac{1}{\kappa} \int \zeta(\boldsymbol{x}) W(\boldsymbol{x}) q(\boldsymbol{x}) d\boldsymbol{x} = \mathbb{E}[\zeta(\boldsymbol{x}) W(\boldsymbol{x})] \quad (4.10)$$

where $W(\boldsymbol{x}) = \frac{\tilde{\xi}(\boldsymbol{x})}{\kappa q(\boldsymbol{x})}$. Then, a Monte Carlo estimator can be used to approximate this integral by sampling from the known proposal

$$\mathbb{E}[\zeta(\boldsymbol{x}) W(\boldsymbol{x})] \approx \frac{1}{NK} \sum_{i=1}^{N} \zeta(\boldsymbol{x}^{(i)}) W(\boldsymbol{x}^{(i)}) \quad (4.11)$$

where the only unknown term is the normalization constant κ. It can be approximated using the samples from the proposal in a MC estimator, as follows

$$1 = \int \frac{\tilde{\xi}(\boldsymbol{x})}{K} d\boldsymbol{x} \quad (4.12)$$

$$K = \int \frac{\tilde{\xi}(\boldsymbol{x})}{q(\boldsymbol{x})} q(\boldsymbol{x}) d\boldsymbol{x} \approx \frac{1}{N} \sum_{i=1}^{N} \frac{\tilde{\xi}(\boldsymbol{x}^{(i)})}{q(\boldsymbol{x}^{(i)})} = \frac{1}{N} \sum_{i=1}^{N} W(\boldsymbol{x}^{(i)}) \quad (4.13)$$

Then, the final importance sampling estimator of integral 4.7, is given by

$$\mathbb{E}[\zeta(\boldsymbol{x})] \approx \sum_{i=1}^{N} \zeta(\boldsymbol{x}^{(i)}) w^{(i)} \tag{4.14}$$

with $w^{(i)} = \frac{W(\boldsymbol{x}^{(i)})}{\sum_{s=1}^{N} W(\boldsymbol{x}^{(s)})}$.

Since this formulation is based on Monte Carlo methods, importance sampling (IS) also has the same statistical properties of MC samplers, namely: it is unbiased, it has finite variance and (a.s.) convergence (Andrieu et al., 2003). A further mathematical treatment of importance sampling can allow to choose specific proposals which produce very efficient results in terms of variance (Casella and Robert, 1994).

4.1.2 Particle Filters and Markov Chain Monte Carlo

State inference and learning of dynamical systems of the form presented in Eq. 4.3 are two problems related by a common aspect: both require to estimate the system state. For example, for a parametrized model, it is first necessary to draw information about the state to subsequently learn or identify any possible unknown parameters. In the bayesian setting adopted in this Chapter, there are two methodologies of interest: filtering and smoothing. The filtering approach aims to estimate the current state based on a history of measurements using the recursive estimator depicted in equations 4.5 and 4.6. As a result, the filtering density $p(\boldsymbol{x}_t|\boldsymbol{y}_{1:t})$ is determined or approximated, in general. State smoothing, on the other hand, aims to use all the information available to get refined estimations for an entire state trajectory. Thus, the joint smoothing density (JSD) $p(\boldsymbol{x}_{1:T}|\boldsymbol{y}_{1:T})$ is determined or approximated up to some time T.

As stated before, in linear gaussian models, the Kalman Filter is the optimal solution for filtering and smoothing. In other applications with nonlinear models, it is possible to use sub-optimal approaches based on linearisation, data transformation or special integration methods (e.g., Extended or Unscented Kalman Filters, spherical cubature integration) (Sarkkä, 2013). Nevertheless, in this thesis, a more general framework is studied, where non-linear and possibly non-gaussian systems can be approximated using sampling methods including particle filters and Markov chain Monte Carlo.

This perspective is valid from the robotics point of view applied here since motion models with non-zero slippage are non-linear and not always the underlying distributions can be considered Gaussian. For example, when a robot is traversing an environment with similar characteristics. It has to maintain high probability hypothesis (e.g., about its localization) on all the possible positions until some feature provides a *strong* likelihood to choose one of them. In this case, the prior on the robot positioning is clearly multi modal. Regarding wheel slip models, they may include complex expressions from which it is usually difficult to get reliable approximations, specially for complex terrains. Although not dynamical models are used here, the proposed work is aimed to be further developed for handling them.

Particle Filter

Rejection and important sampling are important methods to get draws from unknown distributions. However, they alone are not applicable in state inference problems since the dimensionality of the random variables involved increases considerably over time. In contrast, they are suitable when used in recursive estimators to approximate posterior distributions at each time step. Concretely, the particle filter is an sequential application of importance resampling for the bayesian estimator given by equations 4.5 and 4.6. The name of the filter comes from the fact that the posterior filtering distribution is approximated using IS, generating a set of weighted samples $\left\{\boldsymbol{x}_t^{(i)}\right\}_{i=1}^{N}$ also called particles.

In order to derive the algorithm of the particle filter, it is first necessary to highlight another interpretation of importance sampling: it also defines a weighted point-mass approximation of the target distribution

$$\xi(\boldsymbol{x}) \approx \hat{\xi}(\boldsymbol{x}) = \sum_{i=1}^{N} w^{(i)} \delta(\boldsymbol{x} - \boldsymbol{x}^{(i)}) \tag{4.15}$$

This outcome allows to formulate the filter in an inductive way. To avoid cumbersome notation, (possible) dependency on the parameter vector is not denoted, and assumed implicit. Consider that at time $t-1$ an IS approximation of the *posterior* pdf is available

$$\hat{p}(\boldsymbol{x}_{t-1}|\boldsymbol{y}_{1:t-1}) = \sum_{i=1}^{N} w_{t-1}^{i} \delta(\boldsymbol{x}_{t-1} - \boldsymbol{x}_{t-1}^{i}) \tag{4.16}$$

Then, time update equation can be re-written

$$\begin{aligned} p(\boldsymbol{x}_t|\boldsymbol{y}_{1:t-1}) &= \int f(\boldsymbol{x}_t|\boldsymbol{x}_{t-1}) p(\boldsymbol{x}_{t-1}|\boldsymbol{y}_{1:t-1}) d\boldsymbol{x}_{t-1} \\ &= \int f(\boldsymbol{x}_t|\boldsymbol{x}_{t-1}) \sum_{i=1}^{N} w_{t-1}^{(i)} \delta(\boldsymbol{x}_{t-1} - \boldsymbol{x}_{t-1}^{(i)}) d\boldsymbol{x}_{t-1} \\ &= \sum_{i=1}^{N} w_{t-1}^{(i)} \int f(\boldsymbol{x}_t|\boldsymbol{x}_{t-1}) \delta(\boldsymbol{x}_{t-1} - \boldsymbol{x}_{t-1}^{(i)}) d\boldsymbol{x}_{t-1} \\ &= \sum_{i=1}^{N} w_{t-1}^{(i)} f(\boldsymbol{x}_t|\boldsymbol{x}_{t-1}^{(i)}) \end{aligned} \tag{4.17}$$

With this result, the posterior distribution at time t can be obtained

$$p(\boldsymbol{x}_t|\boldsymbol{y}_{1:t}) \approx \frac{g(\boldsymbol{y}_t|\boldsymbol{x}_t)}{p(\boldsymbol{y}_t|\boldsymbol{y}_{1:t-1})} \sum_{i=1}^{N} w_{t-1}^{(i)} f(\boldsymbol{x}_t|\boldsymbol{x}_{t-1}^{(i)}) \tag{4.18}$$

Likewise, this posterior can also be approximated using importance sampling

$$p(\boldsymbol{x}_t|\boldsymbol{y}_{1:t}) \approx \sum_{i=1}^{N} w_t^{(i)} \delta(\boldsymbol{x}_t - \boldsymbol{x}_t^{(i)}) \quad \text{where} \quad w_t^{(i)} = \frac{\tilde{p}(\boldsymbol{x}_t^{(i)}|\boldsymbol{y}_{1:t})}{q(\boldsymbol{x}_t}) \tag{4.19}$$

where $p(\boldsymbol{x}_t^{(i)}|\boldsymbol{y}_{1:t}) = \frac{\tilde{p}(\boldsymbol{x}_t^{(i)}|\boldsymbol{y}_{1:t})}{p(\boldsymbol{y}_t|\boldsymbol{y}_{1:t-1})}$. Furthermore, as the proposal distribution is a design parameter, it can be defined as follows

$$q(\boldsymbol{x}_t) \triangleq \sum_{i=1}^{N} v_{t-1}^{(i)} r(\boldsymbol{x}_t|\boldsymbol{x}_{t-1}^{(i)}, \boldsymbol{y}_t) \tag{4.20}$$

This notation encodes the procedure to sample from the known distribution $r(\cdot)$, explained as follows. The probability to get the i^{th} particle at time t based on some ancestor j at time $t-1$ is given by $v_{t-1}^{(i)}$. Thus, one can define the concept of *ancestor index* $a_t^{(i)}$, which is the index of the particle on which r was conditioned to generate a new sample. Summarizing,

$$\mathbb{P}(a_t^{(i)} = j) = v_{t-1}^{(i)} \qquad j = 1, 2, \ldots, N \tag{4.21}$$

$$\boldsymbol{x}_t^{(i)} \sim r(\boldsymbol{x}_t|\bar{\boldsymbol{x}}_{t-1}^{(i)}, \boldsymbol{y}_t) \tag{4.22}$$

where the particle $\bar{\boldsymbol{x}}_{t-1}^{(i)} = \boldsymbol{x}_{t-1}^{a_t^{(i)}}$ is the *ancestor* of the particle $\boldsymbol{x}_t^{(i)}$ since the last is sampled conditionally on the first. At contrary to classic particle filter derivations, this procedure allows to get samples from a known proposal introducing implicitly the concept of *resampling*. This is, the process of random selection (with replacement) of $\left\{\boldsymbol{x}_{t-1}^{(i)}\right\}_{i=1}^{N}$ to generate $\left\{\bar{\boldsymbol{x}}_{t-1}^{(i)}\right\}_{i=1}^{N}$, based on certain weights.

To illustrate the idea so far and the *ancestor index* concept, consider a five particle set at time t, $\left\{\boldsymbol{x}_t^{(i)}\right\}_{i=1}^{5}$. If the resampling output at time $t-1$ is x_{t-1}^1, x_{t-1}^3, x_{t-1}^3, x_{t-1}^2, x_{t-1}^3, then, the ancestors indices for the new particles are

$$\left\{a_t^i\right\}_{i=1}^{N} = \left\{a_t^1, a_t^2, a_t^3, a_t^4, a_t^5\right\} \tag{4.23}$$

$$= \{1, 3, 3, 2, 3\} \tag{4.24}$$

The next step in the filter derivation consists in inserting Eq. 4.19 in Eq. 4.18 to get the weights of the new particles at time t

$$\bar{w}_t^{(i)} = \frac{g(\boldsymbol{y}_t|\boldsymbol{x}_t^{(i)}) \sum_{j=1}^{N} w_{t-1}^j f(\boldsymbol{x}_t^{(i)}|\boldsymbol{x}_{t-1}^{(j)})}{\sum_{j=1}^{N} v_{t-1}^j r(\boldsymbol{x}_t^{(i)}|\boldsymbol{x}_{t-1}^{(j)}, \boldsymbol{y}_t)} \tag{4.25}$$

Finally, at the initial time $t = 1$, the posterior $p(\boldsymbol{x}_1|\boldsymbol{y}_1)$ can be approximated using IS and a proposal $q(\boldsymbol{x}_1)$. The weight function in this case produce weights given by $w_1^i \propto g(\boldsymbol{y}_1|\boldsymbol{x}_1^{(i)})p(\boldsymbol{x}_1^{(i)})/q(\boldsymbol{x}_1)$. To this IS approximation to be a pdf, the weights must be normalized, as in Eq. 4.14. This completes the filter derivation since it iteratively alternates between time and measurement updates when new information arrives.

The freedom to design of the proposal density allows to produce algorithms with different statistical properties that make complete use of all information available. However, in the work developed here, the basic solution is adopted, which uses as

proposal $q(\boldsymbol{x}_t) = \sum_{j=1}^{N} w_{t-1}^{(j)} f(\boldsymbol{x}_t^{(i)}|\boldsymbol{x}_{t-1}^{(j)})$, thus obtaining a weighting function

$$\bar{w}_t^{(i)} = g(\boldsymbol{y}_t|\boldsymbol{x}_t^{(i)}) \tag{4.26}$$

which are unnormalized weights, depending only on the likelihood of the observation. To get a proper pdf approximation, it is necessary to normalize the weights, as done before. This particular choice of the proposal yields a *bootstrap particle filter*, whose implementation is summarized in Algorithm 2.

Algorithm 2 Bootstrap Particle Filter

1: **Initialize:**
   Sample $\boldsymbol{x}_1^{(i)} \sim \mu(\boldsymbol{x}_1)$
   Calculate weights $\bar{w}_1^{(i)} = g(\boldsymbol{y}_1|\boldsymbol{x}_1^{(i)})$
   Normalize: $w_1^{(i)} = \bar{w}_1^{(i)} / \sum_{j=1}^{N} \bar{w}_1^{(j)}$
2: **for** $t = 2$ **to** T **do**
3: Resampling: Sample $a_t^{(i)}$ with $\mathbb{P}(a_t^{(i)} = j) = w_{t-1}^{(j)}$
4: Time Update: Sample $\boldsymbol{x}_t^i \sim f(\boldsymbol{x}_t|\bar{\boldsymbol{x}}_{t-1}^{(i)})$
5: Measurement Update: Calculate weights $\bar{w}_t^{(i)} = g(\boldsymbol{y}_t|\boldsymbol{x}_t^{(i)})$
6: Normalize: $w_t^i = \bar{w}_t^{(i)} / \sum_{j=1}^{N} \bar{w}_t^{(j)}$
7: **end for**

While the formulation presented here is not classical, it allows to introduce the concept of *ancestor index*. It will be employed subsequently in the identification algorithm to get samples from the JSD. Keeping trace of the state lineage through its ancestors is helpful to mitigate the path degeneracy problem, resulting of the resampling process. This is, at some time the variety of particles would decay due to the survival of the fittest effect (Doucet and Johansen, 2009).

Markov Chain Monte Carlo

A Markov chain (MC) is a random process (i.e., a sequence of random variables) whose transition probability is only function of the current state of the chain (see Fig. 4.2). In other words, the next state of the chain depends only on its current value. The word *state* is used indistinctly in this work for either, Markov chains and state space models; however, it is not a general case. State space models of the form described by Eq. 4.3 model a physical process or system evolving over time, forming a MC. A Markov chain, on the other hand, is a broader concept with other possible interpretations. Furthermore, in this work the index k will be used to denote a transition within a chain, whereas the index t denotes a transition in time for a state space model. For certain cases they may be equal, but not in the general setting discussed in this Section. Extensive theory and properties of MC have been developed in the literature, but only the most important concepts in the context of state inference and system identification are discussed here.

Markov Chain Monte Carlo (MCMC) includes a variety of strategies to generate samples from target distributions, exploring the state space using Markov processes. The idea is to construct a chain whose *limiting distribution* is given by the target

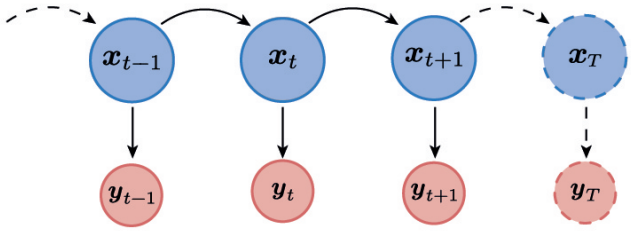

FIGURE 4.2: Graphical representation of a state space model. A Markov chain represents the state evolution in time since the current value only depends of its predecessor. The system states for each time $\boldsymbol{x}_t$ are often latent or hidden variables to be estimated through measurements $\boldsymbol{y}_t$.

distribution. The concept of *limiting distribution* requires a stability property characteristic of the chains used in MCMC: the existence of a *stationary distribution*. Briefly, if ρ is stationary, $\boldsymbol{x}[k]$ and $\boldsymbol{x}[k+1]$ are marginally distributed according to ρ (this includes all $\boldsymbol{x}[m] \forall m \geq k$). In complement, a limiting distribution results of the convergence (in distribution, under the total variation norm) of the marginals to the stationary distribution, independently of the initial conditions. This implies that a limiting distribution is stationary, but the opposite does not necessarily hold. The practical applicability of MCMC requires both, the stationary and limiting distributions to be equal. This equality in a given MC is guaranteed by two properties: irreductibility and aperiodicty. To get a formal proof of this statement, as well as a deeper theoretical insight see e.g., Tierney, 1994.

Within the MCMC algorithms, there are two of interest for this work: Metropolis-Hastings and Gibbs samplers. The Metropolis-Hastings (MH) (Metropolis et al., 1953; Hastings, 1970) algorithm basically consists in using an accept/reject scheme to construct a chain whose limiting distribution is equal to the target distribution $\xi(\boldsymbol{x})$. To this aim, at each iteration, a candidate sample $\boldsymbol{x}'$ from some arbitrary proposal $q(\boldsymbol{x}'|\boldsymbol{x})$ has to be first generated. Then, the Markov chain moves from the current state to the candidate with an acceptance probability given by

$$A(\boldsymbol{x}'|\boldsymbol{x}) = min\left\{1, \frac{\xi(\boldsymbol{x}')}{\xi(\boldsymbol{x})}\frac{q(\boldsymbol{x}|\boldsymbol{x}')}{q(\boldsymbol{x}'|\boldsymbol{x})}\right\} \tag{4.27}$$

Thus, if the chain is in the state $\boldsymbol{x}[k-1]$, and the candidate is accepted wit probability $A(\boldsymbol{x}'|\boldsymbol{x})$, the chain moves towards $\boldsymbol{x}'$. This is, the acceptance of a new sample implies that $\boldsymbol{x}[k] = \boldsymbol{x}'$, whereas the rejection produces $\boldsymbol{x}[k] = \boldsymbol{x}[k-1]$. Algorithm 3 summarizes the MH methodology, providing a practical implementation receipt to generate M samples.

It is interesting to note that the acceptance probability involves a division of the target densities. This implies that one can use the MH sampler using only *unnormalized* targets (i.e., known up to proportionality) and the resulting samples are still draws from the target density. Further details about convergence and theoretical insights, the reader is referred to (Brooks et al., 2011), and the references therein.

The other method of MCMC sampling of interest for this work is Gibbs sampling.

Algorithm 3 Metropolis-Hastings Sampling

Initialize:
  Set the initial state $\boldsymbol{x}[1]$
for $k = 2$ **to** M **do**
  Sample $u \sim U_{[0,1]}$
  Sample $\boldsymbol{x'} \sim q(\boldsymbol{x'}|\boldsymbol{x}[k-1])$
  Calculate the acceptance probability $A(\boldsymbol{x'}|\boldsymbol{x})$
  if $u \leq A$ **then**
    $\boldsymbol{x}[k] = \boldsymbol{x'}$
  else
    $\boldsymbol{x}[k] = \boldsymbol{x}[k-1]$
  end if
end for

It can be considered a special case of the MH method, with a specific choice of the proposal distribution that produce $A(\boldsymbol{x'}|\boldsymbol{x}) = 1$ (Andrieu et al., 2003). This outcome implies that all samples are accepted. To apply this algorithm, the underlying random variable has to be a n-dimensional vector $\boldsymbol{x} = \{x_1, x_2, x_3, \ldots, x_n\}$, with expressions for the conditionals $p(x_i|x_1, x_2, x_{i-1}, x_{i+1}, \ldots, x_n)$ known for all i. Then, the Markov chain with limiting distribution $\xi(\boldsymbol{x})$ is constructed by sampling alternatively from those conditionals. This scheme constitutes a basic Gibbs sampler, which is summarized in Algorithm 4.

Algorithm 4 Basic Gibbs Sampling

Initialize:
  Set the initial state $\boldsymbol{x}[1]$
for $k = 2$ **to** M **do**
  Sample $x_1[k] \sim p(x_1|x_2[k-1], x_i[k-1], x_{i+1}[k-1], \ldots, x_n[k-1])$
  Sample $x_2[k] \sim p(x_2|x_1[k], x_i[k-1], x_{i+1}[k-1], \ldots, x_n[k-1])$
  Sample $x_3[k] \sim p(x_3|x_1[k], x_2[k], x_i[k-1], x_{i+1}[k-1], \ldots, x_n[k-1])$
  $\vdots$
  Sample $x_i[k] \sim p(x_i|x_1[k], x_2[k], x_{i-1}[k], x_{i+1}[k-1], \ldots, x_n[k-1])$
end for

If the conditionals are not available in closed form, intermediate MH samplers can be used to approximate them. This variant, also produces a chain whose limiting distribution is the target (Brooks et al., 2011). The basic form of the Gibbs sampler is often impractical, specially when the individual components of $\boldsymbol{x}$ are highly dependent on each other. This effect is called *poor mixing*, which makes that sampling from the conditionals gives insufficient updates since few new information is contributed by each one. Thus, the chain does not fully explores the state space, possibly getting stuck in some region. To alleviate this issue, strategies called *grouping* and *collapsing* provide formulations to reparametrize the conditionals in a way that the limiting distribution remains unchanged.

All of the sampling algorithms described so far will be employed as part of the identification approach described in the following Section. While only the basic

frameworks are presented they provide a way to understand the formulation to generate samples from the posterior parameter distribution. Any important variation of these sampling techniques will be subsequently addressed.

4.2 Probabilistic Identification Approaches

As stated in Section 4.1.1, the transition functions for the state and measurements may depend on some parameter $\boldsymbol{\gamma}$. This parametric formulation is useful in a number of applications since it gives the model adaptability to different circumstances by simply varying the values of $\boldsymbol{\gamma}$. For example, in the scope of this thesis, parameters of non-zero slip models for a mobile robot would change depending of the terrain. This parameters are often unknown and have to be learned while the robot is moving. Since the system state (i.e., the robot movement variables) is not deterministically known, the model can not be easily identified, requiring an intermediate state inference strategy. Thus, state estimation and parameter learning are tightly coupled, even in a identification problem. Furthermore, as the state is considered as a random variable, the proper way to proceed is to consider the parameters also as random variables, with a posterior distribution to be estimated.

In general, to address the system learning, there are various approaches in the literature. Table 4.1 provides a summary of the main methods grouped according to their identification methodology: marginalization and data augmentation. Additionally, advantages and disadvantages of each one are also depicted. In short, the marginalization strategy aims to identify the system by taking the states out of the problem by integrating them out. Thus, the parameters $\boldsymbol{\gamma}$ are the only variables of interest. The data augmentation strategy, on the other hand, provides a framework to explicitly couple the state inference and learning problems. The idea is to first infer information about the system state and subsequently use that knowledge to infer information about the parameters. Further information of each one can be found in (Södeström and Stoica, 1989; Lindsten, 2013; Schön et al., 2015).

In this work, the Bayesian approach within data augmentation is employed. As shown in Table 4.1, the advantages with respect to the other methods are considerable, despite of the apparent complexity involved in the implementation. Moreover, the characteristics of the model employed, as well as the capability to obtain samples not only from the parameters, but also the slipping velocities makes this approach suitable for the proposed objectives. As will be shown later, the practical applicability of this method requires the use of all the sampling strategies described so far and variants of some of them.

Data Augmentation - Bayesian Learning

Consider the general state space model described in Eq. 4.3. The classic Bayesian identification aims to determine or approximate the parameter posterior

$$p(\boldsymbol{\gamma}|\boldsymbol{y}_{1:T}) = \frac{p(\boldsymbol{\gamma}|\boldsymbol{y}_{1:T})p(\boldsymbol{\gamma})}{p(\boldsymbol{y}_{1:T})} \tag{4.28}$$

TABLE 4.1: Classification and comparison of probabilistic identification approaches.

	Marginalization		Data Augmentation	
Maximum likelihood	Direct Optimization		Expectation Maximization	
	Pros	Cons	Pros	Cons
	- For certain models it can produce exact solutions. - It does not require any other analytical treatment more than solving an optimization problem.	- It requires a closed form of the likelihood to get exact solutions. - If the likelihood is not available in closed form, the use of gradient-based methods is required to get approximate solutions. - This method only produce punctual estimates. - Since the state is integrated out, all the information of the state space model is no fully employed.	- The system state is also estimated alongside the parameters. - It involves an optimization problem. - It can be efficiently addressed using the MCMC samplers described previously.	- This method only produce punctual estimates, as consequence any other information about the posterior can not obtained. - For non linear models, approximations of the distributions involved may cause a sub-optimal solutions when employing gradient-based methods in the optimization (Sarkkä, 2013).
Bayesian	Metropolis-Hastings Sampling		Gibbs Sampling	
	Pros	Cons	Pros	Cons
	- The posterior distribution of the parameters can be approximated using MC samplers. - Any additional knowledge about the parameters can be included using a prior distribution. - For certain models, the use of conjugate priors produce simpler computations (Yang, Drive, and Berger, 1998; Kroese, Taimre, and Botev, 2011).	- Since the state is integrated out, all the information of the state space model is no fully employed. - The proposal distribution of the MH sampler must be carefully designed, otherwise the rejection rate may be high.	- The posterior distribution of the parameters can be approximated. - Samples of the posterior distribution of the state and intermediate variables (e.g., wheel slip velocities) can also be obtained. - Any additional knowledge about the parameters can be included using a prior distribution. - For certain models, the use of conjugate priors produce simpler computations (Yang, Drive, and Berger, 1998; Kroese, Taimre, and Botev, 2011). - It can be efficiently addressed using the MCMC samplers described previously. - Additional sampling techniques that not affect the convergence can be employed within this method.	- It is required to sample from two conditional distributions. If they are not known, additional MCMC samplers have to be used. - If other samplers are used within this method, additional tuning of parameters is required.

using all the available information from a batch of sensor measurements $\boldsymbol{y}_{1:T}$ and (possibly) input commands $\boldsymbol{u}_{1:T}$. However, in plenty of non-linear models, even when the prior is chosen to be well designed, the likelihood is difficult to compute. Furthermore, the dependence of the states in this approach is not considered (states are marginalized). As an alternative, a data augmentation methodology is introduced. The aim is to determine or approximate the joint state-parameter posterior

$$p(\boldsymbol{\gamma}, \boldsymbol{x}_{1:T}|\boldsymbol{y}_{1:T}) = p(\boldsymbol{x}_{1:T}|\boldsymbol{y}_{1:T}, \boldsymbol{\gamma})p(\boldsymbol{y}_{1:T}|\boldsymbol{\gamma}) \tag{4.29}$$

Thus, the identification problem can be solved by considering the state sequence as an auxiliary (latent) variable which is estimated alongside the parameters. The posterior density of the parameters is then obtained by marginalization of Eq. 4.29.

The presence of a latent variable suggest an expectation maximization (EM) approach (Dempster, Larid, and Rubin, 1977; Nordh et al., 2015); however, this algorithm only provides punctual estimation of the parameters, with little information about the posterior distribution. In contrast, a Gibbs sampler can be used to get draws from the exact posterior 4.29, by alternatively sampling from its conditionals. The joint state-parameter posterior can be then approximated by initializing $\boldsymbol{\gamma}[0] \in \Gamma$ and iterating for $k \geq 0$:

$$\text{Draw} \quad \boldsymbol{x}^*_{1:T}[k] \sim p(\boldsymbol{x}_{1:T}|\boldsymbol{y}_{1:T}, \boldsymbol{\gamma}[k]) \tag{4.30a}$$

$$\text{Draw} \quad \boldsymbol{\gamma}[k+1] \sim p(\boldsymbol{\gamma}|\boldsymbol{x}^*_{1:T}[k], \boldsymbol{y}_{1:T}) \tag{4.30b}$$

Under weak conditions, this procedure will generate a valid irreductible and aperiodic Markov Chain in the parameters and states $\{\boldsymbol{\gamma}[k], \boldsymbol{x}_{1:T}\}_{k\geq 1}$, with limiting distribution $p(\boldsymbol{\gamma}, \boldsymbol{x}_{1_T}|\boldsymbol{y}_{1:T})$ (Lindsten and Schön, 2013). Finally, the parameter posterior is the marginal distribution $p(\boldsymbol{\gamma}|\boldsymbol{y}_{1:T})$ that is obtained just keeping the samples corresponding to the parameters.

The first step in this sampling scheme consists in drawing a state trajectory $\boldsymbol{x}_{1:T}$ from the joint smoothing density (JSD) $p(\boldsymbol{x}_{1:T}|\boldsymbol{y}_{1:T}, \boldsymbol{\gamma})$. At this point, it is required to solve a smoothing problem (to sample an entire state trajectory) mainly for two reasons: poor mixing and path degeneracy. Poor mixing, refers to the problem that states are often strongly correlated in consecutive time steps, thus producing a slow convergence (Kroese, Taimre, and Botev, 2011). Path degeneracy, as explained in Section 4.1.2, is an issue inherent to the resampling stage of sequential importance samplers (e.g., the particle filter). Furthermore, using a particle filter to approximate the JSD does not make $p(\boldsymbol{\gamma}, \boldsymbol{x}_{1_T}|\boldsymbol{y}_{1:T})$ a limiting distribution of the chain (Andrieu, Doucet, and Holenstein, 2010). Thus, to address this step in the proposed Gibbs sampler, one of the diverse smoothing algorithms available in the literature can be used. However, since slip models are highly non-linear in general, a Monte Carlo Markov Chain method is employed. Within MCMC exist a variety of algorithms to this aim, namely forward filter/backward smoother, forward filter/backward simulator, Metropolis-Hastings forward filtering/backward proposing, among others. However, these techniques are inefficient in general, since they require a large amount of simulations just to sample one state trajectory. Furthermore, large amount of samples are required to get accurate approximations of the JSD (Lindsten and Schön, 2013).

As an alternative, methods that combine the strengths of Sequential Monte Carlo (SMC) estimation and MCMC have been proposed. They provide a systematic way

to efficiently sample the state space by using SMC to design appropriate proposal distributions for MCMC algorithms (Andrieu, Doucet, and Holenstein, 2010). The general framework to theoretically design and implement this approach is called Particle Markov Chain Monte Carlo (PMCMC).

In this thesis, the methodology witihin PMCMC named conditional particle filter with ancestor sampling (CPF-AS) is employed to get samples from the JSD. It is based in the conditional particle filter approach originally proposed by Andrieu, Doucet, and Holenstein, 2010. This early work consisted in providing beforehand one particle trajectory $\boldsymbol{x'}_{1:T}$ with a given lineage or ancestor path $a_{1:T}$, which will survive to all resampling steps in a PF. The other $N-1$ trajectories are generated using the steps described in Algorithm 2 (in a bootstrap implementation), as usual. Thus, the provided trajectory *conditions* the path of the other particles, hence the name conditional particle filter. This slight modification to the PF algorithm allows to use it within the sampling scheme 4.30 without changing the limiting distribution.

In complement, Lindsten, Jordan, and Schön, 2014 extended this approach proposing the CPF-AS, which improves the mixing of the particle system by adjusting the conditioning particle path at each iteration of the PF, maintaining the invariance property. The keypoint of this variation is the ancestor path of the conditioning trajectory. It is constructed at each iteration, instead of being set deterministically. The method is summarized in Algorithm 5 and is explained as follows.

Consider that a conditional particle trajectory $\boldsymbol{x'}_{1:T}$ is first defined. Additionally, at time $t-1$, the set of N weighted samples $\left\{\boldsymbol{x}^i_{1:t-1}, w^i_{1:t-1}\right\}_{i=1}^N$ is also available. Following a PF algorithm, the propagation of the these samples includes a resampling stage based on their weights. At this point, it is required to include a tracking of each particle's ancestors $\left\{a^i_t\right\}_{i=1}^N$, as mentioned in Section 4.1.2. In this way, the genealogy of each new particle can be traced.

Then, a new set of particles $\left\{\boldsymbol{x}^i_t\right\}_{i=1}^N$ is drawn using the transition model (in a bootstrap strategy) to the resampled particles,

$$\boldsymbol{x}^{(i)}_t \sim f(\boldsymbol{x}_t|\boldsymbol{x}^{a^{(i)}_t}_{t-1}, \boldsymbol{\gamma}) \tag{4.31}$$

Subsequently, the state ancestry path until time t is ordered/augmented as: $x^{(i)}_{1:t} = \left\{\boldsymbol{x}^{a^{(i)}_t}_{1:t-1}, \boldsymbol{x}^{(i)}_t\right\}$. In contrast with a standard PF, where the resampling/propagated stage is done for N particles, the CPF approach requires that x'_t to be included in the set $\left\{\boldsymbol{x}^i_{1:t}\right\}_{i=1}^N$. This is straightforwardly achieved by making the last particle $x^N_t = x'_t$.

Following, the key point of the CPF-AS arises: the trajectory of $\boldsymbol{x}^N_t$ is constructed by linking this particle with an ancestor at time $t-1$. This is, a^N_t is drawn with probability given by:

$$w^i_{t-1|t} \sim w^i_{t-1} f(\boldsymbol{x}'_t|\boldsymbol{x}^i_{t-1}, \boldsymbol{\gamma}) \tag{4.32}$$

Finally, the measurement update stage to update the importance weights is done, as in any standard PF. The procedure is completed by sampling an entire state trajectory $\boldsymbol{x}^*_{1:T}$ based on the weights w^i_T, which concludes (4.30a) in the Gibbs sampler. It has been demonstrated that the computational cost of this approach is linear in the number of particles, and contrary to a standard PF or particle smoothing algorithms, few particles (5 to 100, depending on the application) are required to obtain a good

mixing (Lindsten, Schön, and Jordan, 2013; Lindsten and Schön, 2013). This point is clearly and advantage since the computational effort can be reduced, still obtaining accurate approximations of the JSD.

Algorithm 5 Conditional Particle Filter with Ancestor Sampling

1: **Initialize:**
   Set the parameters $\boldsymbol{\gamma}$
   Draw $\left\{\boldsymbol{x}_1^i\right\}_{i=1}^N$ from the initial distribution $\mu(\boldsymbol{x_1})$
   Set $\boldsymbol{x}'_{1:T}$ arbitrarily, and make $\boldsymbol{x}_1^N = \boldsymbol{x}'_1$
2: **Measurement Update:**
   Compute the importance weights $\left\{\bar{w}_1^i\right\}_{i=1}^N$
   Normalize the particles weights $w_1^i = 1/\sum_i \bar{w}_1^i$
3: **for** $t = 2$ **to** T **do**
4: Apply a resampling step to get $\left\{a_t^i, \boldsymbol{x}_t^{a_t^i}\right\}_{i=1}^{N-1}$
5: Propagate resampled particles to time t,

$$\boldsymbol{x}_t^i \sim f(\boldsymbol{x}_t|\boldsymbol{x}_{t-1}^{a_t^i}, \boldsymbol{\gamma}) \quad \forall i < N$$

6: Make $\boldsymbol{x}_t^N = \boldsymbol{x}'_t$
7: Get the ancestor index for x_t^N according to:

$$P(a_t^N = i) \propto w_{t-1}^i f(\boldsymbol{x}_t^N|\boldsymbol{x}_{t-1}^i, \boldsymbol{\gamma})$$

8: Update/arrange the state trajectories until time t: $\boldsymbol{x}_{1:t}^i = \left\{x_{1:t}^{a_t^i}, x_t^i\right\}_{i=1}^N$
9: **Measurement Update:**
   Compute the importance weights $\left\{\bar{w}_t^i\right\}_{i=1}^N$
   Normalize the weights $w_t^i = 1/\sum_i \bar{w}_t^i$
10: **end for**
11: Sample a single trajectory $\boldsymbol{x}_{1:T}^j$ ($j \in \{1, 2, \ldots, N\}$), according to:

$$P(j = i) \propto w_T^i$$

12: Make $\boldsymbol{x}_{1:T}^* = \boldsymbol{x}_{1:T}^j$

Now the state $\boldsymbol{x}_{1:T}^*$ is available, the next step in the Gibbs sampler, (4.30b), can be addressed. A bayesian approach is chosen

$$p(\boldsymbol{\gamma}|\boldsymbol{x}_{1:T}^*[k], \boldsymbol{y}_{1:T}) = \frac{p(\boldsymbol{x}_{1:T}^*[k], \boldsymbol{y}_{1:T}|\boldsymbol{\gamma})\pi(\boldsymbol{\gamma})}{p(\boldsymbol{x}_{1:T}^*[k], \boldsymbol{y}_{1:T})} \tag{4.33}$$

For some models, choosing a conjugate prior to the likelihood result in a closed expression for this parameter posterior. However, the model employed in this work does not admit such formulation. Thus, the problem of getting samples from this posterior is addressed using a MH sampler. To this aim, the same steps listed in

Algorithm 3 are employed, where the acceptance probability becomes

$$A(\boldsymbol{\gamma}'|\boldsymbol{\gamma}) = min\left\{1, \frac{p(\boldsymbol{\gamma}'|\boldsymbol{x}^*_{1:T}[k], \boldsymbol{y}_{1:T})}{p(\boldsymbol{\gamma}|\boldsymbol{x}^*_{1:T}[k], \boldsymbol{y}_{1:T})} \frac{q(\boldsymbol{\gamma}|\boldsymbol{\gamma}')}{q(\boldsymbol{\gamma}'|\boldsymbol{\gamma})}\right\} \tag{4.34}$$

$$= min\left\{1, \frac{p(\boldsymbol{x}^*_{1:T}[k], \boldsymbol{y}_{1:T}|\boldsymbol{\gamma}')\pi(\boldsymbol{\gamma}')}{p(\boldsymbol{x}^*_{1:T}[k], \boldsymbol{y}_{1:T}|\boldsymbol{\gamma})\pi(\boldsymbol{\gamma})} \frac{q(\boldsymbol{\gamma}|\boldsymbol{\gamma}')}{q(\boldsymbol{\gamma}'|\boldsymbol{\gamma})}\right\} \tag{4.35}$$

Where, $\pi(\gamma)$ is the prior on the parameters and can be chosen to summarize the previous knowledge about them. If this is not the case, non-informative priors can also be employed, as described by Yang, Drive, and Berger, 1998. Thus, both $\pi(\cdot)$ and $q(\cdot)$ are "hyperparameter distributions" subject to the user design criteria. Once the MH algorithm is completed, one iteration of the Gibbs sampler (4.30) is also executed and a valid pair $\boldsymbol{\gamma}, \boldsymbol{x}_{1:T}$ is generated. The entire process, including the CPF-AS and the parameter sampling as described here and summarized in Algorithm 6 constitutes the approach called Particle Gibbs with Ancestor Sampling (PGAS). It provides a practical implementation of a Gibbs sampler with stationary distribution $p(\boldsymbol{\gamma}, \boldsymbol{x}_{1:T}|\boldsymbol{y}_{1:T})$.

Algorithm 6 Particle Gibbs with Ancestor Sampling

1: **Initialize:**
   Set $\boldsymbol{\gamma}[1]$ and $\boldsymbol{x}'_{1:T}[1]$
2: **for** $k = 2$ **to** K **do**
3: Draw $\boldsymbol{x}^*_{1:T}[k]$ by running Algorithm 5 conditionally on $\boldsymbol{x}'_{1:T}[k-1]$
4: Draw $\boldsymbol{\gamma}[k]$ by running steps 4 to 10 of Algorithm 3
5: Set $\boldsymbol{x}'_{1:T}[k] = \boldsymbol{x}^*_{1:T}[k]$
6: **end for**

To get a deeper description of the sampling algorithms presented in this Section, as well as proofs of convergence and theoretical details, the reader is referred to Lindsten, 2013 and the references therein.

4.3 Mobile Robot Model with Non-zero Slip

To model the vehicle motion, the 3D articulated multibody system approach described in Seegmiller, 2014 was employed. This approach was chosen mainly for two reasons: the proposed calibration methodology can be tested in a skid-steered robot, with room for straightforward modifications if using vehicles with more complex configurations; and it provides two formulations that accounts for non-zero wheel slip. The first formulation is a kinematic model which predicts body-level slip based on gravitational, inertial and dissipative forces. The second is a dynamical model that accounts for wheel-terrain forces by using various wheel-ground contact sub models in a modular scheme (e.g., the Pacejka magic formula or the Bekker-Wong model). Since both formulations have proven to be equivalent in several test cases, the kinematic model was adopted in this work. However, as will be discussed later, a dynamic model calibration is also possible.

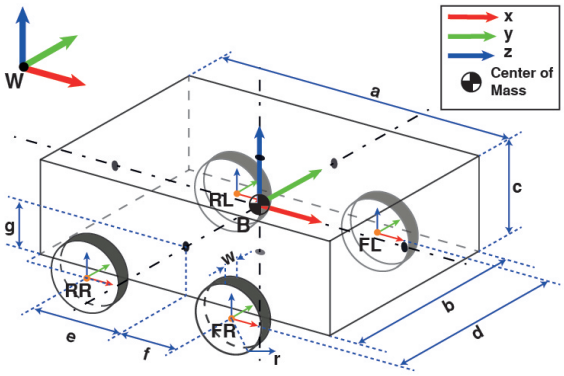

FIGURE 4.3: Schematic diagram of a generic 4-wheeled mobile robot showing the placement of the world (W), body (B), front right (FR), front left (FL), rear right (RR) and rear left (RL) wheel frames. All variables depicted here are required to fully determine the robot model and are summarized in Table 4.2.

4.3.1 Model information

The model is constructed by first specifying a kinematic tree that roots at the main body of the robot. Each branch corresponds to joints with articulations, suspension links or wheels. The main body has six degrees of freedom (DOF) with respect to the global coordinate system and each branch has only one DOF with respect to its parent. It is important to point out that this approach does not necessarily requires the use of the Denavit-Hartenberg convention for the placement of the joint locations.

For simplicity, the contact surface between the terrain and the wheel is considered as a single point, which terminates each branch of the tree. This point has attached a contact frame whose z axis coincides with the normal of the terrain at that point. The x and y axes correspond to the longitudinal and lateral slip directions, respectively. Figure 4.3 schematically depicts the frame placement in each joint and contact points following the methodology described previously. Additionally, mass, center of mass (*COM*) and moment of inertia also have to be specified for the vehicle body and wheels. Table 4.2 summarizes the information required to define the model of any articulated mobile robot.

State Vector

The state of the vehicle is described by the position and orientation of the main body with respect to the world coordinate frame, along with the position displacement of each prismatic or revolute joints. Thus, the state vector which defines completely the position of the robot and its joints in the space is:

$$\boldsymbol{x} = \begin{bmatrix} \mathbf{q}_b^w \\ \boldsymbol{\theta} \end{bmatrix}, \mathbf{q}_b^w = \begin{bmatrix} \mathbf{o}_b^w & {}^w\mathbf{r}_b^w \end{bmatrix}^T \tag{4.36}$$

where $\mathbf{q}_b^w$ include the orientation ($\mathbf{o}_b^w$) and the position (${}^w\mathbf{r}_b^w$) of the main body in global coordinates. The remaining element in the state vector ($\boldsymbol{\theta}$) corresponds to displacements of the prismatic/revolute joints.

Kinematic Predictive Model

To predict the robot motion, the joint spatial velocity ($\dot{\boldsymbol{x}}'$) is first found by solving the complete constraint equation:

$$A(\boldsymbol{x})\dot{\boldsymbol{x}}' = \boldsymbol{v_c} \tag{4.37}$$
$$\begin{bmatrix} A_{wheels} \\ A_{joint} \end{bmatrix} \dot{\boldsymbol{x}}' = \begin{bmatrix} \boldsymbol{v_c} \\ \boldsymbol{v_{joint}} \end{bmatrix}$$

TABLE 4.2: Summary of frames placement and parameters required for the kinematic modelling formulation. All dimensions are measured considering the body frame and the robot's center of gravity are coincident.

i	1	2	3	4	5
Frame Name	Body (B)	FR	FL	RR	RL
Parent	World (W)	Body	Body	Body	Body
Type	-	Revolute	Revolute	Revolute	Revolute
Actuated	-	Yes	Yes	Yes	Yes
x	-	f	f	-e	-e
y	-	$-\frac{d}{2}$	$\frac{d}{2}$	$-\frac{d}{2}$	$\frac{d}{2}$
z	-	g	g	g	g
θ_x	-	0	0	0	0
θ_y	-	0	0	0	0
θ_z	-	0	0	0	0
Inertia about COM	$\frac{M}{12}\begin{bmatrix} b^2+c^2 & 0 & 0 \\ 0 & a^2+c^2 & 0 \\ 0 & 0 & a^2+b^2 \end{bmatrix}$	$\frac{m_i}{12}\begin{bmatrix} 3r^2+w^2 & 0 & 0 \\ 0 & 6r^2 & 0 \\ 0 & 0 & 3r^2+w^2 \end{bmatrix}$			
Wheelbase	e+f				
Track	d				

This expression includes both non-holonomic and holonomic constraints for all wheels and certain joints (e.g., those with symmetric relative movement). The term A_{wheels} holds for the wheel Jacobians, which transform the movement of all the contact points from their local coordinates to the body reference frame. It consists on three rows per wheel: the first two rows restrict the longitudinal and lateral slip velocities; whereas the third row restrict the movement in the normal direction of the contact point. Thus, $\boldsymbol{v_c}$ corresponds to contact point velocities for each wheel. In addition, A_{joint} restricts the time derivative of the holonomic joint constraints ($\boldsymbol{v_{joint}}$), if present. After solving this equation for $\dot{\boldsymbol{x}}'$, the motion kinematics is integrated using the Euler's method to get the robot state:

$$\boldsymbol{x}[t+1] = \boldsymbol{x}[t] + V(\boldsymbol{x}[t])\dot{\boldsymbol{x}}'[t]\delta t \tag{4.38}$$

where δt is the sample time. It is important to note that the joint spatial velocity obtained is measured in the body coordinate frame. Therefore, the linear transformation $V(\boldsymbol{x})$ is required to obtain the time derivative of the body frame pose in world coordinates ($\dot{\boldsymbol{x}}$).

4.3.2 Kinematic Model with Non-zero Slip

In contrast with dynamic formulations that relate wheel slip and contact forces, the kinematic slip parametrization described in this Section accounts for the effects of slippage in the movement of the robot. Thus, an accurate estimation of wheel slip resulting of forces of the wheel-terrain interaction is not guaranteed in this case (as necessary for traction control, for example); however, the motion of the robot accounting for non-zero slip can be properly described/predicted.

Body level slip velocity (linear and angular) is parametrized as function of the robot's velocity, as well as inertial and gravitational forces acting on its center of gravity, as follows:

$$\boldsymbol{v_{cg}} = \begin{bmatrix} p_1 \frac{f_x}{f_z} V_x + p_2 V_x & p_3 \frac{f_y}{f_z} V_x & 0 \end{bmatrix}^T \tag{4.39}$$

$$\boldsymbol{\omega_{cg}} = \begin{bmatrix} 0 & 0 & p_4 \frac{f_y}{f_z} V_x + p_5 V_x + p_6 \omega_z \end{bmatrix}^T \tag{4.40}$$

where fx, fy and f_z represent the x, y and z components of the forces acting on the vehicle body, but transformed to contact point coordinates. The terms V_x and ω_z are the linear and angular velocities of the robot in the x and z axis, respectively. It is worth to note two points in this parametrization: the dimensions of each parameter ensure the proper dimensionality of $\boldsymbol{v_{cg}}$ and $\boldsymbol{\omega_{cg}}$, and all variables are expressed with respect to the robot's center of mass. If the body frame is located in other point, a linear transformation is additionally required. Finally, the joint space velocity is obtained:

$$\dot{\boldsymbol{x}}' = \dot{\boldsymbol{x}}'_{n\_slip} + \dot{\boldsymbol{x}}'_{slip} = \begin{bmatrix} \boldsymbol{\omega}_{\boldsymbol{b}}^{\boldsymbol{w}} + \boldsymbol{\omega_{cg}} \\ {}^{\boldsymbol{b}}\boldsymbol{v}_{\boldsymbol{b}}^{\boldsymbol{w}} + \boldsymbol{v_{cg}} \\ \dot{\boldsymbol{\theta}} \end{bmatrix} \tag{4.41}$$

Subsequently, the robot motion can be integrated by using Eq. 4.38. The reader is referred to the original work of Seegmiller, 2014 to get a deep description about the calculation of all variables involved in this formulation.

4.4 Implementation Details

This Section describes the practical application of the estimation approach described for identifying the slip parameters of the robot model presented in Section 4.3. In this case, the parameter vector is defined as $\boldsymbol{\gamma} \triangleq [p_1, p_2, p_3, p_4, p_5, p_6] \in \Gamma$, where Γ is a suitable subspace of $\mathbb{R}^6$. The functional implementation adopted in this work can be summarized in the following three keypoints:

- Obtaining the likelihood $p(\boldsymbol{x}^*_{1:T}[k], \boldsymbol{y}_{1:T}|\boldsymbol{\gamma})$ for the non-zero slip model.
- Initialization of the CPF and design of the "hyperparameter distributions" for the MH sampler.
- Data stream availability and usage (i.e., sequential updating or batch estimation).

4.4.1 State-Parameter Likelihood

To calculate the acceptance probability in the MH sampler, it is necessary to evaluate the likelihood in Eq. 4.33. In general, for a system with state dynamics and measurement modelled by the probability density functions $f(\cdot)$ and $g(\cdot)$, the likelihood is given by

$$p(\boldsymbol{x}_{1:T}[k], \boldsymbol{y}_{1:T}|\boldsymbol{\gamma}) = \mu(\boldsymbol{x}_1) \prod_{t=1}^{T} g(\boldsymbol{y}_t|\boldsymbol{x}_t) \prod_{t=2}^{T} f(\boldsymbol{x}_t|\boldsymbol{x}_{t-1}, \boldsymbol{\gamma}) \tag{4.42}$$

where $\mu(\cdot)$ is the distribution of the initial state. Since the aim is to estimate the slip parameters $\boldsymbol{\gamma}$ only the state transition are dependent on the parameters. If other variables are to be estimated (e.g., process or measurement covariances), they have to be properly included in this expression. For the modelling presented in Section 4.3, considering a normal density for f, the likelihood is:

$$K_1 exp\left\{-\frac{1}{2}\sum_{t=1}^{T-1}(\boldsymbol{x}_{t+1} - \hat{\boldsymbol{x}}_{t+1})^T \Sigma^{-1} (\boldsymbol{x}_{t+1} - \hat{\boldsymbol{x}}_{t+1})\right\} \tag{4.43}$$

$$= K_1 exp\left\{-\frac{1}{2}\sum_{t=1}^{T-1}\left(\bar{\boldsymbol{x}}_t - \delta t V X_t^f \xi_t \boldsymbol{\gamma}\right)^T \Sigma^{-1} \left(\bar{\boldsymbol{x}}_t - \delta t V X_t^f \xi_t \boldsymbol{\gamma}\right)\right\} \tag{4.44}$$

$$= K_1 K_2 exp\left\{-\frac{1}{2}\sum_{t=1}^{T-1}\left[(C_t\boldsymbol{\gamma})^T \Sigma^{-1} C_t \boldsymbol{\gamma} - 2\bar{\boldsymbol{x}}_t^T \Sigma^{-1} C_t p\right]\right\} \tag{4.45}$$

with K_1 and K_2 including all the terms that are not function of the parameters, and

$$\hat{\boldsymbol{x}}_{t+1} = \boldsymbol{x}_t + \delta t V \dot{\boldsymbol{x}}'_{n\_slip} + \delta t V \dot{\boldsymbol{x}}'_{slip} \tag{4.46}$$

$$\bar{\boldsymbol{x}}_t = \boldsymbol{x}_{t+1} - \boldsymbol{x}_t - \delta t V \dot{\boldsymbol{x}}'_{n\_slip} \tag{4.47}$$

$$C_t = \delta t V X_t^f \xi_t \tag{4.48}$$

Here $\dot{\boldsymbol{x}}'_{n\_slip}$ denote the joint space velocity of the robot with zero slip, and $\dot{\boldsymbol{x}}'_{slip}$ its slip component. In addition, the term X^f corresponds to a coordinate transformation from the vehicle *COM* to its body frame, if both are not coincident. Finally, $\xi\boldsymbol{\gamma}$ is a matrix representation of equations 4.39 and 4.40.

4.4.2 Initialization of CPF-AS and Hyperparameter Distributions

This Section describes the practical details regarding the CPF and the MH sampler. First, a conditional particle trajectory is required for the initialization of the PGAS algorithm. While theoretically any initial state trajectory $\boldsymbol{x}'_{1:T}[1]$ can be employed, better results were observed when setting it to values different from zeros, ones or random. Thus, prior to begin with the identification algorithm, it is required to run a filtering pass to get a better value of the conditional trajectory. To this aim, any filtering/smoothing approach can be employed. In this work,a CPF-AS with 100 particles was employed, which in turn was initialized with a set of ones. This setting allowed to run the identification CPF-AS with only 50 particles.

For the MH sampler, a random walk with zero mean and covariance Λ was used for the proposal distribution $q(\cdot|\boldsymbol{\gamma})$. It is usually employed in this type of samplers since its symmetry property simplifies the term involving the proposal in the acceptance probability. The parameter prior $\pi(\boldsymbol{\gamma})$, on the other hand, was chosen attending a practical aspect. All parameters are related with certain variables involved in the terrain-wheel interaction. Thus, simulation tests allowed to determine proper intervals from which these parameters can take values (see Section 4.6). Thus, for all of them, uniform distributions within the double of the largest interval (i.e., $[-2, 2]$) were established. This selection was also in accordance with a Jeffreys non-informative prior. It consists in uniform distributions which are suitable when few information about the parameter evolution is available (Yang, Drive, and Berger, 1998). If other information coming for example from exteroceptive sensors would be available, it can be included somehow to modify this prior. With these two "hyperparameter distributions" set as explained, the acceptance probability is given by:

$$A = \begin{cases} min\left\{1, \frac{p(\boldsymbol{x}^*_{1:T}[k], \boldsymbol{y}_{1:T}|\tilde{\boldsymbol{\gamma}})}{p(\boldsymbol{x}^*_{1:T}[k], \boldsymbol{y}_{1:T}|\boldsymbol{\gamma})}\right\} & \text{if } -2 \leq p_i \leq 2,\ \forall p_i \in \gamma \\ 0 & \text{otherwise} \end{cases} \tag{4.49}$$

4.4.3 Sensor Measurements and Batch Estimation

Since a kinematic model is employed, only pose and attitude measurements are required to run the identification algorithm. Thus, the measurement model does not involve any intricate density since the state is directly obtained. In simulation, measurements consisted in the robot pose with additive noise, while a global positioning receiver and inertial sensors were employed in real tests. With this information, the measurement update in the CPF-AS is done as a standard bootstrap PF.

As can be noted in Section 4.2, the PG-AS algorithm is defined for a set of data from $t = 1$ to $t = T$. For a mobile robot that is moving around and traversing diverse terrain types (i.e., parameters are changing), a batch estimation approach is then suitable. Hence, a slight change in the original algorithm was introduced to follow a sequential-batch idea. Denoting the observed dataset for a complete calibration path of the robot as $\mathcal{Y} = \{\mathbf{Y}_1, \mathbf{Y}_2, \ldots, \mathbf{Y}_F\}$, with $\mathbf{Y}_1 = \boldsymbol{y}_{1:T}$, $\mathbf{Y}_2 = \boldsymbol{y}_{T+1:2T}$ and so on. Accordingly, the set of states are defined $\mathcal{X} = \{\mathbf{X}_1, \mathbf{X}_2, \ldots, \mathcal{X}_F\}$ with $\mathbf{X}_1 = \boldsymbol{x}^*_{1:T}$, $\mathbf{X}_2 = \boldsymbol{x}^*_{T+1:2T}$, and so forth. Then, Eq. 4.33 is updated for the batch processing according to:

$$\begin{aligned} p(\boldsymbol{\gamma}|\mathbf{Y}_1, \mathbf{X}_1) &= \frac{1}{\mathcal{Z}_1} p(\mathbf{X}_1, \mathbf{Y}_1|\boldsymbol{\gamma})\pi(\boldsymbol{\gamma}) \\ p(\boldsymbol{\gamma}|\mathbf{Y}_2, \mathbf{X}_2) &= \frac{1}{\mathcal{Z}_2} p(\mathbf{X}_2, \mathbf{Y}_2|\boldsymbol{\gamma}) p(\boldsymbol{\gamma}|\mathbf{Y}_1, \mathbf{X}_1) \\ &\vdots \\ p(\boldsymbol{\gamma}|\mathbf{Y}_F, \mathbf{X}_F) &= \frac{1}{\mathcal{Z}_F} p(\mathbf{X}_F, \mathbf{Y}_F|\boldsymbol{\gamma}) p(\boldsymbol{\gamma}|\mathbf{Y}_F - 1, \mathbf{X}_F - 1) \end{aligned} \tag{4.50}$$

This updating process holds if $\mathbf{Y}_i$ and $\mathbf{X}_i$ are independent of both $\mathbf{Y}_j$ and $\mathbf{X}_j$, $\forall i, j \in [1, F]$ with $i \neq j$. Independence of $\mathbf{Y}_i$ is trivially guaranteed, however, independence of $\mathbf{X}_i$ and $\mathbf{X}_j$ is more complicated. To deal with this point, a practical artifice was

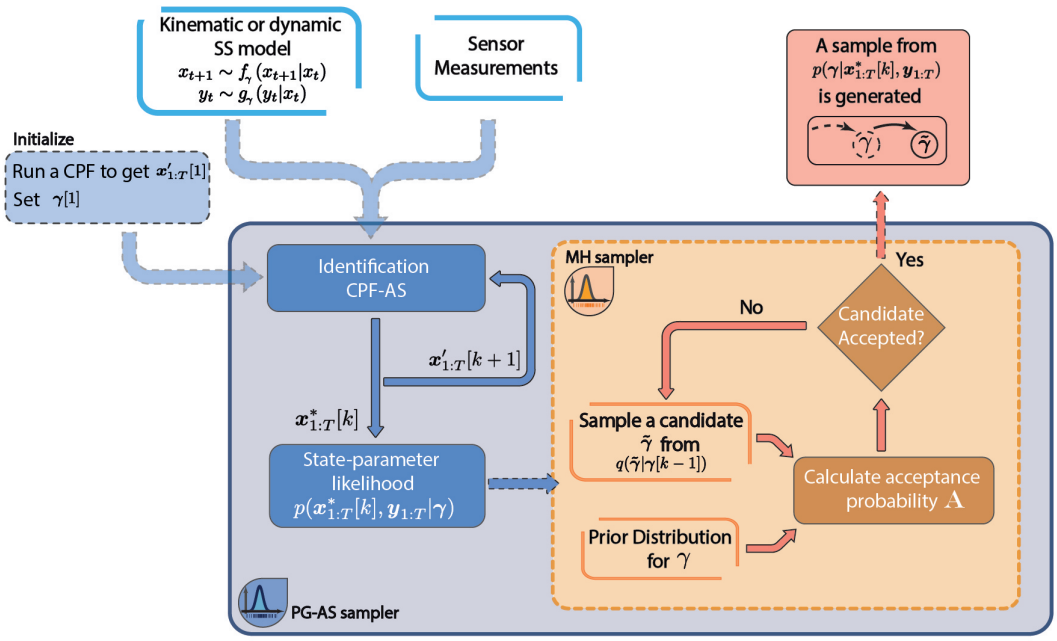

FIGURE 4.4: Architecture of the proposed system identification methodology for nonzero slip models of mobile robots. A single iteration of the PGAS algorithm is shown in the blue box. In the batch framework employed in this work, this procedure is repeated M times for each measurement element collection in the set $\mathcal{Y} = \{\mathbf{y}_{1:T}, \mathbf{y}_{T+1:2T}, \mathbf{y}_{T+2:3T}, \dots\}$.

employed: at the beginning of the estimation process for a specific batch, the state $\mathbf{X}_i$ is initialized only as function of the initial measurements in Y_i. Figure 4.4 schematically depicts the architecture of the overall identification system.

Despite of this formulation uses a fixed time T to define each batch, the practical implementation of the methodology employed a fixed distance travelled Δs instead. The idea remains the same, but this approach is more intuitive and practical. Considering the speed of the robots can be variable (even zero at certain times), this decision ensured enough area to travel and to get enough representative measurements for each batch.

4.5 Testbed

Slippage as one of the most prominent effects of the wheel-terrain contact is function of vehicle's size, weight and power, among other variables (including the terrain-related) (Wong, 2010). For example, compared to big earthmoving machines, small-sized robots exert less pressure on the soil but also their motors produce a smaller thrust Wong, 2001. Thus, different slip behaviours would be observed (depending on the compactness of the terrain), causing diverse possible parametrizations which increase uncertainty in the model. Additionally, the uncertainty can also be increased by the characteristics of the robot (e.g., the *COM* can vary in vehicles with moving parts). For these reasons, two robotic vehicles were employed to test the proposed

identification approach: a Pioneer 3AT and an industrial miniloader. Simulation first allowed to validate the methodology in both vehicles. Subsequently, field terrain experiments were conducted on the industrial miniloader to assess the overall strategy in a machine working on real conditions.

The small-sized Pioneer 3-AT from Mobile Robots Llc (Figure 4.5, right), is part of the robotics laboratory at Universidad Técnica Federico Santa María. It is a research unit with 4 wheels which can reach a maximum of $0.7m/s$ and $140^o/s$, for linear and angular speeds, respectively. Depending on the surface on which it is navigating it can support loads up to $12Kg$. Additionally, the Pioneer 3AT is electrically-driven, with a supply voltage of $12volts$. The variables required to model this robot with the approach described in Section 4.3 are detailed in Table 4.3. Given the robot characteristics (compactness and weight), the *COM* was placed as the geometric center of the robot bounding box.

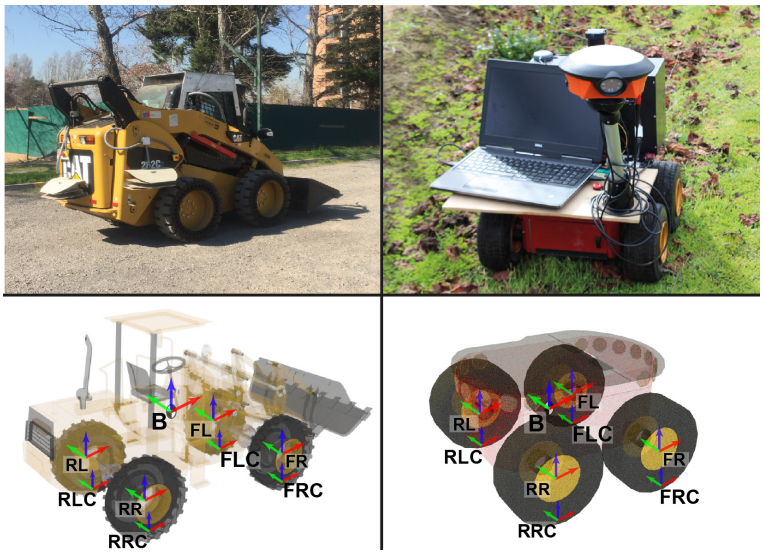

FIGURE 4.5: Mobile robots employed in this work. The first row shows an semi-automated compact miniloader and a Pioneer 3-AT. The second row shows a 3D rendering of both robots with the corresponding frame placement, as described in Figure 4.3. Contact points frames are also included for each wheel.

The miniloader employed in this work is a CAT 262c® earthmoving machine (Fig. 4.5 left). For research purposes, it was robotised by including wheel encoders, stereo imagery, inertial measurements, global positioning receivers among other sensors in a modular scheme. The robot was also included with an industrial computer inside, which allows three operation modes: autonomous, teleoperated and manual. It has a diesel engine and can reach speeds up to $3.5m/s$. The modelling variables for this robot are summarized in Table 4.3.

It is noteworthy that in contrast to the pioneer, election of the *COM* for the CAT was a little more complicated. Movement in the arm and bucket change the inertial characteristics of the vehicle, which is an important point to take into account. However, given the bucket mass together are less than half of the body mass (without load), the *COM* was placed in the geometric center of the body for all of the trials.

TABLE 4.3: Model parameters for the Pioneer 3AT and the compact miniloader.

Description	Reference Variable	Pioneer 3AT	Miniloader
Body length [m]	(a)	0.51	2.98
Body width [m]	(b)	0.32	1.13
Body height [m]	(c)	0.19	1.45
Track [m]	(d)	0.41	1.68
Wheelbase	(e)	0.13	0.40
	(f)	0.13	0.84
Wheel-*COM* height [m]	(g)	6.85	0.54
Wheel radius [m]	(r)	0.11	0.42
Wheel width [m]	(w)	0.09	0.28
Body Mass [Kg]	(M)	12.00	3423.00
Wheel Mass [Kg]	(m_i)	3.62	47.70

In the field experiments, tests to assess this election in the estimation were included, since it can be accounted in the modelling uncertainty.

4.6 Simulation

The simulator employed in this work is an open source software based on the modelling approach described in Section 4.3 (Seegmiller and Kelly, 2016). It is implemented in the Matlab programming environment, with room to include various terrains and mobile robots, as shown in Fig.4.6. All the processing was carried out using a computer with a 2.60 GHz Corei7 processor and 16GB of RAM.

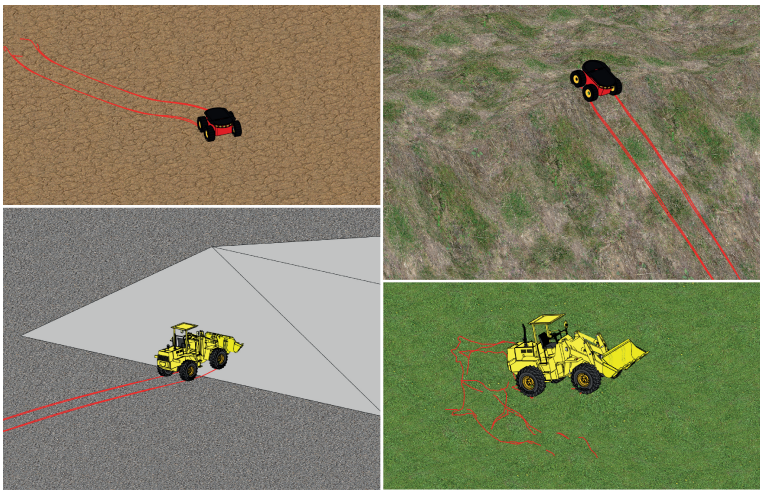

FIGURE 4.6: Simulation environment where different terrain types/configurations and robots can be included. The red trace marks the path followed by the robot on the terrain. The pioneer 3AT and the CAT 262c are the vehicles used in simulation for this work.

Simulation tests are mainly employed for evaluating the mobility prediction, parameter convergence and posterior distributions in two scenarios: when the vehicle

TABLE 4.4: Summary of the parameter values employed for the simulation of the kinematic slip model.

Parameter	Range	Analogous physical variable/effect
p_1	(-1,1)	Slip longitudinal force relationship
p_2	[0,0.5]	Rolling resistance
p_3	(-1,1)	Slip lateral force relationship
p_4	(-1,1)	Oversteer/understeer behaviour
p_5	[-0.5,0.5]	Asymmetry in rolling resistance
p_6	[0,0.5]	Anisotropic friction during skidding

is driving on a single terrain and when it is navigating on heterogenous soil surfaces. Prior to these tests, the simulator was also used to empirically get parameter sets that produced slip behaviours without affecting the vehicle manoeuvring in a big extent. To modify the parameters in the range of values possibly obtained in real experiments, a characteristic of the slip modelling presented in Section 4.3.2 was used: parameters in equations 4.39 and 4.40 are related with certain terra-mechanical effects/variables, as described by Seegmiller and Kelly, 2016. Table 4.4 summarizes the ranges used in this work along with the analogous effects/variables of the robot motion. The criteria employed to choose such values is explained as follows:

- Parameter p_1, analogously to the longitudinal stiffness, accounts for a relationship between force and slip velocity (Wong, 2001). It is a scaling factor of the term f_x/f_z, which can no be close to 1 or -1, since it is physically impossible (the vehicle would have lifted-off).

- Term p_2 is comparable with the rolling resistance. In experimental tests for various tyres in diverse conditions reported by Wong, 2001, rolling resistance does not exceed 0.5.

- The third parameter is similar to p_1, but it accounts for the force slip relationship in the lateral direction. In this case, a roll-over situation would be imminent if the term f_y/f_z is close to 1 or -1.

- Oversteer or understeer behaviour is accounted in p_4. Since it is the same factor involving p_3, both were modified in the same range.

- Asymmetry in rolling resistance possibly representing a difference in the inflation pressure (or wear) in the tyres is considered by p_5. The interval chosen considers asymmetry to the right or left side of the vehicle.

- Term p_6 accounts for the angular slip produced due to anisotropic friction during skidding. Thus, part of the angular velocity would contribute to angular slip, specially in skid-steered robots.

For all the tests, results from the proposed PGAS identification methodology were compared with the Integrated Perturbation Error Minimization (IPEM) approach (Seegmiller et al., 2013). Briefly, the IPEM methodology consists in integrating state predictions over an time horizon for subsequently comparing them with position measurements, producing pose residuals. To change the parameters in a way that these

TABLE 4.5: Parameters employed to simulate a single terrain. Values for each case were randomly selected from the intervals listed in Table 4.4.

	Pioneer 3AT	Miniloader
p_1	0.050	0.250
p_2	0.100	0.200
p_3	-0.100	0.100
p_4	0.090	0.015
p_5	0.100	0.060
p_6	0.050	0.010

residuals are minimized, the prediction is linearised with respect to the parameters. The Jacobian matrix produced is then employed in a Extended Kalman Filter scheme to obtain the parameter estimations. Employing this method reports effective identification results for models of powertrain dynamics, slippage and odometry in simple and complex vehicles (Rogers-Marcovitz and Kelly, 2010; Ordonez et al., 2017).

4.6.1 Single Terrain

In order to simulate a single terrain, a fixed set of parameters were employed. Table 4.5 shows the values employed for each vehicle, which were randomly drawn from an uniform distribution defined within the intervals described before. Additionally, to test repeatability, the robots were manually driven in 10 different trajectories using a joystick. Each one of them consisted of 5 minutes of driving at maximum speed through the virtual world at a sampling rate of 0.1secs. The distance to define each batch in these trajectories was set $\Delta s = 30m$. In early tests it was found that acceptable distances to run the algorithm were in the range 10-30m. This balanced a trade-off between getting enough information in a batch, and obtaining good calibration results.

The vehicles traversed plane and steep terrains, similar to the one shown at the bottom left of Fig 4.6. Thus, observability of the parameters related with gravity terms were ensured.

Regarding the "hyperparameter functions", the covariance matrix for the random walk was chosen as:

$$\Lambda = \begin{bmatrix} 0.1 & 0 & 0 & 0 & 0 & 0 \\ 0 & 0.1 & 0 & 0 & 0 & 0 \\ 0 & 0 & 0.01 & 0 & 0 & 0 \\ 0 & 0 & 0 & 0.01 & 0 & 0 \\ 0 & 0 & 0 & 0 & 0.01 & 0 \\ 0 & 0 & 0 & 0 & 0 & 0.1 \end{bmatrix} \tag{4.51}$$

It is result of prior tests where it was observed that sampling from p_1, p_2 and p_6 required more variability to reach the true values. Conversely, p_3, p_4 and p_5 rapidly converged, requiring less variability to draw new candidates. It is noteworthy that increasing variances in this matrix produced a higher rejection rate in the MH

sampler, with any noticeable improvement. Finally, the parameter prior $\pi(\boldsymbol{\gamma})$ was set as described in Section 4.4.2.

The first simulation outcome to evaluate was the evolution of the posterior means for each parameter. Thus, a sort of maximum a posteriori estimation is obtained. Figures 4.7a and 4.7b show results for the pioneer and the miniloader, respectively. As can be noted, all of the sample means are fluctuating around the true values for almost all of the iterations and all the trajectories. However, in certain cases (e.g., trajectory 9 for the pioneer or trajectory 10 for the miniloader) the paths are less smoother than others. This is an indicator that an appropriate identification requires the vehicle to drive in a path that ensures observability of all the parameters. In fact, as reported by Antonelli, Chiaverini, and Fusco, 2005, a proper choice of the trajectories used to collect the measurements is crucial to correctly identify a kinematic model.

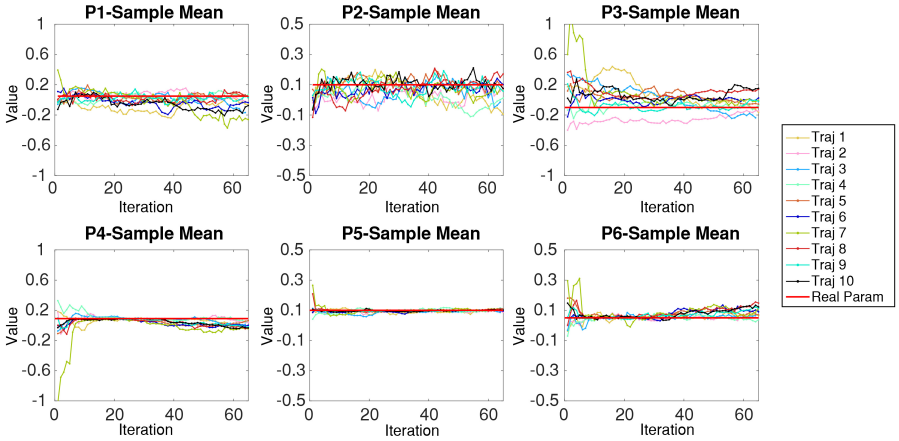

(A)

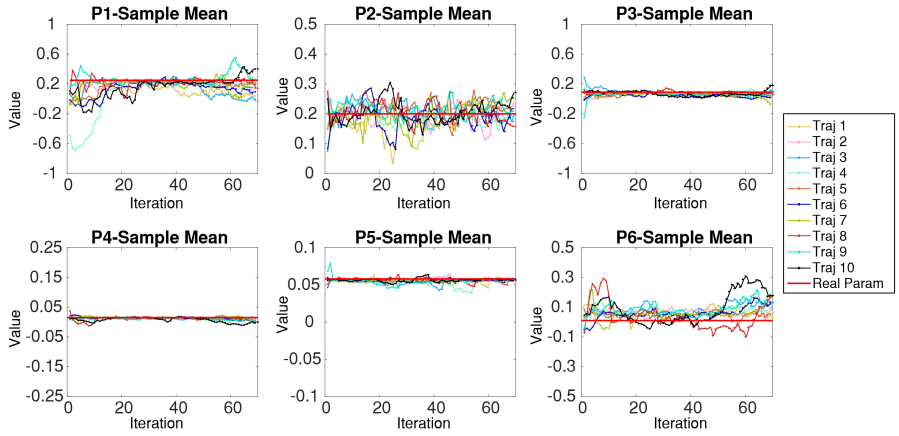

(B)

FIGURE 4.7: Evolution of the sample means of the six parameters for the Pioneer 3AT (A) and the miniloader CAT262c (B). A total of 10 calibration trials were simulated. Variability on the means for different cases indicate a strong dependency of the estimations with the trajectory followed by the robot.

Another interesting thing to note in these results is that in general, the parameter means of p_2, p_5 and p_6 are naturally bounded in the limits specified in Table 4.4 . This

is, despite of using a general constraint to sample between the interval $[-2, 2]$, the means of such particular parameters did not exceed the respective parameter limits. Furthermore, a deep insight about the samples generated shows that the region of high likelihood of the parameter posteriors is concentrated in the proper intervals. In fact, the capability to analyse these posteriors through the evolution of the samples generated is one of the advantages of the proposed method.

Figure 4.8a shows the evolution of the histograms obtained after each batch processing (iteration) in the second trajectory. At each batch, one histogram was constructed employing the 1000 samples from the parameter posterior, generated with the PGAS algorithm. For this particular case, more than 60 measurement batches were obtained. As can be seen, the red trace indicating the true parameter value always remains in the region of high probability (yellow hue) for all cases. Histograms of some parameters wider than others, indicating an increased uncertainty in those estimations. In fact, this result also agrees with the variability of the means observed in the previous figures. This outcome may indicate that the proposed model is not highly sensitive to changes in p_1, p_3 and p_6. In order to get a deeper insight of the evolution in the samples generated throughout the whole trajectory, Fig. 4.8b shows a "top view" of the draws from the parameter posteriors. In this case it is clear that samples from p_1 are more scattered than others. However, it can also be noted that the true parameter values remain within regions with a higher likelihood, not only for the first one but also for the other parameters. Another interesting point to highlight in this figure is the variability in the sample scattering, for different batches. For example, near iteration 50 of p_4, the posterior parameter distribution gets narrower. This clearly indicates that the measurement batch was rich in information about that parameter. At contrary, between iterations 40 and 50 of p_5, the posterior parameter distribution is thicker, which suggest that measurements from that part of the trajectory were not very informative for that parameter. With these type of analysis one may create a mapping between the control inputs and some "score of observability". This mapping would allow to develop optimal calibration trajectories that provide rich informative measurements with shorter routes. For clarity in the analysis and to avoid cumbersome graphic stacking, images corresponding only to the miniloader are shown. Results for the pioneer robot are shown in Appendix A.

An important characteristic about the PGAS method used is one can obtain samples not only from the parameters, but also of the robot state. This feature can be further employed to get insight about intermediate variables involved in the model calculation. To generate the K samples from the state, the model needs to be simulated the same number of times, thus generating K samples of such variables. For this thesis, it is of particular interest to assess the contact point velocities (cpv) of the robot with respect to the ground since they are closely related with wheel slippage (Wong, 2010). Given that 1000 samples of the parameters and the robot state were generated at each batch in the current implementation, the same number of cpv were also generated. Thus, a powerful consequence of the methodology employed arises: it provides a mean to consider these velocities (and therefore wheel slippage) as random variables. Furthermore, the distributions approximated by their samples would allow a probabilistic traversability assessment of the robot. For example, variability on the parameter estimations may be associated with uncertainty in the cpv for a specific terrain. Thus, one may predict if the robot is likely to experience slipping conditions

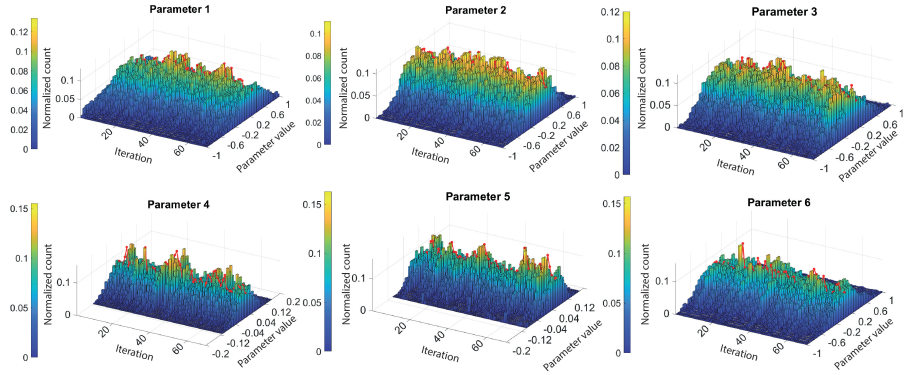

(A)

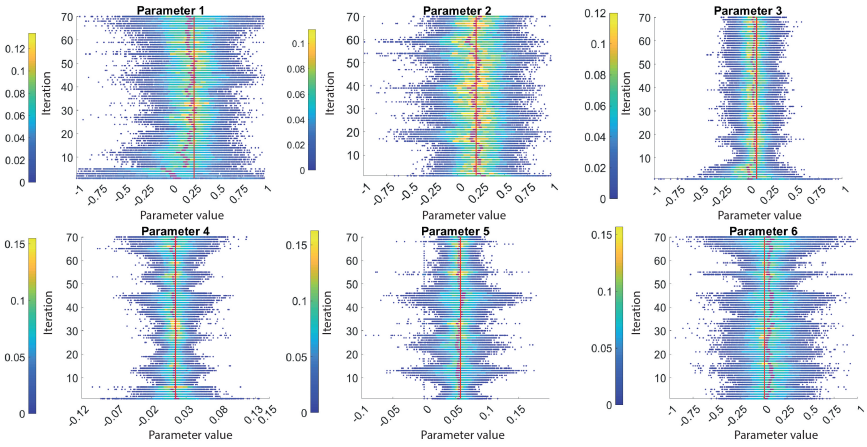

(B)

FIGURE 4.8: Evolution of the histograms (A) and sample population (B) generated after processing each measurement batch (iteration) for one trajectory. Bars and samples are coloured according to their likelihood with higher values associated with a yellowish hue. The red trace in the top of each histogram corresponds to the real value of the parameter. The red line in the second row depicts the true value of the parameter, and the purple regions highlighted in each image illustrates a 95% confidence interval.

based on this analysis. Another benefit of PGAS in this sense is the capability to work with non-linear and non gaussian distributions which may appear in practical situations.

To illustrate the previous discussion, Figures 4.9a and 4.9b show the approximations of the distributions of contact point velocities for the miniloader. The results only corresponds to the left side of the robot since the terrain simulated was uniform. However, in uneven soil surfaces, each wheel has to be assessed individually. Both figures show that generated samples (white dots) can effectively represent the cpv during calibration. Furthermore, as the robot drives and gets new information, the confidence region gets centred at the true value (red cross). This is an interesting outcome given the high variability observed in the evolution of the parameter means. Further analysis and development is certainly required to apply this finding in path planning, mobility prediction or terrain traversability assessment; however this work

provides a valuable starting point. It is worth to mention that although only one trajectory is analysed here, a similar behaviour was observed in the remaining trajectories. Moreover, the same analysis holds for the results regarding the pioneer robot, which are detailed in Appendix A.

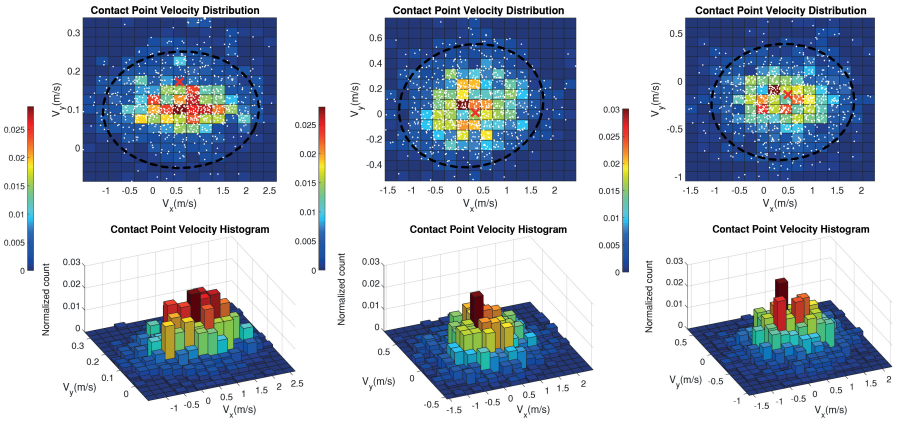

(A)

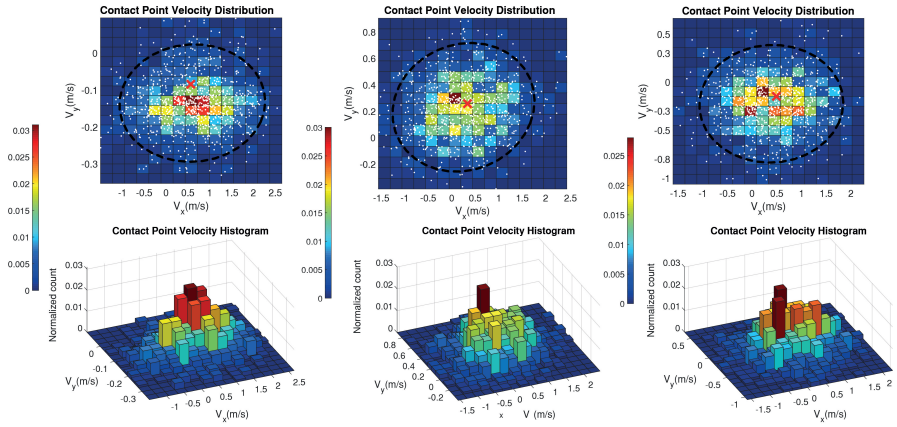

(B)

FIGURE 4.9: Approximations of the contact point velocities distributions for the front left (A) and back left (B) wheels of the miniloader in a single trajectory. Each column corresponds to the samples generated at the beginning, middle and ending of the trajectory, respectively. The dashed ellipse depicts a 90% confidence region and the red cross indicates the true values. The white dots correspond to samples generated during the calibration process. Bars and cells are coloured according to their normalized likelihood.

To compare the proposed approach with the integrated perturbation error dynamics, the parameter evolution is first analysed. Figure 4.10 shows the estimations provided by IPEM for all calibration trajectories. In general, all values converge rapidly for both robots, which was expected to some extent since IPEM was designed to identify static (constant) parameters. However, it is interesting to note that p_1, p_2 and p_3 are slightly biased, specially for the pioneer robot. Furthermore, the PGAS results showed the same behaviour of that parameters for the same robot. This outcome implies that the identification performance may be related with i) the size and weight

of the robot or ii) the speed at which they were driven. Thus, from these results, it can be inferred that the robot's inertial characteristics and speed affect the calibration performance.

At this point it is also important to note the higher variability in the sample means of the PGAS with respect to IPEM estimations. Since the sampler in the PGAS was free to generate draws from the posteriors within the interval $[-2, 2]$, parameters were not constrained to be constant. In this ideal test case, this is clearly a disadvantage since stationariness in the parameter evolution is desired. However, in real cases were terrain characteristics can change rapidly while the robot is driving, this variability is a desired feature.

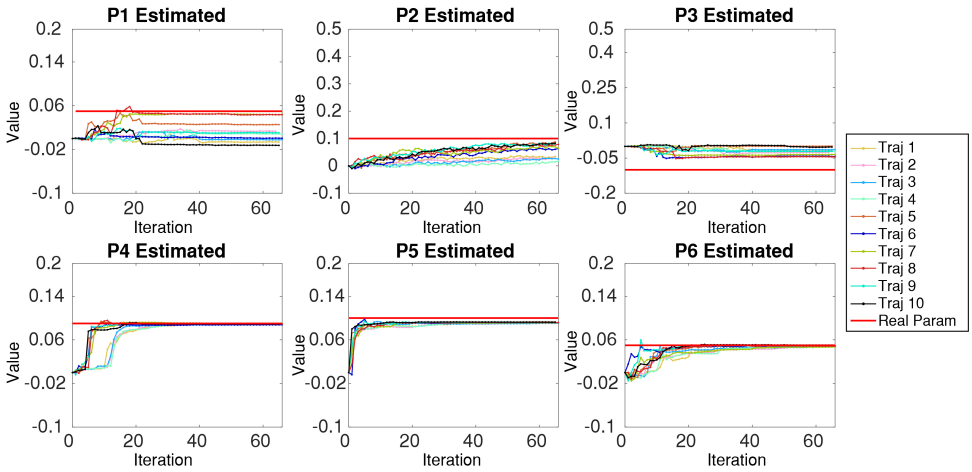

(A)

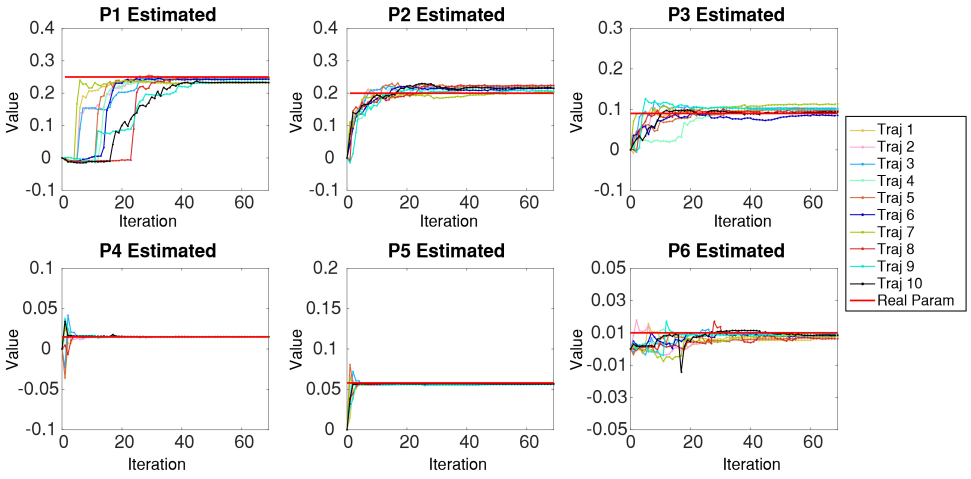

(B)

FIGURE 4.10: Parameter estimations using the IPEM methodology for the pioneer (A) and the miniloader CAT262c (B). Results corresponds to the same calibration trajectories presented in Fig.4.7.

Numerically assessing the accuracy on the parameter estimation itself is an option, but it is more interesting to evaluate the accuracy in the estimated robot positioning, instead. This is, how well the model is capable to predict the robot state with the parameters estimated with both methods. To this aim, after processing each

measurement batch, the final position of the robot was estimated using the parameters learned along with an EKF and Particle Filter for the IPEM and PGAS methods, respectively. In addition, the uncalibrated model was also considered by setting all parameters to zero and running a positioning EKF. Figure 4.11 depicts the statistical behaviour of the residuals for the robot pose before and after calibration. Residuals were calculated as the difference between the true robot position and orientation with their estimated values. For simplicity, only a 2D positioning is considered, but these results can be extended for a three dimensional case. At this point, only data for the miniloader is presented, and results regarding the pioneer are detailed in Apendix A. In general, the residuals are close to zero when using calibrated parameters with the IPEM and the PGAS methodologies, for all trajectories. However, as the IPEM approach produced parameter estimations converging rapidly to the true values, its residuals show a bounded tendency closer to zero. Additionally, both approaches show similar interquartile ranges that considerably outperforms the uncalibrated results. It is also interesting to note the high amount of outliers in the IPEM method, probably produced by the variability of the parameter estimates at the first iterations.

To get a deep insight about the total error obtained, Tables 4.6 and 4.7 summarize the accumulated mean squared errors (MSE) of the miniloader positioning. In this case, the superior performance of the IPEM approach is more evident. This outcome is certainly produced by the rapid convergence of the parameter estimates, as noted previously. Appendix A details this results for the pioneer robot.

TABLE 4.6: Accumulated mean squared error of the robot position for the 10 trajectories

Traj.	Pose MSE [m]				
	Uncalibrated	Calibrated IPEM	% Improvement	Calibrated PGAS	% Improvement
1	3.076	0.778	74.713	1.603	47.880
2	3.742	0.819	78.115	1.561	58.278
3	2.678	1.027	61.627	1.379	48.482
4	2.775	0.823	70.338	1.690	39.105
5	3.338	1.167	65.049	1.596	52.180
6	3.596	1.010	71.909	1.582	55.998
7	3.504	1.185	66.176	1.522	56.578
8	3.247	0.982	69.762	1.354	58.317
9	2.584	1.096	57.573	1.458	43.588
10	3.549	0.788	77.807	1.299	63.406

TABLE 4.7: Accumulated mean squared error of the robot orientation for the 10 trajectories

Traj.	Attitude MSE [deg]				
	Uncalibrated	Calibrated IPEM	% Improvement	Calibrated PGAS	% Improvement
1	27.115	0.458	98.312	0.617	97.726
2	29.153	0.374	98.716	0.373	98.721
3	21.339	0.244	98.856	0.481	97.744
4	24.733	0.420	98.301	0.620	97.492
5	25.606	0.597	97.670	0.525	97.950
6	31.463	0.607	98.071	0.485	98.457
7	25.245	0.256	98.987	0.452	98.209
8	27.576	0.257	99.067	0.483	98.248
9	23.413	0.222	99.051	0.503	97.854
10	30.792	0.659	97.861	0.529	98.282

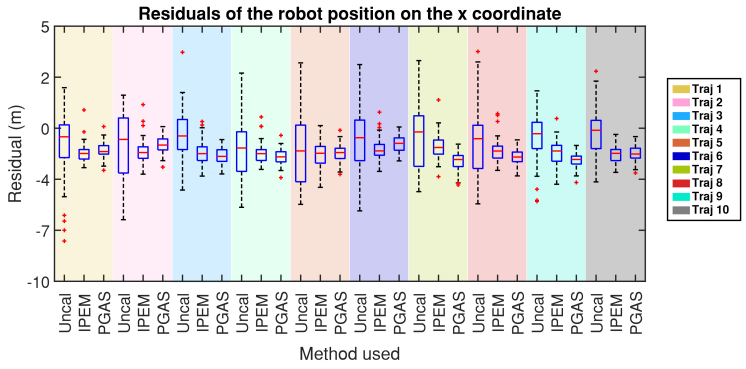

(A)

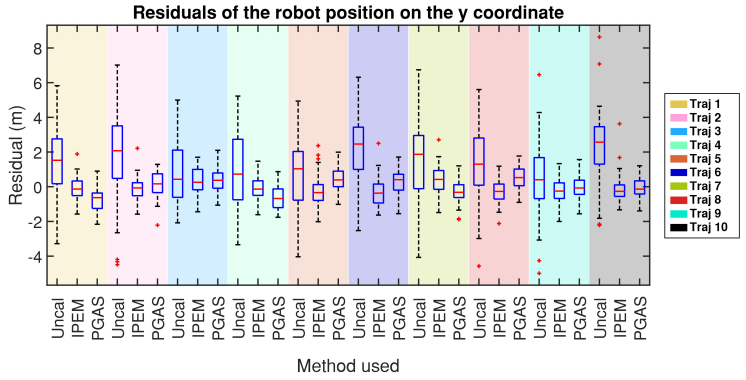

(B)

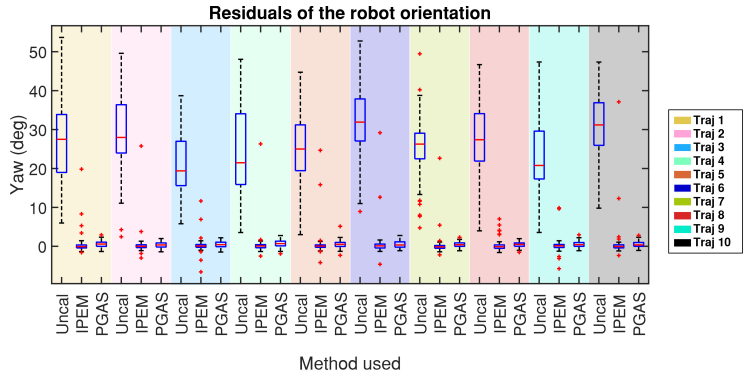

(C)

FIGURE 4.11: Boxplots of the residuals for the 2D position of the miniloader in 10 trajectories. Coordinates x (A), y (B) and the robot attitude (C) are depicted. IPEM and PGAS methods outperformed the uncalibrated positioning, with a better performance of IPEM.

4.6.2 Multiple Terrains

In real off road scenarios, it is common to observe diverse and mixed terrain types, which affect the vehicle slippage behaviour and thus the parametrization of its model. Furthermore, even in the same terrain type, factors like soil cohesion and humidity also affect the robots mobility (Wong, 2010). For this reason, the proposed identification algorithm was also tested varying the model parameters to simulate terrain changes. Given the characteristics of the simulator, at a specific time interval Δt (in simulation

time), five parameter sets were established for each robot. Table 4.8, list the values employed. For these changes to have enough representativeness in the robot movement (and thus in the parameter observability), Δt is function of the robot maximum speed and its dimensions. Thus, $\Delta t = 1.4s$ for the Pioneer, and $\Delta t = 2s$ for the miniloader. Additionally, the length of the travelled distance to get a measurement batch was set to $\Delta s = 10m$ and $\Delta s = 15m$ for the pioneer and the miniloader, respectively. As mentioned before, these values are in the limits that ensured that each data batch provide enough information (given the variability of the terrains) to run the identification algorithm for each robot. Finally, all the remaining parameters about the PGAS method were not changed from the previous setup.

TABLE 4.8: Parameter values used to simulate various terrains for the pioneer and the miniloader

	Pioneer 3AT					CAT 262c				
Params	Case 1(P^1)	Case 2(P^2)	Case 3(P^3)	Case 4(P^4)	Case 5(P^5)	Case 1(P^1)	Case 2(P^2)	Case 3(P^3)	Case 4(P^4)	Case 5(P^5)
p_1	0.07	-0.5	0.74	0.03	-0.57	0.1	0.07	0.5	0.001	0.25
p_2	0.5	0.02	0.22	0.089	0.44	0.0255	0.03	0.09	0.09	0.2
p_3	-0.3	-0.65	-0.058	-0.73	-0.9	-0.03	-0.3	0.03	0.3	0.09
p_4	-0.88	0.88	0.08	-0.13	-0.69	-0.02	-0.4	-0.02	0.2	0.5
p_5	0.01	0.1	0.5	-0.2	0.58	0.1	0.01	0.1	0.09	0.058
p_6	0.5	0.05	0.52	0.44	0.12	0.5	0.1	0.08	0.9	0.01

Similarly to the previous test case, 10 trajectories for each robot were simulated. At this point, only plain terrain was considered, with the objective to agree with experimental field tests (detailed in the next Section). In that case, only flat surfaces were available to drive with the heavy miniloader. This election comes at the cost that some of the parameters will be unobservable. As Fig. 4.12 shows, p_1 could not be correctly identified for either of the two robots. An interesting point to note here is p_3 and p_4 are also parameters dependent on gravtity, however, these results suggest that their dependency is stronger with lateral forces experienced by the vehicles, specially for the miniloader. In fact, this evolution of means indicates that the PGAS algorithm was not capable of calibrate the model for the pioneer. Only sample means of p_5 follow the real values, in contrast with the miniloder, where sample means p_2, p_3, p_4 and p_5 show a good tendency. Additionally, the variability observed in estimations for p_6 in single terrain tests is more critical here. Changing the covariance of the random walk Λ may attenuate this effect.

The evolution of the sample populations approximating the posterior for one trajectory of the miniloader is shown in Figure 4.13a. In this case is more evident the capability of PGAS for adapting to changes in the parameter values (and therefore the terrain characteristics). All the populations (not including p_1) shows a tendency for moving to regions were the real parameters are probable. Unobservability of p_1 is now more evident since the samples from the posterior distributions are roughly uniform in the interval $[-2, 2]$. This implies that any information about p_1 was available in the measurements, and therefore the best estimate of the posterior is an uniform distribution (the prior). Similarly, samples from p_6 are scattered in the same interval, but the regions of higher likelihood are less wide. This outcome indicates estimations with a better confidence, but they still can not follow the parameter change in a proper way. Considering also the results of the single terrain tests, it can be concluded that p_6 is particularly difficult to identify in this model. In fact, a close look of the parametrization reveals a possible reason for this issue. The sixth parameter is related with the angular velocity of the robot ω_z (see Eq. 4.40), whose magnitude is

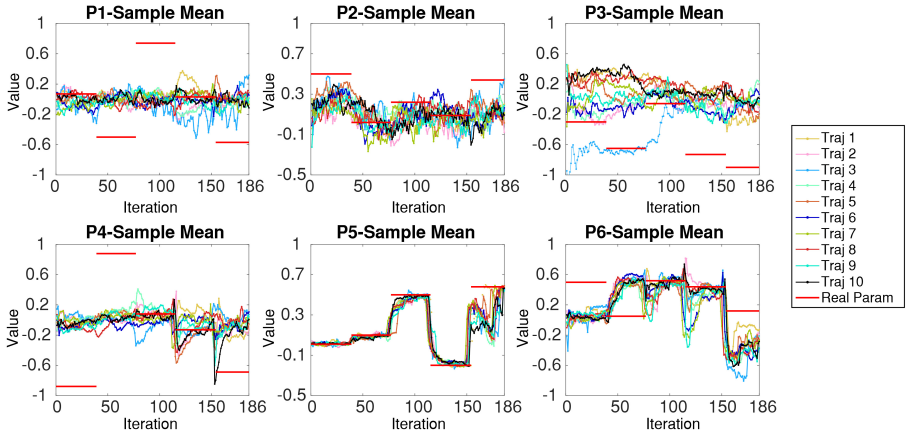

(A)

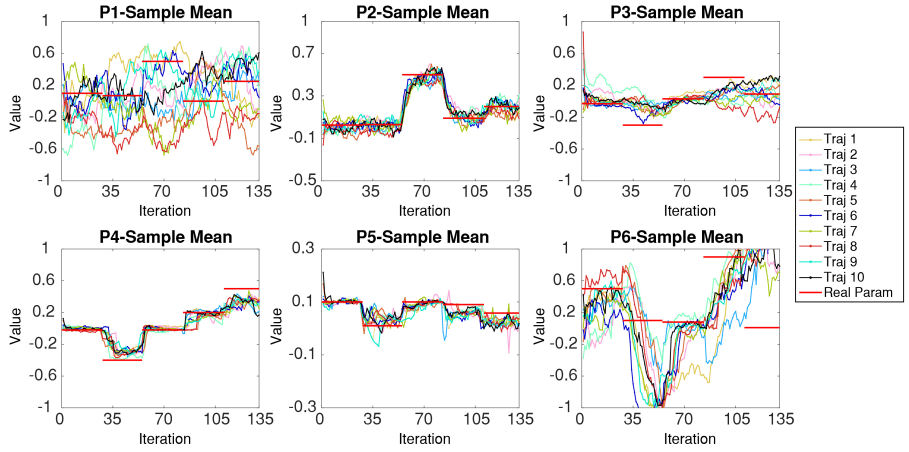

(B)

FIGURE 4.12: Evolution of the sample means of the parameters for the Pioneer 3AT (A) and the miniloader CAT262c (B). A total of 10 calibration trials changing 5 different parameter sets were simulated. Unobservability of parameters related with gravity terms is clear.

smaller than the other terms. Thus, the effect of p_6 would be "faded" at some extent. However, this drawback is not highly critical in the robot movement analysis for the same reason.

Histograms and sample evolution regarding the pioneer robot are detailed in Appendix B. However, it is important to note here that in agreement with the means evolutions, the posterior distributions are not correctly estimated for this robot for any other parameter than p_5. Therefore, the robot speed and inertial characteristics indeed have an impact in the identification of this slippage model. This issue was confirmed when analysing the results of the IPEM algorithm, as will be shown later.

The samples generated for the miniloader also exhibit a proper characterization of the contact point velocities. Figures 4.14 and 4.14 show distributions of the front and rear wheels cpv at each terrain transition (i.e., just before the parameters changed its value), and at the end of the trajectory. As can be noted, the true cpv lies in the 90% confidence region of the approximated distribution. This result indicates that the samples generated by the PGAS algorithm can correctly characterize the randomness

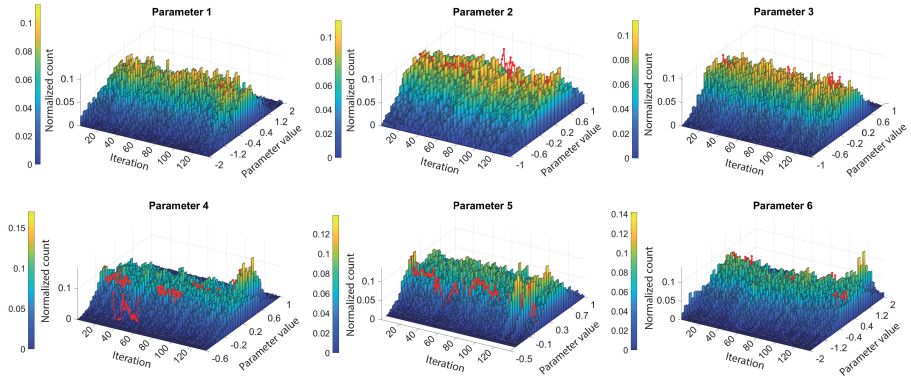

(A)

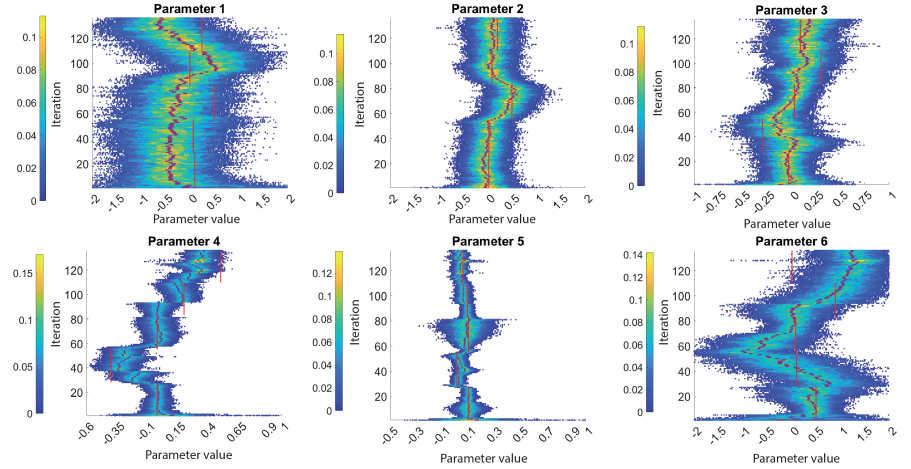

(B)

FIGURE 4.13: Evolution of the histograms (A) and sample population (B) generated after processing each measurement batch (iteration) for one trajectory. Bars and samples are coloured according to their likelihood with higher values associated with a yellowish hue. The red trace in the top of each histogram corresponds to the real value of the parameter. The red line in the second row depicts the true value of the parameter, and the purple regions highlighted in each image illustrates a 95% confidence interval.

of the cpv when traversing heterogenous terrains. With this observation in hand, a probabilistic assessment of the robot mobility of terrain traversability can also be performed in such changing terrains, which is a more realistic scenario than only navigating on terrains with the same characteristics, specially in off-road scenarios.

In accordance with the other results for the pioneer robot in heterogeneous terrains, their cpv were not correctly characterized. For any of the test trajectories or the robot wheels, the true values were located within the 90% confidence region or even in the space spanned by the generated samples. The corresponding figures for this vehicle are depicted in Appendix B.

When comparing the PGAS and IPEM approaches, the latter shows a lower performance since it is not capable of account for the parameter variation in any of the testing robots, as shown in Fig. 4.16. Moreover, as by construction the parameter

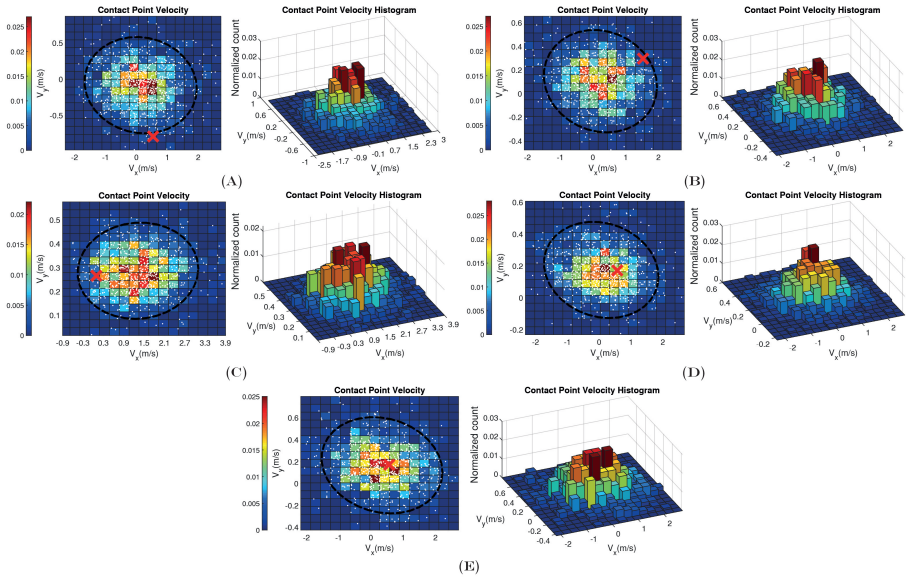

FIGURE 4.14: Approximations of the contact point velocities distributions for the front left wheel of the miniloader during transitions $P^1 - P^2$(A), $P^2 - P^3$(B), $P^3 - P^4$(C), $P^4 - P^5$(D) and at the end of the trajectory (E). The dashed ellipse depicts a 90% confidence region and the red cross indicates the true velocities. The white dots correspond to samples generated during the calibration process. Bars and cells are coloured according to their normalized likelihood.

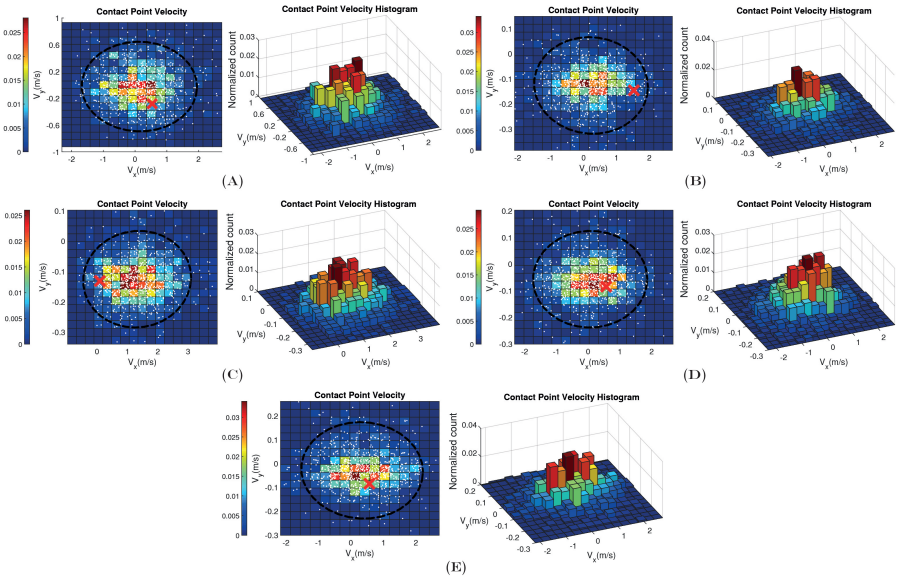

FIGURE 4.15: Approximations of the contact point velocities distributions for the rear left wheel of the miniloader during transitions $P^1 - P^2$(A), $P^2 - P^3$(B), $P^3 - P^4$(C), $P^4 - P^5$(D) and at the end of the trajectory (E). The dashed ellipse depicts a 90% confidence region and the red cross indicates the true velocities. The white dots correspond to samples generated during the calibration process. Bars and cells are coloured according to their normalized likelihood.

estimates are forced to have only slight changes, all of them were fairly constant throughout the calibration procedure. Furthermore, evolution of estimates are similar for all calibration trajectories, which indicates that independently of the path followed by the robot, the parameters will not be identifiable.

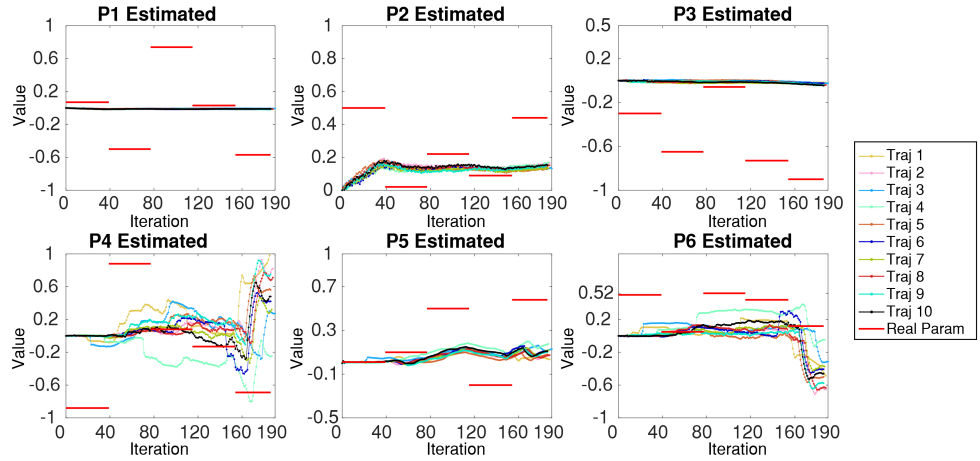

(A)

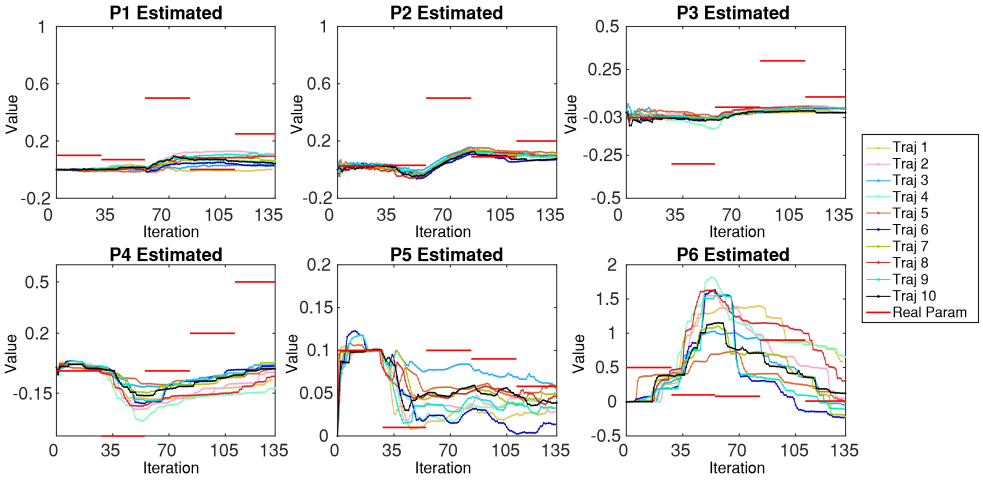

(B)

FIGURE 4.16: Parameter estimations using the IPEM methodology for the pioneer (A) and the miniloader CAT262c (B). Results corresponds to the same calibration trajectories presented in Fig.4.12.

Given the model was not properly calibrated, it could be expected to get a poor mobility prediction in this case. This conjecture is particularly true for the miniloader, as Fig. 4.17 shows. Residuals in the x and y robot position using parameters calibrated with PGAS present an improvement with respect to IPEM and the uncalibrated approaches. Furthermore, this improvement is more evident in the robot attitude prediction. Residuals in this case are nearer to zero, with low amount of outliers, which also indicates a higher precision. This outcome also confirms the conclusion that the employed model is not deeply sensitive to changes in p_6.

In contrast, the better performance of PGAS was not observed for the pioneer. In fact, the uncalibrated model showed the best prediction capabilities. As parameters

estimates in the IPEM approach were almost constant, results of these methods were fairly similar. The PGAS method, on the other hand, produced the worst position prediction for this robot. In this case, it is clear that variability in the parameters seriously affects the robot state in the model employed. This fact makes sense given the sampling scheme employed in the PGAS. As the state is sampled conditionally on the parameters and vice versa, a bad drawn of the parameters will produce an incorrect state estimate. In the next iterations this sequence degenerates the model calibration providing the poor results observed in both the parameter posterior approximation and the robot state prediction. It is important to highlight that this issue only appears in the pioneer robot, which clearly supports the conclusion that weight, size and speeds of the robots affect the identification of this model. The corresponding results that illustrates this discussion are shown in Appendix B.

Accumulated errors for the miniloader in all the trajectories are summarized in Tables 4.9 and 4.10. The better performance of the PGAS approach for this robot is more visible here. In general, it outperforms the position and attitude estimations of IPEM and the uncalibrated model. This results show that variability on the parameters (and therefore the terrain characteristics) was correctly accounted by the proposed methodology. Furthermore, as noted before, the variability in the estimations of p_1 and p_6 was not critical in the robot motion estimation. Recall that p_1 does not have any effect when driving on flat surfaces, whereas p_6 was associated with the angular velocity of the robot (which is a smaller magnitude when compared with other terms in the parametrization). In contrast, accumulated errors for the pioneer robot (detailed in Appendix B) shows a poor performance of PGAS, which agrees with the previous results for that robot.

TABLE 4.9: Accumulated mean squared error of the miniloader position for 10 calibration trajectories

Traj.	Pose MSE [m]				
	Uncalibrated	Calibrated IPEM	% Improvement	Calibrated PGAS	% Improvement
1	1.885	1.793	4.878	1.745	7.453
2	1.960	1.719	12.299	1.579	19.444
3	2.175	1.907	12.326	1.845	15.147
4	1.944	1.895	2.528	1.595	17.958
5	1.954	1.664	14.839	1.559	20.210
6	2.046	1.976	3.438	1.684	17.704
7	1.858	1.736	6.592	1.708	8.094
8	1.938	1.839	5.119	1.834	5.360
9	2.032	1.802	11.302	1.623	20.103
10	1.885	1.856	1.524	1.575	16.427

TABLE 4.10: Accumulated mean squared error of the miniloader orientation for 10 calibration trajectories

Traj.	Attitude MSE [deg]				
	Uncalibrated	Calibrated IPEM	% Improvement	Calibrated PGAS	% Improvement
1	10.204	-2.284	77.620	0.448	95.611
2	11.376	-7.131	37.317	0.634	94.431
3	16.674	-6.006	63.979	0.450	97.301
4	13.026	-0.124	99.050	0.569	95.635
5	16.907	-2.622	84.490	0.580	96.568
6	5.641	-6.285	-11.420	0.562	90.031
7	14.389	-3.311	76.988	0.439	96.949
8	14.521	-4.046	72.141	0.469	96.770
9	11.545	-3.456	70.066	0.633	94.521
10	11.009	-6.372	42.120	0.518	95.296

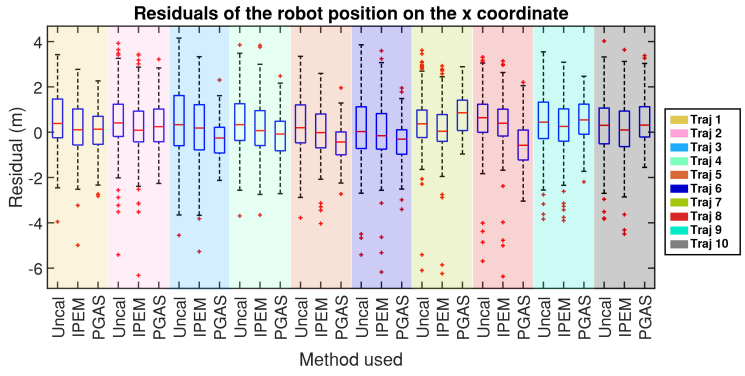

(A)

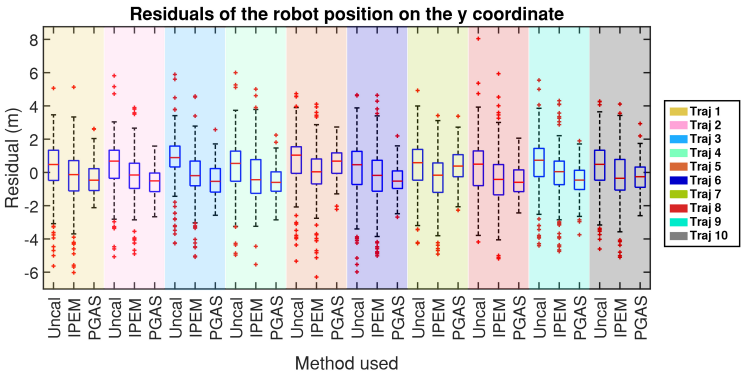

(B)

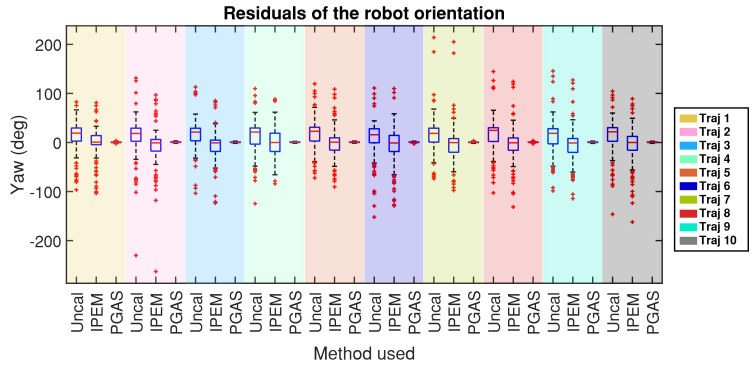

(C)

FIGURE 4.17: Boxplots of the residuals for the 2D position of the miniloader in 10 trajectories. Coordinates x (A), y (B) and the robot attitude (C) are depicted. IPEM and PGAS methods outperformed the uncalibrated positioning, with a better performance of PGAS.

Finally, it is important to note that in both simulation cases (single and multiple terrains), the current implementation of PGAS is off-line. Timing results produced a mean processing time of 3,5 hours for 5 minutes of simulated driving. This outcome is certainly an important drawback of the proposed methodology; however, the code can be further optimized to work in various cores of the processor. Furthermore, if available, the use of graphics processing units is also an optimization option.

4.7 Experimental Results

Given the simulation results, the field tests were only performed on the miniloader CAT262c. The technical details of the vehicle employed are detailed in Section 4.5. As only position and attitude measurements are required, the sensors employed at this point were global positioning receivers and an inertial measurement unit (IMU). For this work, this information was provided by the Vectornav® Vn-200. It is a miniature device that combines a GPS receiver with inertial sensors along with a Kalman filter processing to get accurate position and attitude estimations. It characteristics include a heading, and pitch/roll accuracies of 0.3^o and 0.1 RMS, respectively. Furthermore, the angular resolution is less than 0.05^o. The corresponding horizontal an vertical position accuracies are $2.5m$ and $5m$. In order to get the ground truth for these experiments, a RTK SwiftNav® Piksi V2 was used. It has $2cm$ accuracy when the base station and the rover stations have a fixed signal. The mounting of the sensors on the vehicle is shown in Fig. 4.18. All data was first logged using Robot Operating System (ROS) and then processed offline using a computer with a 2.60 Ghz Corei7 processor and 16GB of RAM.

FIGURE 4.18: Sensors employed in experimental tests. The IMU was located in the vehicle body. The GPS and RTK antennas were placed at its top.

The experimental tests were carried out in the Pontificia Universidad Católica de Chile, campus San Joaquín. It is located at $33^o30'00.3''$ S, $70^o36'35.3''$ W in the Metropolitan Region of Santiago, Chile. Due to operative issues, these tests were only conducted inside the campus, where terrains consisted mainly in pavement and gravel plain surfaces. Figure 4.19 depicts several snapshots of the testing place, including the terrain traversed at some points.

Regarding the PGAS methodology, the only change with respect to the simulation setup was the distance travelled to get a batch measurement. Considering that variability on the terrain was uncertain at some extent (soil compactness and humidity can change even in the same terrain type), a new batch was processing was performed when the miniloader travelled $10m$. As stated before, this distance was found to be the minimum at which the identification algorithm provided successful results in

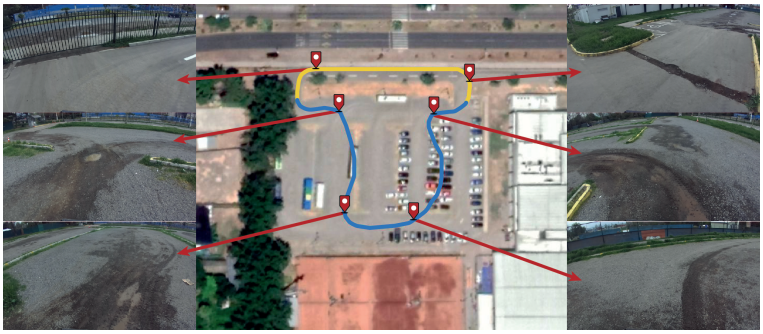

FIGURE 4.19: Location of the experimental tests: a parking lot with a mixture of gravel and pavement. The blue line denotes a gravel terrain, whereas the yellow line corresponds to paved surfaces.

multiple terrains. The remaining parameters and hyperpameter distributions were set identical to simulation.

Given the characteristics of the experimental location, tests consisted in driving with the vehicle ten times following approximately the same path. This election also allowed to test repeatability on the parameter and state estimates. To assess the parameter estimations and the consequent robot motion estimations when including additional external uncertainties, two types of trials were performed: with the miniloader arm (including the bucket) static and with the miniloader arm constantly moving. Figure 4.20 shows the evolution of the sample means obtained with the PGAS methodology throughout the calibration trajectories for both cases. In general, all the means have a similar tendency for all the identifiable parameters (as the terrain was flat, p_1 was not observable). Considering that p_3 also showed a high variability in the simulation tests, these results can be considered as satisfactory estimations of the parameters. It also has to be noted that parameter means do not show considerable changes in the terrain transitions. However, their variability increases at some extent when traversing the gravel terrain. This outcome makes sense since gravel is looser than pavement, which increases the possibility of experience diverse slippage situations even in the same terrain type.

As the effects of the arm movement in the miniloader are not appreciable analysing the sample means (they show similar evolutions over the iterations), the sample populations provide a better insight of this point. Figure 4.21 shows the samples approximating the parameter posterior after each batch estimation. It can be noted that spreading on the approximated posterior is wider when the arm was moving. This outcome indicates that uncertainty in the robot motion would also be higher in this case, as will be demonstrated later.

Regarding the contact point velocities, Fig. 4.22 shows the samples generated to approximate their distributions. Similarly to the parameter estimations, the results corresponding to the moving arm test case are more spread, indicating a higher uncertainty in the characterization of the cpv. It is then inferred that these samples indeed capture the variability of the contact point velocities produced due to the arm movement. Regarding the terrain transitions, it is certainly required to evaluate the evolutions of these samples through all the trajectory to get a profiling of these cpv. With this outcome and an estimation or measurement of the vehicle's velocity, it could be also possible to characterize the wheel slippage in a similar way. While

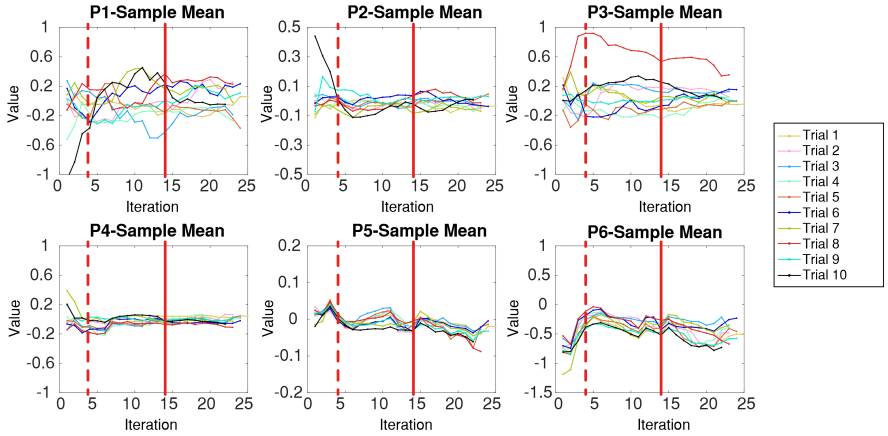

(A)

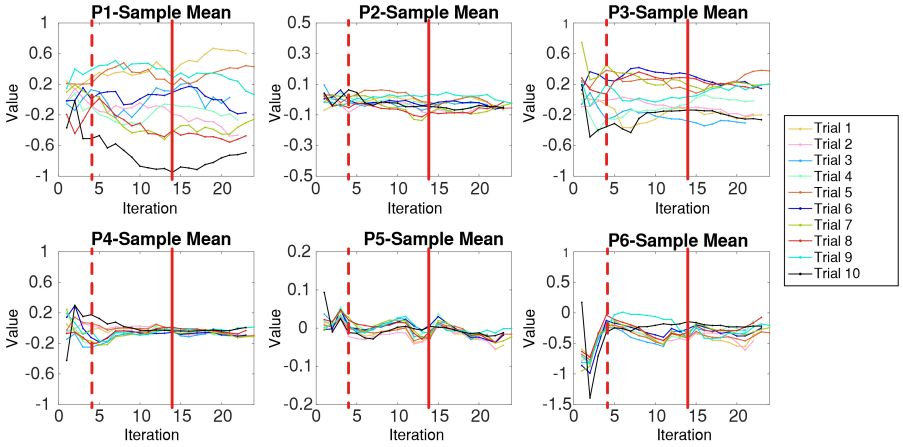

(B)

FIGURE 4.20: Evolution of the sample means of the six parameters for the miniloader with the arm static (A) and in movement (B). A total of 10 trials following the same path were performed. The dashed and solid red lines show the terrain changes from gravel to pavement and pavement to gravel, respectively.

only the front and rear left wheels are analysed here, the others showed similar results (considering that only plain terrain was traversed).

In order to compare the PGAS estimates with the IPEM results, the same approach followed in the simulation was adopted. The parameter estimates obtained with the IPEM methodology are shown in Fig. 4.23. It can be seen that parameters are fairly constant, at contrast with the PGAS means. Furthermore, the effects of driving in different terrains are not appreciable, as also observed in Section 4.6.2. A comparison between the estimates obtained when the arm was static and when it was in movement also does not show any difference at this point.

In this case, the residuals are computed with respect to the RTK and the IMU yaw angle readings. Figures 4.24 and 4.25 show the boxplots the residuals for both test cases. In general, the robot motion was better estimated with parameters sampled using the PGAS methodology, with a slight decreasing in performance for tests where the arm was moving. This outcome is reasonable since other parameters than those identified with PGAS or IPEM also changed (e.g., *COM* or body inertia). It also

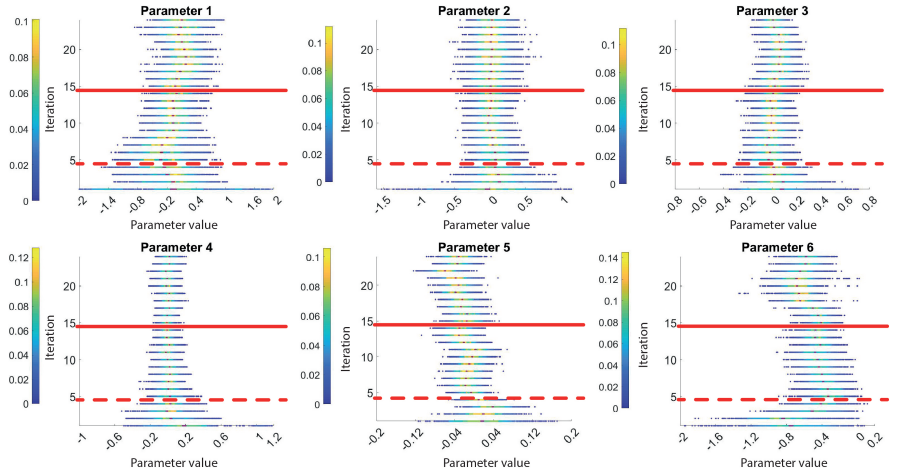

(A)

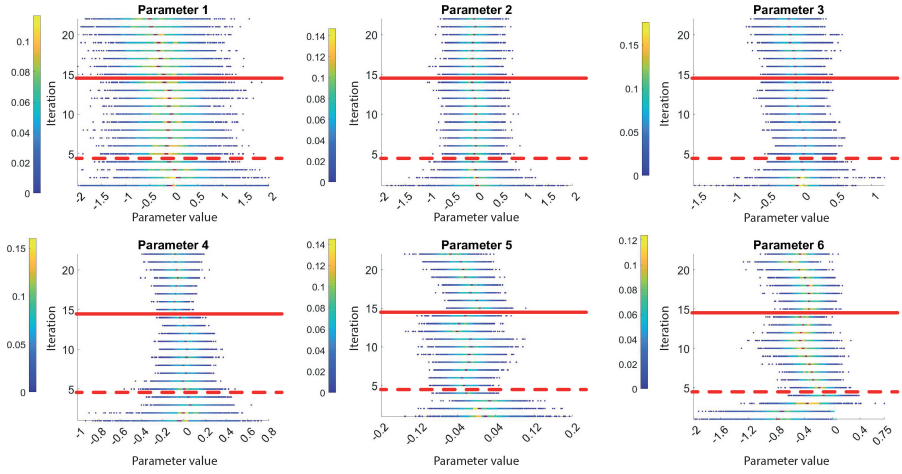

(B)

FIGURE 4.21: Evolution of the sample populations generated after processing each measurement batch (iteration) in one trajectory for tests with the arm static (A) and in movement (B). Bars and samples are coloured according to their likelihood with higher values associated with a yellowish hue. The dashed and solid red lines depict terrain changes from gravel to pavement and pavement to gravel, respectively.

can be noted that robot orientation shows a particular improvement for the PGAS methodology, which agrees with the results observed in simulation.

Finally, Tables 4.11, 4.12, 4.11, 4.14 summarize the accumulated errors during the trajectory for the 10 trials for both test cases. Following the insights given by the residual boxplots, a better performance is obtained when calibrating the model with the PGAS methodology. Thus, variability of the parameters provided by PGAS can indeed account for the effects of terrain characteristics in the robot motion prediction. Special mention has to be done with respect to the attitude MSE in the first trial with the arm moving. The anomalous error obtained there is produced by the outlier showed in the corresponding residual boxplot. This is certainly consequence of an artefact in the measured yaw angle.

As noted in the end of the simulation tests, the processing time was also high in

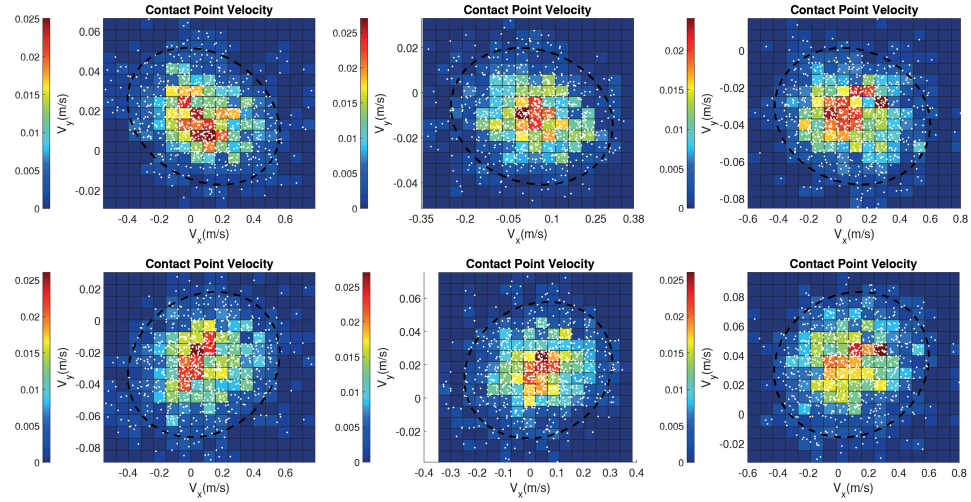

(A)

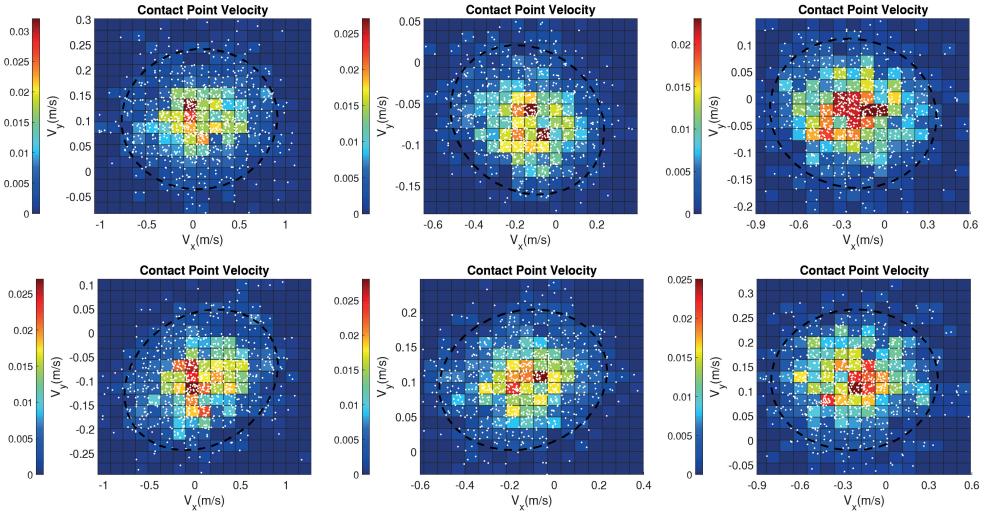

(B)

FIGURE 4.22: Approximations of the contact point velocities distributions left wheels of the miniloader in a single trajectory, when the arm was static (A) and moving (B). Rows correspond to front and rear wheels for each case, whereas columns show the samples generated at the beginning, middle and ending of the trajectory, respectively. The dashed ellipse depicts a 90% confidence region. The white dots correspond to samples generated during the calibration process. Bars and cells are coloured according to their normalized likelihood.

this case. A mean of 3 hours for processing each trial was required. Considering that the vehicle was driven for 5 minutes approximately, the computational burden is confirmed to be the main drawback of the algorithm implementation.

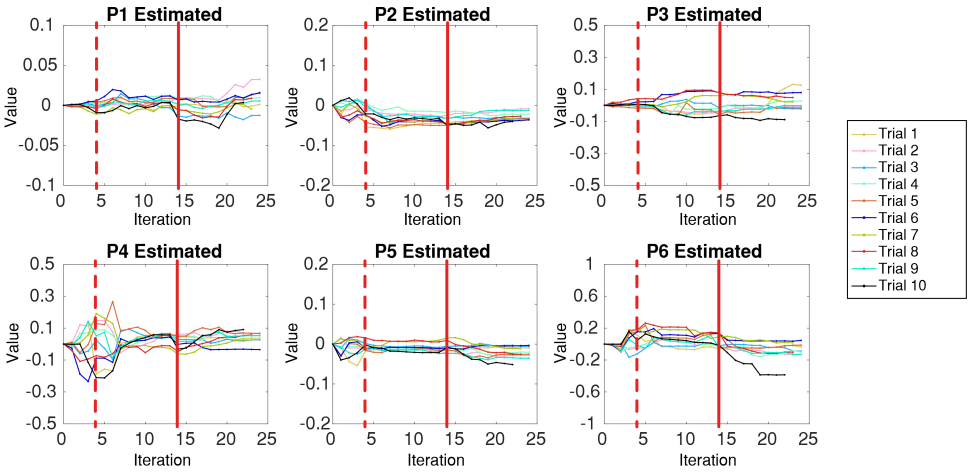

(A)

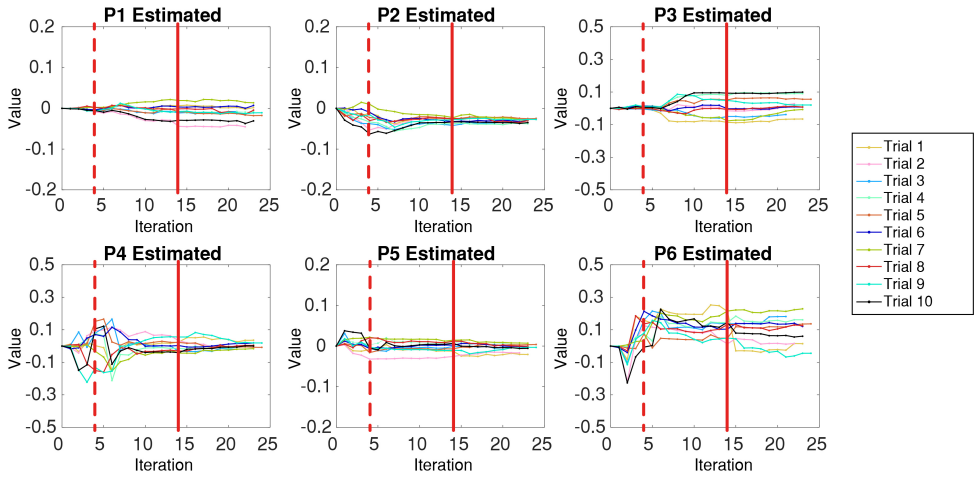

(B)

FIGURE 4.23: Parameter estimations using the IPEM methodology miniloader with the arm static (A) and in movement (B). Results corresponds to the same calibration trajectories presented in Fig.4.12. The dashed and solid red lines show the terrain changes from gravel to pavement and pavement to gravel, respectively.

4.8 Contributions

The material presented in this Chapter studied and implemented a methodology for probabilistic identification of a non-zero slippage model for a skid steer robot. At contrary to classic approaches, the proposed method enabled the assessment of the parameter posteriors and their evolution trough all the calibration trajectory. Furthermore, it was interesting and promising to observe that the samples generated also allowed to characterize the distributions of the wheels contact point velocities. Precisely, this point is one of the major contributions of the Chapter since it would enable to also characterize wheel slip as a random variable and consequently perform a probabilistic assessment of the mobility status of the robot in a given terrain. Additionally, the comparison between the IPEM approach and PGAS showed that the latter has a better performance in heterogeneous terrains, which is also an important

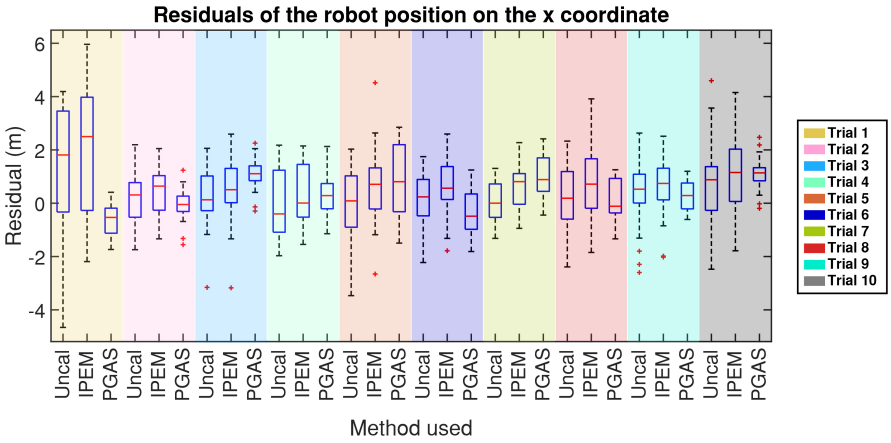

(A)

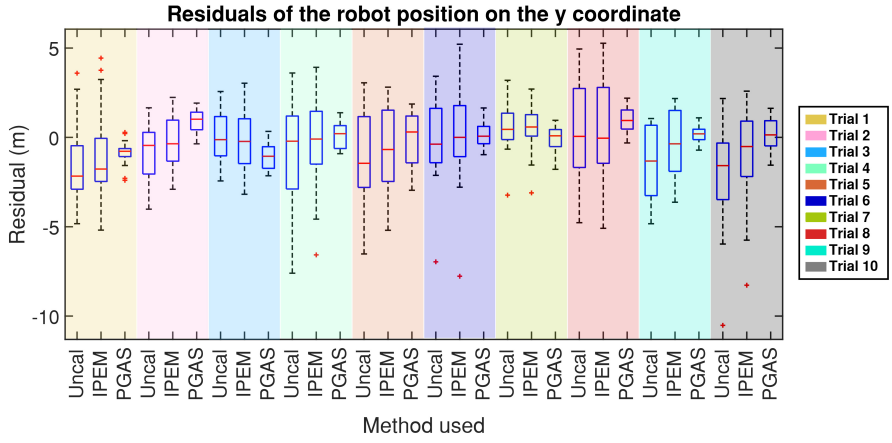

(B)

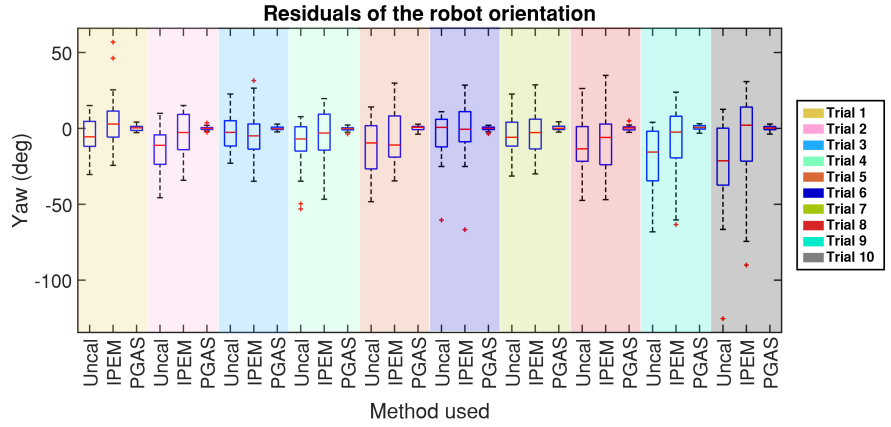

(C)

FIGURE 4.24: Boxplots of the residuals for the 2D position of the miniloader in the 10 trials with the arm static. Coordinates x (A), y (B) and the robot attitude (C) are depicted. IPEM and PGAS methods outperformed the uncalibrated positioning, with a better performance of PGAS.

outcome from the simulation and field tests presented in this Chapter.

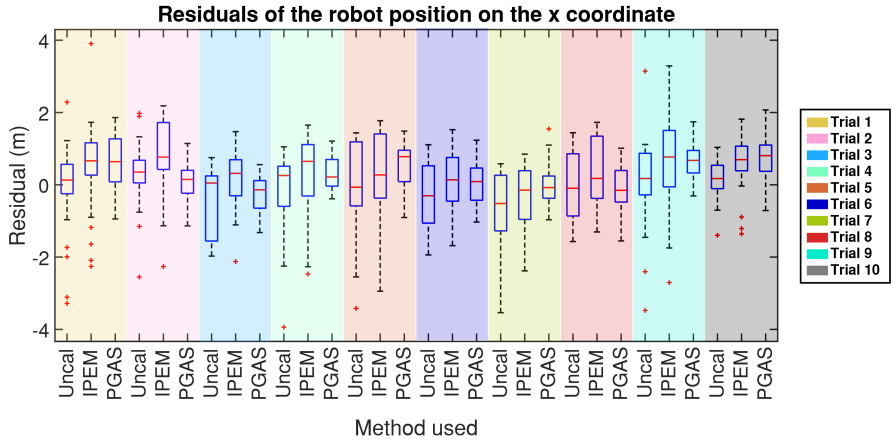

(A)

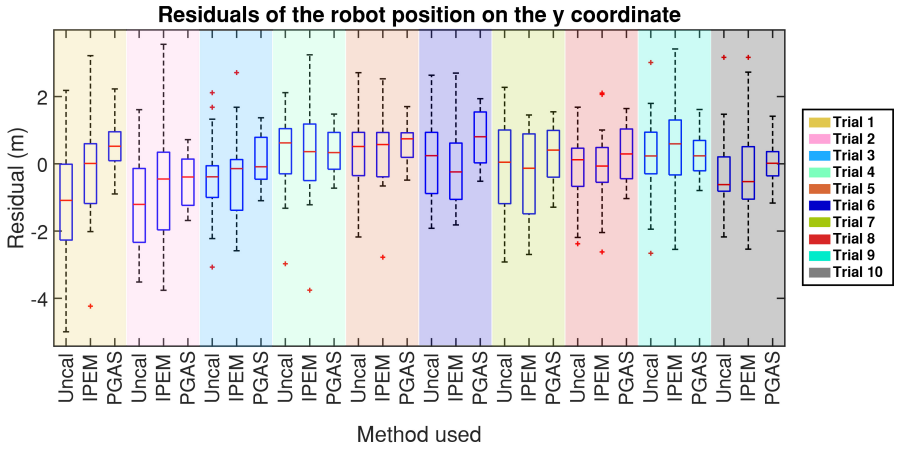

(B)

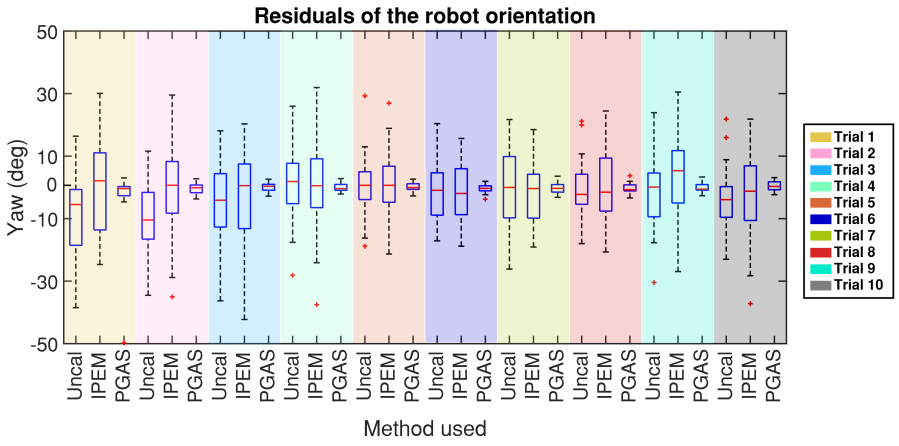

(C)

FIGURE 4.25: Boxplots of the residuals for the 2D position of the miniloader in the 10 trials with the arm in movement. Coordinates x (A), y (B) and the robot attitude (C) are depicted. IPEM and PGAS methods outperformed the uncalibrated positioning, with a better performance of PGAS.

TABLE 4.11: Accumulated mean squared error of the miniloader position for 10 trials with the arm static

Trial	Pose MSE [m]				
	Uncalibrated	Calibrated IPEM	% Improvement	Calibrated PGAS	% Improvement
1	3.591	3.786	-5.414	1.193	66.772
2	1.750	1.593	9.022	1.179	32.623
3	1.536	1.875	-22.038	1.629	-6.010
4	2.591	2.392	7.698	1.055	59.279
5	2.704	2.593	4.118	2.051	24.171
6	1.957	2.149	-9.788	1.014	48.181
7	1.290	1.569	-21.685	1.287	0.242
8	2.740	2.730	0.356	1.304	52.403
9	2.250	2.076	7.757	0.716	68.183
10	3.023	2.683	11.242	1.454	51.921

TABLE 4.12: Accumulated mean squared error of the miniloader orientation for 10 trials with the arm static

Trial	Attitude MSE [deg]				
	Uncalibrated	Calibrated IPEM	% Improvement	Calibrated PGAS	% Improvement
1	10.027	13.354	-33.178	1.439	85.649
2	15.112	11.902	21.243	0.919	93.922
3	9.340	11.352	-21.547	0.993	89.367
4	13.169	13.290	-0.921	1.013	92.306
5	16.556	17.783	-7.407	1.438	91.316
6	11.338	13.282	-17.144	1.032	90.897
7	10.452	11.615	-11.123	1.277	87.780
8	17.890	16.665	6.845	1.311	92.672
9	20.317	16.431	19.125	1.275	93.725
10	28.396	22.758	19.856	1.352	95.240

TABLE 4.13: Accumulated mean squared error of the miniloader position for 10 trials with the arm in movement

Trial	Pose MSE [m]				
	Uncalibrated	Calibrated IPEM	% Improvement	Calibrated PGAS	% Improvement
1	1.864	1.785	4.251	1.180	36.706
2	1.832	1.938	-5.826	0.918	49.863
3	1.336	1.402	-4.921	0.808	39.500
4	1.352	1.486	-9.932	0.842	37.750
5	1.370	1.454	-6.138	1.094	20.093
6	1.358	1.242	8.531	1.125	17.136
7	1.556	1.405	9.688	0.915	41.202
8	1.230	1.253	-1.867	0.976	20.688
9	1.431	1.753	-22.572	0.953	33.401
10	1.057	1.499	-41.870	1.021	3.394

TABLE 4.14: Accumulated mean squared error of the miniloader orientation for 10 trials with the arm in movement

Trial	Attitude MSE [deg]				
	Uncalibrated	Calibrated IPEM	% Improvement	Calibrated PGAS	% Improvement
1	13.211	13.878	-5.044	17.185	-30.078
2	12.038	11.297	6.156	1.456	87.909
3	11.082	13.124	-18.429	1.203	89.145
4	8.906	9.980	-12.053	1.084	87.825
5	7.124	8.472	-18.912	1.066	85.031
6	7.283	7.644	-4.952	1.064	85.394
7	10.196	8.951	12.209	1.429	85.984
8	7.596	8.785	-15.662	1.310	82.754
9	8.499	11.659	-37.192	1.155	86.414
10	8.244	11.036	-33.862	1.355	83.565

The resulting article for this work is about to be sent for review and publication in an ISI journal.

Chapter 5

Conclusions

This Chapter summarizes the main conclusions and contributions of this Thesis, and identifies the work to be developed for extending the research presented here.

5.1 Contributions and Results

This work provided a thorough analysis and several applications of robotic perception for phenotyping and autonomous navigation. The state of the art was first reviewed for both perspectives in order to analyse the best sensors for each one and to know how they can be employed in practical applications. Despite of this thesis was focused on the hardware and data processing, the use of the resultant information for agronomic assessment was also depicted, specially in Chapter 2. In this way, it was intended to highlight the tight relationship between the two areas (agricultural and robotics). To achieve this aim, two case studies that filled some gaps encountered in the literature, were developed. The first provided an implementation to on-line geometrically characterize fruit trees using a LiDAR and to estimate structural variables from them. Furthermore, various methods of volume estimation were assessed along with the effects in these estimates when only partial data is employed. It was found that partially scanning the groves does not have a significant impact in the accuracy, which is an interesting outcome that could serve to optimize the overall measurement time. The second test case presented a sensor fusion application to get a geometric and thermal characterization of trees. In this case, the agronomic implications are more marked since temperature of the leaves provides a physiological insight of the tree water status. Laboratory and field tests allowed to validate the proposed system as a novel tool to assess the health status of an orchard.

The robotics perspective of this thesis was bounded to analyse the terrain on which the robot is navigating and its effects on the robot movement. Then, descriptive and dynamic approaches were proposed. Descriptively characterizing the terrain consisted in performing a visual terrain classification. Among the other methodologies proposed in the state of the art for this application, the main contribution in this topic is the usage of a low cost sensor to get high accuracy classification rates (>85%) using a medium-size training dataset. Extensive experimental tests conducted in several terrains showed that appropriate raw data preprocessing and feature engineering provide robustness even when the illumination conditions change. While the labelling of a new sample was suitable for on-line classification when driving at low speeds, it can be further improved to work in any driving velocities.

A dynamic characterization of the terrain effects on the robot movement can be interpreted in several ways. Among them, this thesis proposed the identification of a state of the art kinematic model that accounts for non-zero wheel slippage. In contrast with classical approaches where parameters are deterministically estimated or with limiting assumptions such as linear models or Gaussian distributions, it was chosen to use sampling methods within the Particle Markov Chain Monte Carlo methods to get approximations of the posterior parameter distributions. This original point of view proved to offer extended capabilities of analysis, not only for the parameters but also for the uncertainty propagation to other variables of interest. Simulation tests showed that the employed parametrization was limited in some extent since some parameters had more effect than others in the robot motion. Furthermore, the identification performance was found to be highly dependent on the robot size and speed. Thus, large gravitational and inertial forces had to induce slip to get a proper calibration. For this reason, parameter estimates worked better when using the miniloader. The sampling scheme employed by the proposed identification method also allowed to obtain sample populations of the contact point velocities of the wheel. As consequence, it was shown that uncertainty in the parameter estimates can properly account for variability in these contact point velocities. This outcome is specially interesting since it enables the possibility to study wheel slip also as a random variable and perform a probabilistic traversability assessment. In addition, a comparison between the proposed approach with the IPEM methodology showed that the latter provides better results in homogeneous terrains, where parameters remain slightly constant. However, it was found that in changing terrains the PGAS identification provided a better performance. Given the simulation results, experimental tests were only conducted using a semi-automated miniloader. Several trials performed in various conditions in a heterogenous terrain, showed the capability of the proposed method to identify model parameters that correctly accounted for the robot slippage (and thus the robot positioning) in the testing trajectory. Finally, it is worth to mention that the current implementation of PGAS does not admit real time applications, which is its main drawback. Given PGAS is a Monte Carlo method, it suffers of the known computational issues of those methods.

5.2 Further Work

Despite of achieving acceptable results in the applications developed, there are certain points to be further improved to extend this research. The first of the agricultural case studies can be extended to analyse also the effect of the vehicle travelling speed used to acquire data. Since the objective was to improve the efficiency of the overall scanning task, it is an important factor that also have to be taken into account. With respect to the 3D and thermal characterization, the static mounting designed for this work is a limiting aspect. It is necessary to improve the design to place the sensing system on a mobile robot. In addition, the use of an IMU instead of the potentiometer is a necessary change to improve the fusion results.

Regarding the terrain classification, the proposed methodology can be extended by using other machine learning algorithms which have proven to produce excellent results (e.g., convolutional neural networks). However, to implement them it is

required to extend the training dataset. Additionally, the labelling time has to be improved in order to use the terrain classifier at different driving velocities.

With respect to the calibration methodology employed in this work, the first point to improve is the processing time. To fully exploit its capabilities and potential for mobility assessment, an efficient computational implementation is required. As simulation and experimental tests demonstrated, the samples generated can be used to characterize the contact point velocities. With an estimation or measurement of the robot velocity, wheel slippage can be further described in a similar way. Therefore, a probabilistic terrain traversability assessment can be enabled. Given the results obtained with the kinematic model, designing a PGAS sampler to estimate parameters of dynamical models might be also possible. Finally, integrating both applications of terrain characterization is a necessary step. In that way, the robot would be capable to associate how the terrain "looks" and what are its effects of the robot mobility. This junction will further provide the robot with prediction capabilities to evaluate its mobility on the upcoming terrain in an integral manner.

Appendix A

Simulation Results for the Pioneer 3AT Robot - Single Terrain

This Appendix summarizes the results for the pioneer robot when simulating a single terrain. As commented in Section 4.6.1 of Chapter 4, evolutions of samples generated by the PGAS algorithm shows that parameters are correctly identified. The true values remain in regions of high probability as shown in Fig. A.1. It can also be noted that samples population are more scattered in the interval $[-1, 1]$, which indicates that model identification for this robot was particularly rough. A similar behaviour was observed in the other trajectories. However, as concluded at the end of the simulation Section, the variability on the model parameters for this robot is a disadvantage. The inertial characteristics of the pioneer makes the model specially sensitive to changes in the parameters. For this reason, it can be seen that sample populations did not characterized well the contact point velocities. Figure A.2 shows that the true value is not even in the space spanned by the samples.

When comparing the PGAS and IPEM methodologies for this robot, it can be seen that the latter stands out. Figure A.3 shows that despite of PGAS residuals are less spread, they are not centred at zero, in general. Thus, error in the positioning summarized in Tables A.1 and A.2 is expected. This outcome indicates that the employed slippage model is highly sensitive to changes in the parameters for small sized vehicles.

TABLE A.1: Accumulated mean squared error of the robot position for the 10 trajectories

Traj.	Pose MSE [m]				
	Uncalibrated	Calibrated IPEM	% Improvement	Calibrated PGAS	% Improvement
1	0.877	0.875	0.207	1.434	-63.487
2	1.146	1.146	-0.061	1.210	-5.580
3	0.954	0.964	-1.032	1.399	-46.694
4	0.746	0.742	0.478	1.151	-54.310
5	0.843	0.761	9.798	1.431	-69.759
6	0.892	0.810	9.155	1.373	-53.983
7	0.815	0.768	5.806	1.338	-64.166
8	0.856	0.841	1.836	1.259	-47.043
9	0.762	0.670	11.969	1.045	-37.208
10	0.834	0.838	-0.485	1.391	-66.794

TABLE A.2: Accumulated mean squared error of the robot orientation for the 10 trajectories

Traj.	Attitude MSE [deg]				
	Uncalibrated	Calibrated IPEM	% Improvement	Calibrated PGAS	% Improvement
1	5.236	0.285	94.565	0.387	92.609
2	5.347	0.167	96.870	0.367	93.144
3	4.204	0.401	90.471	0.341	91.885
4	5.505	0.160	97.090	0.515	90.642
5	12.378	0.576	95.348	0.495	96.001
6	9.203	0.175	98.099	0.514	94.416
7	10.486	0.098	99.067	0.498	95.249
8	12.021	0.461	96.164	0.475	96.052
9	11.736	0.144	98.770	0.187	98.403
10	11.792	0.441	96.260	0.548	95.349

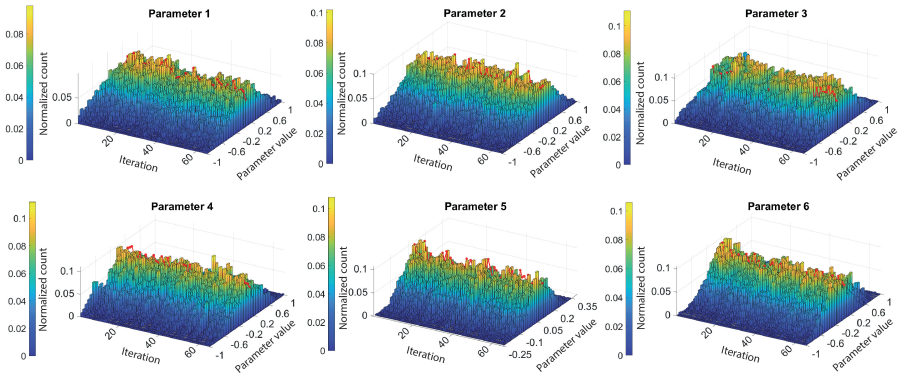

(A)

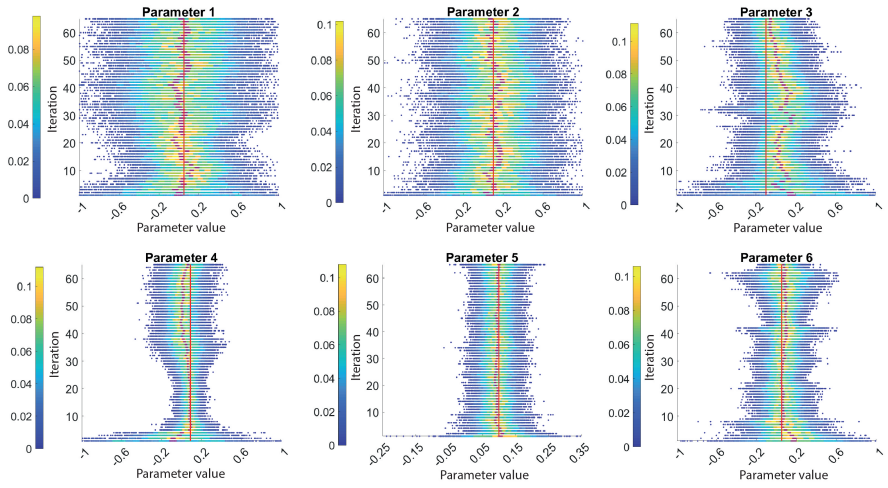

(B)

FIGURE A.1: Evolution of the histograms (A) and sample population (B) generated after processing each measurement batch (iteration) for one trajectory. Bars and samples are coloured according to their likelihood with higher values associated with a yellowish hue. The red trace in the top of each histogram corresponds to the real value of the parameter. The red line in the second row depicts the true value of the parameter, and the purple regions highlighted in each image illustrates a 95% confidence interval.

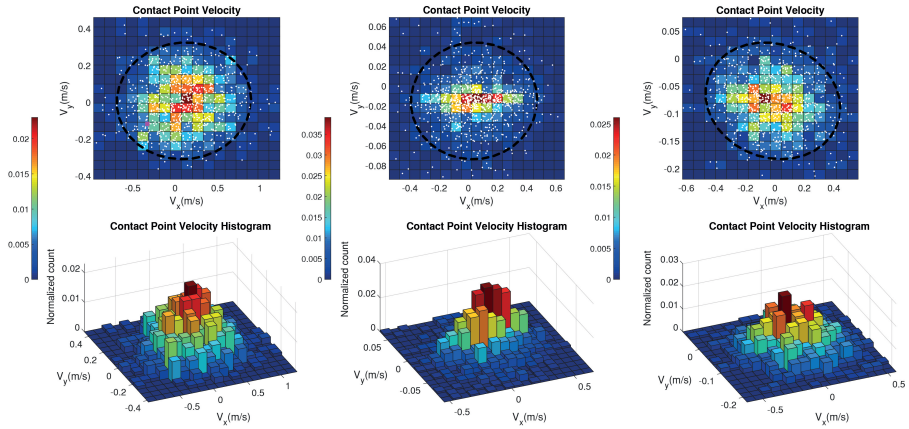

(A)

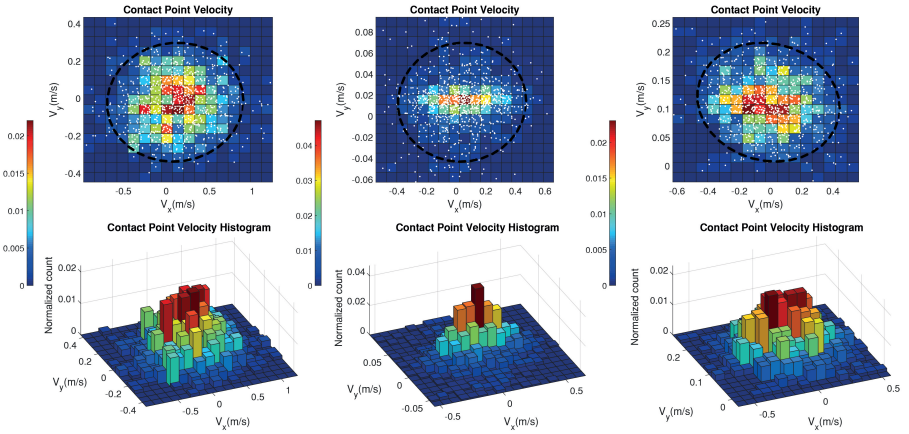

(B)

FIGURE A.2: Approximations of the contact point velocities distributions for the front left (A) and back left (B) wheels of the pioneer in a single trajectory. Each row corresponds to the samples generated at the beginning, middle and ending of the trajectory, respectively. The dashed ellipse depicts a 90% confidence region and the red cross indicates the true velocities. The white dots correspond to samples generated during the calibration process. Bars and cells are coloured according to their normalized likelihood.

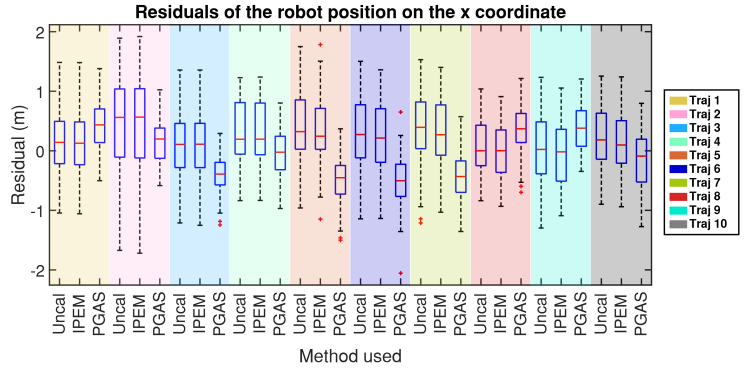

(A)

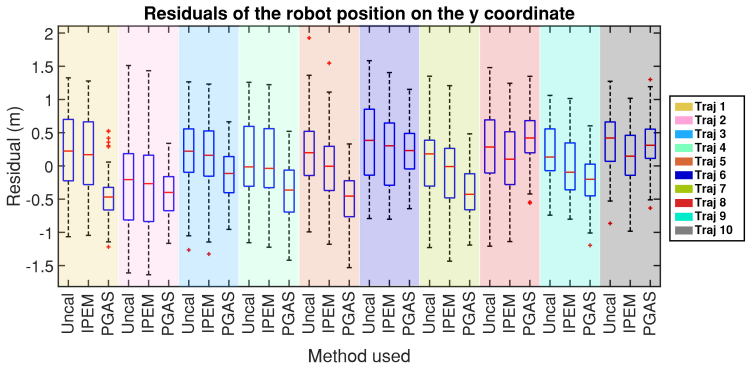

(B)

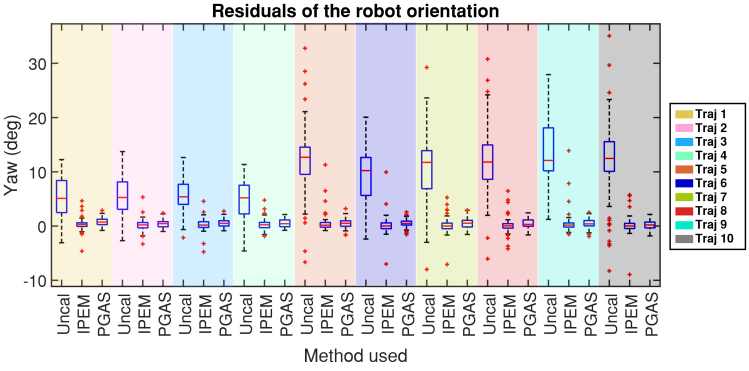

(C)

FIGURE A.3: Boxplots of the residuals for the 2D position of the pioneer in 10 trajectories. Coordinates x (A), y (B) and the robot attitude (C) are depicted. IPEM and PGAS methods outperformed the uncalibrated positioning, with a better performance of IPEM, when driving on a single terrain.

Appendix B

Simulation Results for the Pioneer 3AT Robot - Multiple Terrains

Results of multiple terrain tests for the pioneer robot are summarized in this Appendix. Figure B.1 provides a extended insight about the samples that approximate the parameter posterior distribution. Almost all of them are widely spread in the interval $[-1, 1]$ (except for p_5), which indicates that the PGAS methodology could not properly identify the model. Furthermore, similarly to the single terrain tests with this robot, the samples of the contact point velocities for front and rear wheels were not representative. In general, the real values of the c.p.v. lie outside the regions where the samples are distributed (Figures B.2 and B.3).

The comparison with the IPEM algorithm reveals a lower performance of PGAS also in this test case. In Fig. B.4 can be observed that residuals obtained using PGAS estimates do not contain the zero in the first and third quartiles, for most of the trajectories. Thus, a increased error in the positioning is expected for the PGAS method when compared with the others. However, the robot orientation results present a better performance for PGAS. It is important to note that this outcome was fairly similar for all the test cases and both robots. A closer review of the parameter estimations reveals that p_5 was always correctly determined when using PGAS. Then, it can be inferred that p_5 is the dominating term in the parametrization of the angular slip velocity (Eq. 4.40). Finally, Tables B.1 and B.2 shows the accumulated errors in positioning and attitude of the robot, which agree with the previous discussion.

TABLE B.1: Accumulated mean squared error of the robot position for the 10 trajectories

Traj.	Pose MSE [m]				
	Uncalibrated	Calibrated IPEM	% Improvement	Calibrated PGAS	% Improvement
1	0.945	0.917	2.981	1.180	-24.774
2	0.797	0.792	0.685	1.012	-26.941
3	1.028	1.050	-2.140	1.066	-3.741
4	0.990	0.968	2.152	1.243	-25.599
5	1.021	1.041	-1.931	1.137	-11.275
6	0.974	0.948	2.651	1.007	-3.359
7	0.969	0.965	0.479	1.204	-24.216
8	0.859	0.856	0.362	1.185	-37.875
9	0.990	0.950	4.063	1.281	-29.364
10	1.124	1.078	4.157	1.324	-17.785

TABLE B.2: Accumulated mean squared error of the robot orientation for the 10 trajectories

Traj.	Attitude MSE [deg]				
	Uncalibrated	Calibrated IPEM	% Improvement	Calibrated PGAS	% Improvement
1	6.363	4.135	35.013	0.503	92.100
2	8.470	5.235	38.200	0.401	95.262
3	8.675	5.104	41.164	0.478	94.486
4	8.888	5.541	37.663	0.389	95.628
5	7.985	5.335	33.187	0.515	93.554
6	8.944	5.761	35.587	0.582	93.495
7	8.788	5.547	36.883	0.452	94.862
8	9.002	5.214	42.080	0.552	93.866
9	9.478	6.149	35.121	0.471	95.025
10	9.173	5.547	39.528	0.545	94.057

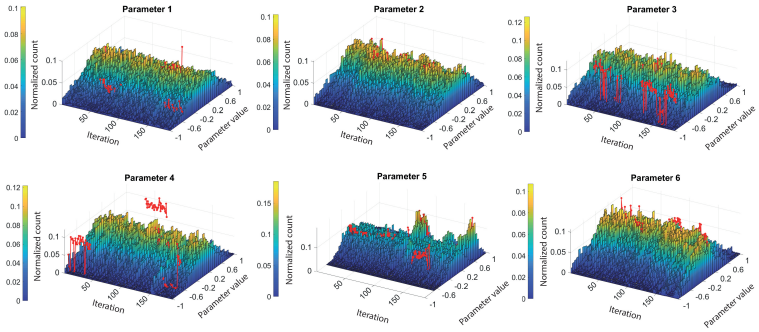

(A)

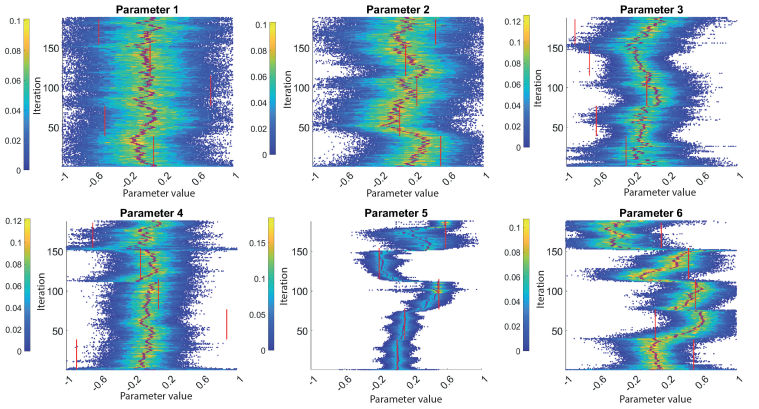

(B)

FIGURE B.1: Evolution of the histograms (A) and sample population (B) generated after processing each measurement batch (iteration) for one trajectory. Bars and samples are coloured according to their likelihood with higher values associated with a yellowish hue. The red trace in the top of each histogram corresponds to the real value of the parameter. The red line in the second row depicts the true value of the parameter, and the purple regions highlighted in each image illustrates a 95% confidence interval.

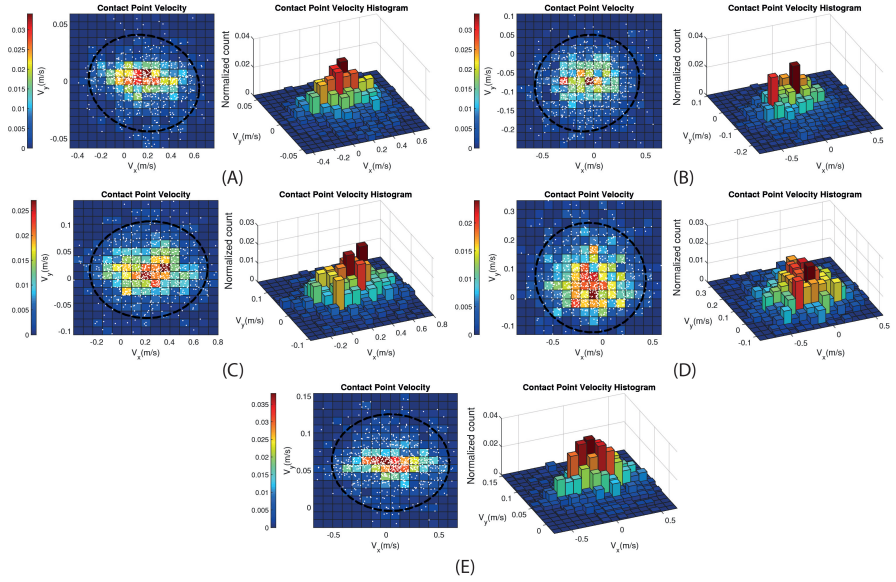

FIGURE B.2: Approximations of the contact point velocities distributions for the front left wheel of the robot during transitions $P^1 - P^2$(B), $P^2 - P^3$(C), $P^3 - P^4$(D), $P^4 - P^5$(E) and at the end of the trajectory. The dashed ellipse depicts a 90% confidence region and the red cross indicates the true velocities. The white dots correspond to samples generated during the calibration process. Bars and cells are coloured according to their normalized likelihood.

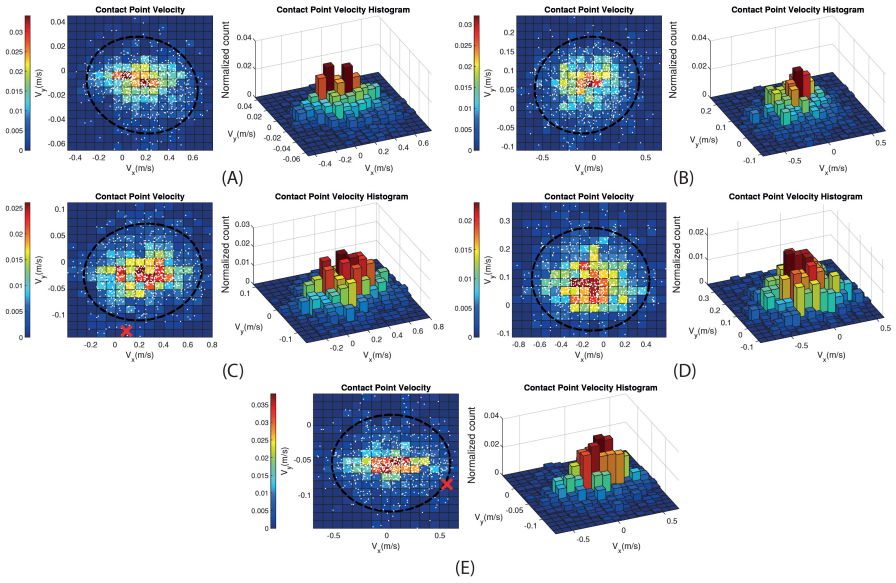

FIGURE B.3: Approximations of the contact point velocities distributions for the rear left wheel of the robot during transitions $P^1 - P^2$(B), $P^2 - P^3$(C), $P^3 - P^4$(D), $P^4 - P^5$(E) and at the end of the trajectory. The dashed ellipse depicts a 90% confidence region and the red cross indicates the true velocities. The white dots correspond to samples generated during the calibration process. Bars and cells are coloured according to their normalized likelihood.

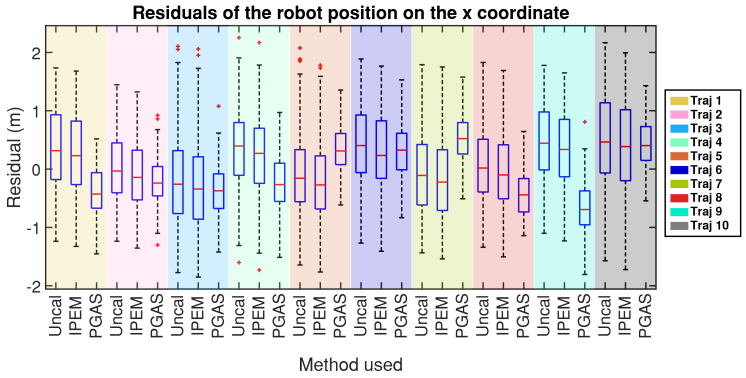

(A)

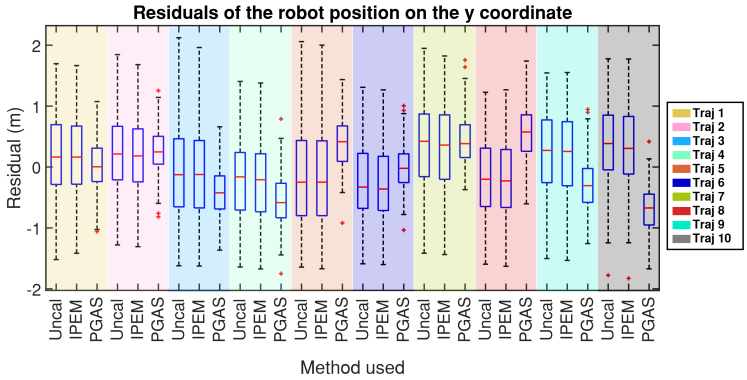

(B)

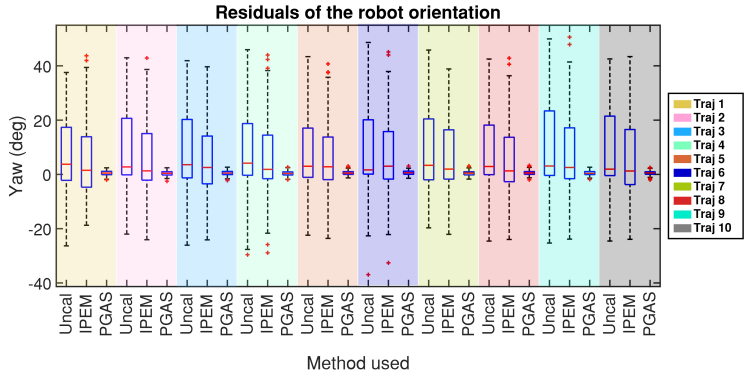

(C)

FIGURE B.4: Boxplots of the residuals for the 2D position of the pioneer in 10 trajectories. Coordinates x (A), y (B) and the robot attitude (C) are depicted. IPEM and PGAS methods outperformed the uncalibrated positioning, with a better performance of IPEM, when driving on a single terrain.

Bibliography

AghaKouchak, A. et al. (2015). "Remote sensing of drought: Progress, challenges and opportunities". In: *Reviews of Geophysics* 53.2, pp. 452–480. ISSN: 19449208. DOI: 10.1002/2014RG000456.

Aguilar, Wilbert G and Stephanie G Morales (2016). "3D Environment Mapping Using the Kinect V2 and Path Planning Based on RRT Algorithms". In: *Electronics* 5.4, pp. 70–87. DOI: 10.3390/electronics5040070.

Alenyà, G., B. Dellen, and C. Torras (2011). "3D modelling of leaves from color and ToF data for robotized plant measuring". In: *IEEE International Conference on Robotics and Automation*, pp. 3408–3414.

Allouis, Tristan et al. (2013). "Stem volume and above-ground biomass estimation of individual pine trees from LiDAR data: Contribution of full-waveform signals". In: *IEEE Journal of Selected Topics in Applied Earth Observations and Remote Sensing* 6.2, pp. 924–934. ISSN: 19391404. DOI: 10.1109/JSTARS.2012.2211863.

Andrieu, Christophe, Arnaud Doucet, and Roman Holenstein (2010). "Particle Markov chain Monte Carlo methods". In: *Journal of the Royal Statistical Society* 72.3, pp. 269–342.

Andrieu, Christophe et al. (2003). "An Introduction to MCMC for Machine Learning". In: *Machine Learning* 50.1, pp. 5–43.

Andújar, Dionisio et al. (2013). "Potential of a terrestrial LiDAR-based system to characterise weed vegetation in maize crops". In: *Computers and Electronics in Agriculture* 92, pp. 11–15.

Andújar, Dionisio et al. (2016). "Using depth cameras to extract structural parameters to assess the growth state and yield of cauliflower crops". In: *Computers and Electronics in Agriculture* 122, pp. 67–73.

Angelova, Anelia et al. (2007). "Learning and Prediction of Slip from Visual Information". In: *Journal of Field Robotics* 24.3, pp. 205–231. ISSN: 15564959. DOI: 10.1002/rob.20179.

Antonelli, Gianluca, Stefano Chiaverini, and Giuseppe Fusco (2005). "A Calibration Method for Odometry of Mobile Robots Based on the Least-Squares Technique : Theory". In: *IEEE Transactions on Robotics* 21.5, pp. 994–1004.

Arnal Barbedo, Jayme Garcia Vieira Koenigkan, Luciano and Thiago Teixeira Santos (2016). "Identifying multiple plant diseases using digital image processing". In: *Biosystems Engineering* 147, pp. 104–116. ISSN: 15375110. DOI: 10.1016/j.biosystemseng.2016.03.012.

Arriagada Pfeiffer, Sebastián et al. (2018). "Mechatronic terrestrial LiDAR for canopy porosity and crown surface estimation". In: *Computers and Electronics in Agriculture* 146.January, pp. 104–113. ISSN: 01681699. DOI: 10.1016/j.compag.2018.01.022.

Auat Cheein, Ferando et al. (2015). "Real-time approaches for characterization of fully and partially scanned canopies in groves". In: *Computers and Electronics in Agriculture* 118, pp. 361–371.

Auat Cheein, Fernando A. and Jose Guivant (2014). "SLAM-based incremental convex hull processing approach for treetop volume estimation". In: *Computers and Electronics in Agriculture* 102, pp. 19–30.

Bac, C. Wouter et al. (2014). "Harvesting Robots for High-value Crops: State-of-the-art Review and Challenges Ahead". In: *Journal of Field Robotics* 31.6, pp. 888–911.

Ball, David et al. (2016). "Vision-based Obstacle Detection and Navigation for an Agricultural Robot". In: *Journal of Field Robotics* 33.8, pp. 1107–1130. DOI: 10.1002/rob.

Baluja, Javier et al. (2012). "Assessment of vineyard water status variability by thermal and multispectral imagery using an unmanned aerial vehicle (UAV)". In: *Irrigation Science* 30.6, pp. 511–522. ISSN: 03427188. DOI: 10.1007/s00271-012-0382-9.

Bekker, Mieczylsaw (1956). *Theory of Land Locomotion*. University of Michigan, p. 499.

Ben-Hur, Asa and Jason Weston (2010). "A User's Guide to Support Vector Machines". In: *Data Mining Techniques for the Life Sciences*. Ed. by O Carugo and F Eisenhaber. Humana Press, pp. 223–239.

Benet, B, V Rousseau, and R Lenain (2016). "Fusion between a color camera and a TOF camera to improve traversability of agricultural vehicles". In: *The 6th International Work- shop Applications of Computer Image Analysis and Spectroscopy in Agriculture*.

Bishop, C. M. (2006). *Pattern Recognition and Machine Learning*, p. 738. ISBN: 0387310738. DOI: 10.1117/1.2819119. arXiv: 0-387-31073-8. URL: http://www.library.wisc.edu/selectedtocs/bg0137.pdf.

Brixius, W. (1987). *Traction prediction equations for bias ply tires*.

Brooks, Christopher A. and Karl Iagnemma (2012). "Self-Supervised Terrain Classification for Planetary Surface Exploration Rovers". In: *Journal of Field Robotics* 29.3, pp. 445–468. ISSN: 14746670. DOI: 10.1002/rob.21408.

Brooks, Steve et al. (2011). *Handbook of Markov Chain Monte Carlo*. Chapman and Hall, p. 575.

Broten, Gregory, David MacKay, and Jack Collier (2012). "Probabilistic obstacle detection using 2 1/2 D terrain maps". In: *Proceedings of the 2012 9th Conference on Computer and Robot Vision, CRV 2012*, pp. 17–23. ISBN: 9780769546834. DOI: 10.1109/CRV.2012.10.

Casella, George and Christian P Robert (1994). "Rao-Blackwellization of Sampling Schemes". In: *Boimetrika* 83.1, pp. 81–94.

Chaivivatrakul, Supawadee et al. (2014). "Automatic morphological trait characterization for corn plants via 3D holographic reconstruction". In: *Computers and Electronics in Agriculture* 109, pp. 109–123. ISSN: 01681699. DOI: 10.1016/j.compag.2014.09.005.

Chan, Tony F. and Luminita A. Vese (2001). "Active contours without edges". In: *IEEE Transactions on Image Processing* 10.2, pp. 266–277. ISSN: 10577149. DOI: 10.1109/83.902291.

Chen, Y.a, H.b Zhu, and H.E.c Ozkan (2012). "Development of a variable-rate sprayer with laser scanning sensor to synchronize spray outputs to tree structures". In: *Transactions of the ASABE* 55.3, pp. 773–781. ISSN: 21510032. DOI: 10.13031/2013.41509.

Chéné, Yann et al. (2012). "On the use of depth camera for 3D phenotyping of entire plants". In: *Computers and Electronics in Agriculture* 82, pp. 122–127. ISSN: 01681699.

Chetverikov, Dmitry, Dmitry Stepanov, and Pavel Krsek (2005). "Robust Euclidean alignment of 3D point sets: The trimmed iterative closest point algorithm". In: *Image and Vision Computing* 23.3, pp. 299–309. ISSN: 02628856. DOI: 10.1016/j.imavis.2004.05.007.

Choi, Won Seok et al. (2012). "Fast iterative closest point framework for 3D LIDAR data in intelligent vehicle". In: *IEEE Intelligent Vehicles Symposium, Proceedings*, pp. 1029–1034. ISBN: 9781467321198. DOI: 10.1109/IVS.2012.6232293.

Choset, Howie et al. (2005). *Principles of Robot Motion*, p. 603. ISBN: 0262033275.

Corti, M. et al. (2015). "Use of Spectral and Thermal Imaging Sensors to Monitor Crop Water and Nitrogen Status". In: *Conference on Proximal Sensing Supporting Precision Agriculture*. DOI: 10.3997/2214-4609.201413855.

Coyle, Eric (2010). "Fundamentals and Methods of Terrain Classification Using Proprioceptive Sensors". Doctor of Philosphy Thesis. Florida State University, p. 91.

Cunningham, Chris, Issa Nesnas, and William L Whittaker (2015). "Terrain Traversability Prediction by Imaging Thermal Transients". In: *IEEE International Conference on Robotics and Automation (ICRA)*, pp. 3947–3952. ISBN: 9781479969234.

Cunningham, Christopher and William L Whittaker (2017). "Improving Slip Prediction on Mars Using Thermal Inertia Measurements". In: *Autonomous Robots*, pp. 1–19.

DaMatta, Fábio M. and José D. Cochicho Ramalho (2006). "Impacts of drought and temperature stress on coffee physiology and production: A review". In: *Brazilian Journal of Plant Physiology* 18.1, pp. 55–81. ISSN: 16770420. DOI: 10.1590/S1677-04202006000100006.

De Cubber, Geert and Haris Balta (2015). "Terrain Traversability Analysis using full-scale 3D Processing". In: *Proceeding of 8th IARP Workshop on Robotics for Risky Environments,* pp. 3–6.

Dempster, A., N. Larid, and D. Rubin (1977). "Maximum Likelihood from Incomplete Data via the EM Algorithm". In: *Journal of the Royal Statistical Society* 39.1, pp. 1–38.

Deventer, Heidi van et al. (2015). "Reducing Leaf-Level Hyperspectral Data to 22 Components of Biochemical and Biophysical Bands Optimizes Tree Species Discrimination". In: *IEEE Journal of Selected Topics in Applied Earth Observations and Remote Sensing* 8.6, pp. 3161–3171. ISSN: 21511535. DOI: 10.1109/JSTARS.2015.2424594.

Doucet, Arnaud and Adam Johansen (2009). "A Tutorial on Particle Filtering and Smoothing: Fifteen years later". In: *The Oxford Handbook of Nonlinear Filtering*. 12. John Wiley and Sons, pp. 656–704.

Du, Lin et al. (2016). "Estimation of rice leaf nitrogen contents based on hyperspectral LIDAR". In: *International Journal of Applied Earth Observations and Geoinformation* 44, pp. 136–143. ISSN: 0303-2434. DOI: 10.1016/j.jag.2015.08.008.

Eitel, Jan U H et al. (2014). "LiDAR based biomass and crop nitrogen estimates for rapid, non-destructive assessment of wheat nitrogen status". In: *Field Crops Research* 159, pp. 21–32. ISSN: 03784290. DOI: 10.1016/j.fcr.2014.01.008.

Elfiky, Noha M et al. (2015). "Automation of dormant pruning in specialty crop production: An adaptive framework for automatic reconstruction and modeling of apple trees". In: *IEEE Computer Society Conference on Computer Vision and Pattern Recognition Workshops*. Vol. 2015-Octob, pp. 65–73. ISBN: 9781467367592. DOI: 10.1109/CVPRW.2015.7301298.

Elseberg, Jan et al. (2012). "Comparison of nearest-neighbor-search strategies and implementations for efficient shape registration". In: *Journal of Software Engineering for Robotics (JOSER)* 3.1, pp. 2–12. ISSN: 2035-3928.

Escolà, A. et al. (2013). "Variable rate sprayer. Part 1 - Orchard prototype: Design, implementation and validation". In: *Computers and Electronics in Agriculture* 95, pp. 122–135. ISSN: 01681699. DOI: 10.1016/j.compag.2013.02.004.

Escolà, Alexandre et al. (2011). "Performance of an ultrasonic ranging sensor in apple tree canopies". In: *Sensors* 11.3, pp. 2459–2477. ISSN: 14248220. DOI: 10.3390/s110302459.

Fankhauser, Peter, Michael Bloesch, and Diego Rodriguez (2015). "Kinect v2 for Mobile Robot Navigation : Evaluation and Modeling". In: *International Conference on Advanced Robotics (ICAR)*, pp. 388–394.

Fawcett, Tom (2006). "An introduction to ROC analysis". In: *Pattern Recognition Letters* 27.8, pp. 861–874. ISSN: 01678655. DOI: 10.1016/j.patrec.2005.10.010. arXiv: /dx.doi.org/10.1016/j.patrec.2005.10.010 [http:].

Fernandez, Juan Carlos (2010). "Characterization of Surface Roughness of Bare Agricultural Soils Using LIDAR". Doctor of Philosophy Thesis. University of Florida, p. 172.

Fieber, Karolina D et al. (2013). "Analysis of full-waveform LiDAR data for classification of an orange orchard scene". In: *ISPRS Journal of Photogrammetry and Remote Sensing* 82, pp. 63–82. ISSN: 09242716. DOI: 10.1016/j.isprsjprs.2013.05.002.

Fleischmann, Patrick and Karsten Berns (2016). "A Stereo Vision Based Obstacle Detection System for Agricultural Applications". In: *Field and Service Robotics*, pp. 217–231. ISBN: 9783319277004.

Foglia, Mario and Giulio Reina (2006). "Agricultural Robot for Radicchio Harvesting". In: *Journal of Field Robotics* 23.6/7, pp. 363–377. ISSN: 14746670.

Fraser, Andrew. et al. (2003). "Incorporating invariants in mahalanobis distance based classifiers: application to face recognition". In: *Proceedings of the International Joint Conference on Neural Networks, 2003.* Vol. 4, pp. 3118–3123. ISBN: 0-7803-7898-9. DOI: 10.1109/IJCNN.2003.1224070.

Fraundorfer, By Friedrich and Davide Scaramuzza (2012). "Visual Odometry Part II: Matching, Robustness, Optimization, and Applications". In: *IEEE Robotics and Automation Magazine* 19.2, pp. 78–90.

Gal, Yarin (2016). "Uncertainty in Deep Learning". PhD thesis. University of Cambridge, p. 160.

Gil, E. et al. (2013). "Variable rate sprayer. Part 2 - Vineyard prototype: Design, implementation, and validation". In: *Computers and Electronics in Agriculture* 95, pp. 136–150. ISSN: 01681699. DOI: 10.1016/j.compag.2013.02.010.

Golightly, Andrew and Darren Wilkinson (2011). "Bayesian parameter inference for stochastic biochemical network models using particle Markov chain Monte Carlo". In: *Interface Focus* 1.6, pp. 807–820.

Gongal, A. et al. (2015). "Sensors and systems for fruit detection and localization: A review". In: *Computers and Electronics in Agriculture* 116, pp. 8–19. ISSN: 01681699. DOI: 10.1016/j.compag.2015.05.021.

Gongal, A. et al. (2016). "Apple crop-load estimation with over-the-row machine vision system". In: *Computers and Electronics in Agriculture* 120, pp. 26–35. ISSN: 01681699. DOI: 10.1016/j.compag.2015.10.022.

González, Ramón, Alejandro López, and Karl Iagnemma (2017). "Thermal vision , moisture content , and vegetation in the context of off-road mobile robots". In: *Journal of Terramechanics* 70, pp. 35–48. DOI: 10.1016/j.jterra.2017.01.001.

Gonzalez, Ramon et al. (2013). "Control of Off-road Mobile Robots using Visual Odometry and Slip Compensation". In: *Advanced Robotics* 27.11, pp. 893–906.

Graham, Carl and Denis Talay (2013). *Stochastic Simulation and Monte Carlo Methods*. Ed. by P. Glynn and Y. Jan. New York: Springer-Verlag Berlin Heidelberg, p. 260. ISBN: 9783642393624.

Greaves, Heather et al. (2015). "Estimating aboveground biomass and leaf area of low-stature Arctic shrubs with terrestrial LiDAR". In: *Remote Sensing of Environment* 164, pp. 26–35. ISSN: 00344257. DOI: 10.1016/j.rse.2015.02.023.

Guo, Yan et al. (2011). "Optimal Path Planning in Field Based on Taversability Prediction for Mobile Robot". In: *International Conference on Electric Information and Control Engineering*, pp. 536–566. ISBN: 9781424480395.

Häselich, Marcel et al. (2013). "Probabilistic terrain classification in unstructured environments". In: *Robotics and Autonomous Systems*. Vol. 61. 10. Elsevier B.V., pp. 1051–1059.

Hastings, W K (1970). "Monte Carlo Sampling Methods Using Markov Chains and Their Applications". In: *Boimetrika* 57.1, pp. 97–109.

Hegazy, Shawky and Corina Sandu (2013). "Experimental investigation of vehicle mobility using a novel wheel mobility number". In: *Journal of Terramechanics* 50.5-6, pp. 303–310. ISSN: 00224898. DOI: 10.1016/j.jterra.2013.09.005.

Hernández-Aceituno, Javier et al. (2016). "Using Kinect on an Autonomous Vehicle for Outdoors Obstacle Detection". In: *IEEE Sensors* 16.10, pp. 3603–3610.

Hétroy-Wheeler, Franck, Eric Casella, and Dobrina Boltcheva (2016). "Segmentation of tree seedling point clouds into elementary units". In: *International Journal of Remote Sensing* 37.13, pp. 2881–2907.

Hillnhütter, C. et al. (2011). "Remote sensing to detect plant stress induced by Heterodera schachtii and Rhizoctonia solani in sugar beet fields". In: *Field Crops Research* 122.1, pp. 70–77. ISSN: 03784290. DOI: 10.1016/j.fcr.2011.02.007.

Ho, Ken, Thierry Peynot, and Salah Sukkarieh (2013). "A near-to-far non-parametric learning approach for estimating traversability in deformable terrain". In: *IEEE International Conference on Intelligent Robots and Systems*, pp. 2827–2833. ISBN: 9781467363587. DOI: 10.1109/IROS.2013.6696756.

Howard, Ayanna and Homayoun Seraji (2001). "Vision-Based Terrain Characterization and Traversability Assessment". In: *Journal of Robotic Systems* 18.10, pp. 577–587.

Hsu, Chih-Wei and Chih-Jen Lin (2002). "A Comparison of Methods for Multiclass Support Vector Machines". In: *IEEE Transactions on Neural Networks* 13.2, pp. 415–425.

Hwanjo, Yu and Kim Sungchul (2012). "SVM Tutorial - Classification, Regression and Ranking". In: *Handbook of Natural Computing*. Ed. by Grzegorz Rozenberg, Thomas Bäck, and Joost Kok. Springer, Berlin, Heidelberg, pp. 479–506.

Iagnemma, Karl and Steven Dubowsky (2004). *Mobile Robots in Rough Terrain*. Vol. 12. Springer, p. 109. ISBN: 3540221085. DOI: 10.1007/978-3-540-73958-6_2. arXiv: arXiv:1011.1669v3.

Iagnemma, Karl and Chris C. Ward (2009). "Classification-based wheel slip detection and detector fusion for mobile robots on outdoor terrain". In: *Autonomous Robots* 26.1, pp. 33–46. ISSN: 09295593. DOI: 10.1007/s10514-008-9105-8.

Iagnemma, Karl et al. (2004). "Online terrain parameter estimation for wheeled mobile robots with application to planetary rovers". In: *IEEE Transactions on Robotics* 20.5, pp. 921–927. ISSN: 15523098. DOI: 10.1109/TRO.2004.829462.

Ishigami, Genya, Gaurav Kewlani, and Karl Iagnemma (2009). "Predictable mobility". In: *IEEE Robotics and Automation Magazine* 16.4, pp. 61–70. ISSN: 10709932. DOI: 10.1109/MRA.2009.934823.

— (2010). "Statistical mobility prediction for planetary surface exploration rovers in uncertain terrain". In: *Proceedings - IEEE International Conference on Robotics and Automation*, pp. 588–593. ISSN: 10504729.

Ishigami, Genya et al. (2007). "Terramechanics-Based Model for Steering Maneuver of Planetary Exploration Rovers on Loose Soil". In: *Journal of Field Robotics* 24.3, pp. 233–250. ISSN: 14746670. DOI: 10.1002/rob. arXiv: 10.1.1.91.5767.

Jay, Sylvain et al. (2015). "In-field crop row phenotyping from 3D modeling performed using Structure from Motion". In: *Computers and Electronics in Agriculture* 110, pp. 70–77. ISSN: 01681699. DOI: 10.1016/j.compag.2014.09.021.

Ji, Wei et al. (2012). "Automatic recognition vision system guided for apple harvesting robot". In: *Computers and Electrical Engineering* 38.5, pp. 1186–1195. ISSN: 00457906. DOI: 10.1016/j.compeleceng.2011.11.005.

Jones, Hamlyn G et al. (2009). "Thermal infrared imaging of crop canopies for the remote diagnosis and quantification of plant responses to water stress in the field". In: *Functional Plant Biology* 36, pp. 978–989.

Kankare, Ville et al. (2013). "Individual tree biomass estimation using terrestrial laser scanning". In: *ISPRS Journal of Photogrammetry and Remote Sensing* 75, pp. 64–75. ISSN: 09242716. DOI: 10.1016/j.isprsjprs.2012.10.003.

Karkee, Manoj et al. (2014). "Identification of pruning branches in tall spindle apple trees for automated pruning". In: *Computers and Electronics in Agriculture* 103, pp. 127–135. ISSN: 01681699. DOI: 10.1016/j.compag.2014.02.013.

Kazmi, Wajahat, Sergi Foix, and Guillem Alenyà (2012). "Plant Leaf Imaging Using Time of Flight CameraUnder Sunlight, Shadowand Room Conditions". In: *IEEE International Symposiumon Robotic and Sensors Environments*, pp. 192–197. ISBN: 9781467327060.

Kazmi, Wajahat et al. (2014). "Indoor and outdoor depth imaging of leaves with time-of-flight and stereo vision sensors: Analysis and comparison". In: *ISPRS Journal of Photogrammetry and Remote Sensing* 88, pp. 128–146. ISSN: 09242716. DOI: 10.1016/j.isprsjprs.2013.11.012.

Kecman, V (2005). *Support Vector Machines: Theory and Applications*. Ed. by Lipo Wang. 1st ed. Springer-Verlag Berlin Heidelberg, p. 431. ISBN: 9783540243885.

Kim, Jayoung and Jihong Lee (2013). "Real-time estimation of maximum friction and optimal slip ratio based on material identification for a mobile robot on rough terrain". In: *International Conference on Control, Automation and Systems (ICCAS 2013)*, pp. 1708–1713. ISBN: 9788993215052. DOI: 10.1109/ICCAS.2013.6704210.

— (2018). "Traction-energy balancing adaptive control with slip optimization for wheeled robots on rough terrain". In: *Cognitive Systems Research* 49, pp. 142–156. ISSN: 1389-0417. DOI: 10.1016/j.cogsys.2018.01.007. URL: https://doi.org/10.1016/j.cogsys.2018.01.007.

Koenig, Kristina et al. (2015). "Comparative classification analysis of post-harvest growth detection from terrestrial LiDAR point clouds in precision agriculture". In: *ISPRS Journal of Photogrammetry and Remote Sensing* 104, pp. 112–125.

Kroese, Dirk P, Thomas Taimre, and Zdravko Botev (2011). *Handbook of Monte Carlo Methods*. 1st ed. New York: John Wiley and Sons, p. 743. ISBN: 9780470177938.

Kross, Angela et al. (2015). "Satellite and in situ derived corn and soybean biomass and leaf area index: Response to controlled tile drainage under varying weather conditions". In: *Agricultural Water Management* 160, pp. 118–131. ISSN: 18732283. DOI: 10.1016/j.agwat.2015.06.007.

Lachat, E. et al. (2015). "First experiences with kinect V2 sensor for close range 3D modelling". In: *International Archives of the Photogrammetry, Remote Sensing and Spatial Information Sciences - ISPRS Archives* 40.5W4, pp. 93–100. ISSN: 16821750. DOI: 10.5194/isprsarchives-XL-5-W4-93-2015.

Laible, Stefan, Yasir Niaz Khan, and Andreas Zell (2013). "Terrain Classification With Conditional Random Fields on Fused 3D LIDAR and Camera Data". In: *European Conference on Mobile Robots (ECMR)*, pp. 172–177. ISBN: 9781479902637.

Lau, Daniel (2013). *The Science Behind Kinects or Kinect 1.0 versus 2.0*. URL: http://www.gamasutra.com/blogs/DanielLau/20131127/205820/ (visited on 06/20/2003).

Lee, Taehee, Joongyou Shirr, and Dongil Cho (2009). "Position estimation for mobile robot using in-plane 3-axis IMU and active beacon". In: *IEEE International Symposium on Industrial Electronics*, pp. 1956–1961. ISBN: 9781424443499. DOI: 10.1109/ISIE.2009.5214363.

Leung, Thomas and Jitendra Malik (2001). "Representing and Recognizing the Visual Appearance of Materials using Three-dimensional Textons". In: *International Journal of Computer Vision* 43.1, pp. 29–44.

Li, Dawei et al. (2015). "Digitization and visualization of greenhouse tomato plants in indoor environments". In: *Sensors* 15.2, pp. 4019–4051. ISSN: 14248220. DOI: 10.3390/s150204019.

Li, Jiangbo et al. (2016a). "Multispectral detection of skin defects of bi-colored peaches based on vis-NIR hyperspectral imaging". In: *Postharvest Biology and*

Technology 112, pp. 121–133. ISSN: 09255214. DOI: 10.1016/j.postharvbio.2015.10.007.

Li, Stan Z. (2009). *Markov Random Field Modeling in Image Analysis - Third Edition*, p. 372. ISBN: 9780874216561. DOI: 10.1007/s13398-014-0173-7.2. arXiv: arXiv:1011.1669v3.

Li, Wang et al. (2016b). "Remote estimation of canopy height and aboveground biomass of maize using high-resolution stereo images from a low-cost unmanned aerial vehicle system". In: *Ecological Indicators* 67, pp. 637–648. ISSN: 1470160X. DOI: 10.1016/j.ecolind.2016.03.036.

Lin, Yi (2015). "LiDAR: An important tool for next-generation phenotyping technology of high potential for plant phenomics?" In: *Computers and Electronics in Agriculture* 119, pp. 61–73. ISSN: 01681699.

Lindsten, Fredrik (2013). "Particle filters and Markov chains for learning of dynamical systems". MA thesis. Linköping University, p. 254.

Lindsten, Fredrik, Michael Jordan, and Thomas Schön (2014). "Particle Gibbs with Ancestor Sampling". In: *Journal of Machine Learning Research* 15, pp. 2145–2184.

Lindsten, Fredrik and Thomas Schön (2013). "Backward Simulation Methods for Monte Carlo Statistical Inference". In: *Foundations and Trends in Machine Learning* 6.1, pp. 1–143. DOI: 10.1561/2200000045.

Lindsten, Fredrik, Thomas B Schön, and Michael I Jordan (2013). "Bayesian semiparametric Wiener system identification". In: *Automatica* 49.7, pp. 2053–2063. ISSN: 0005-1098. DOI: 10.1016/j.automatica.2013.03.021. URL: http://dx.doi.org/10.1016/j.automatica.2013.03.021.

Livny, Yotam et al. (2010). "Automatic reconstruction of tree skeletal structures from point clouds". In: *ACM Transactions on Graphics* 29.6, p. 1. ISSN: 07300301. DOI: 10.1145/1882261.1866177.

Marinello, F. et al. (2015). "Application of the Kinect sensor for dynamic soil surface characterization". In: *Precision Agriculture* 16.6, pp. 601–612.

Martinelli, Federico et al. (2015). "Advanced methods of plant disease detection. A review". In: *Agronomy for Sustainable Development* 35.1, pp. 1–25. ISSN: 17730155. DOI: 10.1007/s13593-014-0246-1.

Marzband, Mousa et al. (2017). "An optimal energy management system for islanded microgrids based on multiperiod artificial bee colony combined with Markov chain". In: *IEEE Systems* 11.3, pp. 1712–1722.

Meng, Xiangrui et al. (2018). "A terrain description method for traversability analysis based on elevation grid map". In: *International Journal of Advanced Robotic Systems* 15.1, pp. 1–12. DOI: 10.1177/1729881417751530.

Metropolis, Nicholas et al. (1953). "Equation of State Calculations by Fast Computing Machines". In: *The Journal of Chemical Physics* 21.6, pp. 1087–1091. DOI: 10.1063/1.1699114.

Milellla, Analissa, Giulio Reina, and James Underwood (2015). "A Self-learning Framework for Statistical Ground Classification using Radar and Monocular Vision". In: *Journal of Field Robotics* 32.1, pp. 20–41. DOI: 10.1002/rob.

Miller, Jordan, Justin Morgenroth, and Christopher Gomez (2015). "3D modelling of individual trees using a handheld camera: Accuracy of height, diameter and

volume estimates". In: *Urban Forestry and Urban Greening* 14.4, pp. 932–940. ISSN: 16108167. DOI: 10.1016/j.ufug.2015.09.001.

Mora, Marco et al. (2016). "Automated computation of leaf area index from fruit trees using improved image processing algorithms applied to canopy cover digital photograpies". In: *Computers and Electronics in Agriculture* 123, pp. 195–202. ISSN: 01681699. DOI: 10.1016/j.compag.2016.02.011.

Mountrakis, Giorgos, Jungho Im, and Caesar Ogole (2010). "Support vector machines in remote sensing : A review". In: *ISPRS Journal of Photogrammetry and Remote Sensing* 1.315, pp. 1–13. ISSN: 0924-2716. DOI: 10.1016/j.isprsjprs.2010.11.001. URL: http://dx.doi.org/10.1016/j.isprsjprs.2010.11.001.

Mulla, David J. (2013). "Twenty five years of remote sensing in precision agriculture: Key advances and remaining knowledge gaps". In: *Biosystems Engineering* 114.4, pp. 358–371. ISSN: 15375110. DOI: 10.1016/j.biosystemseng.2012.08.009.

Muller, Urs A et al. (2013). "Real-time adaptive off-road vehicle navigation and terrain classification". In: *Unmanned Systems Technology XV*, pp. 1–19. DOI: 10.1117/12.2015533.

Næsset, Erik (2009). "Effects of different sensors, flying altitudes, and pulse repetition frequencies on forest canopy metrics and biophysical stand properties derived from small-footprint airborne laser data". In: *Remote Sensing of Environment* 113.1, pp. 148–159. ISSN: 00344257. DOI: 10.1016/j.rse.2008.09.001.

Nielsen, Michael, David C. Slaughter, and Chris Gliever (2012). "Vision-based 3D peach tree reconstruction for automated blossom thinning". In: *IEEE Transactions on Industrial Informatics* 8.1, pp. 188–196. ISSN: 15513203. DOI: 10.1109/TII.2011.2166780.

Nordh, Jerker et al. (2015). "Particle filtering based identification for autonomous non-linear ODE models". In: *17th IFAC Symposium on System Identification SYSID*. Elsevier B.V., pp. 415–420. DOI: 10.1016/j.ifacol.2015.12.163. URL: http://dx.doi.org/10.1016/j.ifacol.2015.12.163.

Nuske, Stephen et al. (2014). "Automated Visual Yield Estimation in Vineyards". In: *Journal of Field Robotics* 31.5, pp. 837–860. DOI: 10.1002/10.. arXiv: 10.1.1.91.5767.

Okamoto, Hiroshi and Won Suk Lee (2009). "Green citrus detection using hyperspectral imaging". In: *Computers and Electronics in Agriculture* 66.2, pp. 201–208. ISSN: 01681699. DOI: 10.1016/j.compag.2009.02.004.

Ono, Masahiro et al. (2015). "Risk-aware Planetary Rover Operation : Autonomous Terrain Classification and Path Planning". In: *Aerospace Conference*, pp. 1–10. ISBN: 9781479953806.

Oonk, Stephen et al. (2014). "Extended Kalman Filter for Improved Navigation with Fault Awareness". In: *IEEE International Conference on Systems, Man, and Cybernetics*, pp. 2681–2686. ISBN: 9781479938407.

Ordonez, Camilo et al. (2017). "Learning of skid-steered kinematic and dynamic models for motion planning". In: *Robotics and Autonomous Systems* 95, pp. 207–221. ISSN: 0921-8890. DOI: 10.1016/j.robot.2017.05.014. URL: http://dx.doi.org/10.1016/j.robot.2017.05.014.

Otsu, Kyohei et al. (2016). "Autonomous Terrain Classification With Co- and Self-Training Approach". In: *IEEE Robotics and Automation Letters* 1.2, pp. 814–819. ISSN: 2377-3766. DOI: 10.1109/LRA.2016.2525040.

Pacejka, Hans (2005). *Tire and vehicle dynamics*. Elsevier, p. 632.

Palleja, Tomas and Andrew J. Landers (2015). "Real time canopy density estimation using ultrasonic envelope signals in the orchard and vineyard". In: *Computers and Electronics in Agriculture* 115, pp. 108–117. ISSN: 01681699. DOI: 10.1016/j.compag.2015.05.014.

Pforte, Florian, Jörn Selbeck, and Oliver Hensel (2012). "Comparison of two different measurement techniques for automated determination of plum tree canopy cover". In: *Biosystems Engineering* 113.4, pp. 325–333. ISSN: 15375110. DOI: 10.1016/j.biosystemseng.2012.09.014.

Pueschel, Pyare, Glenn Newnham, and Joachim Hill (2014). "Retrieval of gap fraction and effective plant area index from phase-shift terrestrial laser scans". In: *Remote Sensing* 6.3, pp. 2601–2627. ISSN: 20724292. DOI: 10.3390/rs6032601.

Ramos, Sebastian et al. (2017). "Detecting Unexpected Obstacles for Self-Driving Cars : Fusing Deep Learning and Geometric Modeling". In: *IEEE Intelligent Vehicles Symposium*, pp. 1025–1032. ISBN: 9781509048045.

Reina, Giulio, Annalisa Milella, and Rainer Worst (2015). "LIDAR and stereo combination for traversability assessment of off-road robotic vehicles". In: *Robotica* 34, pp. 2823–2841. DOI: 10.1017/S0263574715000442.

Reina, Giulio, James Underwood, and Graham Brooker (2011). "Short-range radar perception in outdoor environments". In: *Lecture Notes in Computer Science (including subseries Lecture Notes in Artificial Intelligence and Lecture Notes in Bioinformatics)*. Vol. 6856 LNAI, pp. 265–276.

Reina, Giulio et al. (2010). "Odometry Correction Using Visual Slip Angle Estimation for Planetary Exploration Rovers". In: *Advanced Robotics* 24.3, pp. 359–385. ISSN: 0169-1864. DOI: 10.1163/016918609X12619993300548.

Reina, Giulio et al. (2016). "Ambient awareness for agricultural robotic vehicles". In: *Biosystems Engineering* 146, pp. 114–132. ISSN: 15375110. DOI: 10.1016/j.biosystemseng.2015.12.010.

Robert, Christian and George Casella (2004). *Monte Carlo Statistical Methods*. 2nd. Springer, p. 645.

Rogers-Marcovitz, Forrest and Alonzo Kelly (2010). "On-line Mobile Robot Model Identification using Integrated Perturbative Dynamics". In: *International Symposium on Experimental Robotics*, pp. 417–431.

Romero, Adriana, Carlo Gatta, and Gustau Camps-valls (2015). "Unsupervised Deep Feature Extraction for Remote Sensing Image Classification". In: *IEEE Transactions on Geoscience and Remote Sensing* 54.3, pp. 1–14. DOI: 10.1109/TGRS.2015.2478379..

Rosell, J. R. and R. Sanz (2012). "A review of methods and applications of the geometric characterization of tree crops in agricultural activities". In: *Computers and Electronics in Agriculture* 81, pp. 124–141. ISSN: 01681699. DOI: 10.1016/j.compag.2011.09.007. URL: http://dx.doi.org/10.1016/j.compag.2011.09.007.

Rosell-Polo, Joan R et al. (2009). "Obtaining the three-dimensional structure of tree orchards from remote 2D terrestrial LIDAR scanning". In: *Agricultural and Forest Meteorology* 149.9, pp. 1505–1515. ISSN: 01681923.

Rosell-Polo, Joan R. et al. (2015). "Advances in Structured Light Sensors Applications in Precision Agriculture and Livestock Farming". In: *Advances in Agronomy* 133, pp. 71–112. ISSN: 00652113.

Ross, Patrick James (2016). "Vision-Based Traversability Estimation in field Environments". Doctor of Philosophy Thesis. Queensland University of Technology.

Salvi, Joaquim et al. (2007). "A review of recent range image registration methods with accuracy evaluation". In: *Image and Vision Computing* 25.5, pp. 578–596. ISSN: 02628856. DOI: 10.1016/j.imavis.2006.05.012.

Santamaría-Navarro, Ángel et al. (2015). "Terrain classification in complex 3D outdoor environments". In: *Journal of Field Robotics* 32.1, pp. 42–60.

Sanz, R. et al. (2013). "Relationship between tree row LIDAR-volume and leaf area density for fruit orchards and vineyards obtained with a LIDAR 3D Dynamic Measurement System". In: *Agricultural and Forest Meteorology* 171-172, pp. 153–162. ISSN: 01681923. DOI: 10.1016/j.agrformet.2012.11.013.

Sanz-Cortiella, Ricardo et al. (2011). "Innovative LIDAR 3D dynamic measurement system to estimate fruit-tree leaf area". In: *Sensors* 11.6, pp. 5769–5791. ISSN: 14248220. DOI: 10.3390/s110605769.

Sarkkä, Simmo (2013). *Bayesian Filtering and Smoothing*. Ed. by D. R. Cox et al. New York: Cambridge University Press, p. 229.

Schmid, Cordelia, Cordelia Schmid, and Cordelia Schmid (2001). "Constructing models for content-based image retrieval". In: *IEEE International Conference on Computer Vision and Pattern Recognition*. Kauai, United States, pp. 11–39.

Schön, Thomas B et al. (2015). "Sequential Monte Carlo Methods for System Identification". In: *17th IFAC Symposium on System Identification SYSID*. Elsevier B.V., pp. 775–786.

Schwiegerling, Jim (2004). *Field Guide to Visual and Ophthalmic Optics*. Ed. by SPIE Press, p. 124.

Seegmiller, Neal and Alonzo Kelly (2016). "High-Fidelity Yet Fast Dynamic Models of Wheeled Mobile Robots". In: *IEEE Transactions on Robotics* 32.3, pp. 614–625. ISSN: 15523098. DOI: 10.1109/TRO.2016.2546310.

Seegmiller, Neal et al. (2013). "Vehicle Model Identification by Integrated Prediction Error Minimization". In: *The International Journal of Robotics Research* 32.8, pp. 912–931.

Seegmiller, Neal A (2014). "Dynamic Model Formulation and Calibration for Wheeled Mobile Robots for Wheeled Mobile Robots". PhD thesis. Carnegie Mellon University, p. 126.

Sekhar Nandi, Chandra, Bipan Tudu, and Chiranjib Koley (2014). "A machine vision-based maturity prediction system for sorting of harvested mangoes". In: *IEEE Transactions on Instrumentation and Measurement* 63.7, pp. 1722–1730. ISSN: 00189456. DOI: 10.1109/TIM.2014.2299527.

Shamrao et al. (2018). "Estimation of terramechanics parameters of wheel-soil interaction model using particle filtering". In: *Journal of Terramechanics* 79, pp. 79–95. ISSN: 0022-4898. DOI: 10.1016/j.jterra.2018.07.003. URL: https://doi.org/10.1016/j.jterra.2018.07.003.

Shneier, Michael et al. (2008). "Learning traversability models for autonomous mobile vehicles". In: *Autonomous Robots* 24.1, pp. 69–86. DOI: 10.1007/s10514-007-9063-6.

Slaughter, David C et al. (2008). "Multispectral Machine Vision Identification of Lettuce and Weed Seedlings for Automated Weed Control". In: *Weed Technology* 22.2, pp. 378–384. DOI: 10.1614/WT-07-104.1.

Smith, William and Huei Peng (2013). "Modeling of wheel – soil interaction over rough terrain using the discrete element method". In: *Journal of Terramechanics* 50.5-6, pp. 277–287. ISSN: 0022-4898. DOI: 10.1016/j.jterra.2013.09.002. URL: http://dx.doi.org/10.1016/j.jterra.2013.09.002.

Sock, Juil et al. (2014). "Probabilistic traversability map building for autonomous navigation". In: *International Conference on Control, Automation and Systems* 1.Iccas, pp. 652–655. ISSN: 15987833. DOI: 10.1109/ICCAS.2014.6987861.

Södeström, Torsten and Petre Stoica (1989). *System Identification*. Prentice Hall, p. 612.

Solin, Arno et al. (2018). "Modeling and Interpolation of the Ambient Magnetic Field by Gaussian Processes". In: *IEEE Transactions on Robotics* 34.4, pp. 1112–1127. arXiv: arXiv:1509.04634v2.

Song, Wenjie et al. (2018). "Lane Detection and Classification for Forward Collision Warning System Based on Stereo Vision". In: *IEEE Sensors* 18.12, pp. 5151–5163.

Song, Xiaojing et al. (2008). "Optical flow-based slip and velocity estimation technique for unmanned skid-steered vehicles". In: *2008 IEEE/RSJ International Conference on Intelligent Robots and Systems, IROS*, pp. 101–106. ISBN: 9781424420582. DOI: 10.1109/IROS.2008.4651025.

Svensgaard, Jesper, Thomas Roitsch, and Svend Christensen (2014). "Development of a Mobile Multispectral Imaging Platform for Precise Field Phenotyping". In: *Agronomy* 4.3, pp. 322–336. ISSN: 2073-4395. DOI: 10.3390/agronomy4030322.

Taheri, Sh et al. (2015). "A technical survey on Terramechanics models for tire-terrain interaction used in modeling and simulation of wheeled vehicles". In: *Journal of Terramechanics* 57, pp. 1–22. ISSN: 00224898. DOI: 10.1016/j.jterra.2014.08.003.

Thrun, Sebastian et al. (2006). "Stanley : The Robot that Won the DARPA Grand Challenge". In: *Journal of Field Robotics* 23.9, pp. 661–692. DOI: 10.1002/rob.

Tierney, Luke (1994). "Markov Chains for Exploring Posterior Distributions". In: *The Annals of Statistics* 22.4, pp. 1701–1762.

Torres-Sánchez, Jorge et al. (2013). "Configuration and Specifications of an Unmanned Aerial Vehicle (UAV) for Early Site Specific Weed Management". In: *PLoS ONE* 8.3. ISSN: 19326203. DOI: 10.1371/journal.pone.0058210.

Tumbo, S. D. et al. (2002). "Investigation of laser and ultrasonic ranging sensors for measurements of citrus canopy volume". In: *Applied Engineering in Agriculture* 18.3, pp. 367–372. ISSN: 08838542.

Varma, M. and Andrew Zisserman (2002). "Classifying Images of Materials: Achieving Viewpoint and Illumination Independence". In: *Lecture notes in computer science*, pp. 255–271. ISSN: 16113349.

Varma, Manik and Andrew Zisserman (2005). "A statistical approach to texture classification from single images". In: *International Journal of Computer Vision* 62.1-2, pp. 61–81. ISSN: 09205691.

Varma, Manik et al. (2009). "A Statistical Approach To Material Classification Using Image Patch Exemplars". In: *IEEE Transcations on Pattern Analysis and Machine Intelligence* 31.11, pp. 2032–2047.

Vitzrabin, Efi and Yael Edan (2016). "Adaptive thresholding with fusion using a RGBD sensor for red sweet-pepper detection". In: *Biosystems Engineering* 146, pp. 45–56. ISSN: 15375110. DOI: 10.1016/j.biosystemseng.2015.12.002.

Wachs, J. P. et al. (2010). "Low and high-level visual feature-based apple detection from multi-modal images". In: *Precision Agriculture* 11.6, pp. 717–735. ISSN: 13852256. DOI: 10.1007/s11119-010-9198-x.

Wakui, Futoshi and Yoshiaki Terumichi (2011). "Three-Dimensional Numerical Simulation of Tire Behavior on Soft Ground". In: *Transactions of the Japan Society of Mechanical Engineers* 77.781, pp. 3264–3277. ISSN: 1881-3046. DOI: 10.1299/kikaic.77.3264.

Wang, Qi et al. (2013). "Automated Crop Yield Estimation for Apple Orchards". In: *International Symposium on Experimental Robotics*, pp. 745–758. ISBN: 978-3-319-00064-0. DOI: 10.1007/978-3-319-00065-7.

Wang, Wangxia, Basia Vinocur, and Arie Altman (2003). "Plant responses to drought, salinity and extreme temperatures: Towards genetic engineering for stress tolerance". In: *Planta* 218.1, pp. 1–14. ISSN: 00320935. DOI: 10.1007/s00425-003-1105-5.

Wang, Weilin and Changying Li (2014). "Size estimation of sweet onions using consumer-grade RGB-depth sensor". In: *Journal of Food Engineering* 142, pp. 153–162. ISSN: 02608774. DOI: 10.1016/j.jfoodeng.2014.06.019.

Weerakkody, W A P and L D B Suriyagoda (2015). "Scientia Horticulturae Estimation of leaf and canopy photosynthesis of pot chrysanthemum and its implication on intensive canopy management". In: *Scientia Horticulturae* 192, pp. 237–243. ISSN: 0304-4238. DOI: 10.1016/j.scienta.2015.05.028.

Wei, Gong et al. (2012). "Multi-wavelength canopy LiDAR for remote sensing of vegetation: Design and system performance". In: *ISPRS Journal of Photogrammetry and Remote Sensing* 69, pp. 1–9. ISSN: 09242716. DOI: 10.1016/j.isprsjprs.2012.02.001.

Weiss, Christian, Holger Frohlich, and Andreas Zell (2006). "Vibration-based Terrain Classification Using Support Vector Machines". In: *2006 IEEE/RSJ International Conference on Intelligent Robots and Systems*, pp. 4429–4434. ISBN: 1-4244-0258-1. DOI: 10.1109/IROS.2006.282076.

Welles, Jon M and Shabtai Cohen (1996). "Canopy structure measurement by gap fraction analysis using commercial instrumentation". In: *Journal of Experimental Botany* 47.9, pp. 1335–1342. ISSN: 0022-0957. DOI: 10.1093/jxb/47.9.1335. URL: https://academic.oup.com/jxb/article-lookup/doi/10.1093/jxb/47.9.1335.

Winkens, Christian, Florian Sattler, and Dietrich Paulus (2017). "Hyperspectral Terrain Classification for Ground Vehicles". In: *International Joint Conference on Computer Vision, Imaging and Computer Graphics Theory and Applications*, pp. 417–424. ISBN: 9789897582264. DOI: 10.5220/0006275404170424.

Wong, J Y and V M Asnani (2008). "Study of the correlation between the performances of lunar vehicle wheels predicted by the Nepean wheeled vehicle performance model and test data". In: *Proceedings of the Institution of Mechanical Engineers, Part D: Journal of Automobile Engineering* 222.11, pp. 1939–1954. ISSN: 0954-4070. DOI: 10.1243/0954407JAUTO811.

Wong, Jo (2001). *Theory of ground Vehicles*. Vol. 53. John Wiley and Sons, p. 523. ISBN: 9788578110796. DOI: 10.1017/CBO9781107415324.004. arXiv: arXiv:1011.1669v3.

Wong, Jo Yo (2010). *Terramechanics and Off-Road Vehicle Engineering*. Ed. by Elsevier. 2nd. Butterworth-Heinemann, p. 463.

Woods, Michael, José Guivant, and Jayanytha Katupitiya (2015). "Terrain Classification and Segmentation using Non-Semantic Range Data". In: *Australasian Conference on Robotics and Automation (ACRA)*. Canberra.

Yandun, Francisco et al. (2016a). "Classifying Agricultural Terrain for Machinery Traversability Purposes". In: *AGRICONTROL 2016: The 5th IFAC Conference on Sensing, Control and Automation for Agriculture*. Elsevier, pp. 457–462.

Yandun, Francisco et al. (2016b). "LiDAR and thermal images fusion for ground-based 3D characterisation of fruit trees". In: *Biosystems Engineering* 151, pp. 479–494. DOI: 10.1016/j.biosystemseng.2016.10.012.

Yandun, Francisco et al. (2017). "A survey of ranging and imaging techniques for precision agriculture phenotyping". In: *IEEE/ASME Transactions on Mechatronics* 22.6, pp. 2428–2439. ISSN: 10834435. DOI: 10.1109/TMECH.2017.2760866.

Yandun, Francisco et al. (2018). "Terrain classification using ToF sensors for the enhancement of agricultural machinery traversability". In: *Journal of Terramechanics* 76, pp. 1–13. ISSN: 00224898. DOI: 10.1016/j.jterra.2017.10.005.

Yang, Ruoyong, Revere Drive, and James O Berger (1998). *A Catalog of Noninformative Priors*. Tech. rep. Duke University, p. 44.

Yu, Hongshan et al. (2014). "Obstacle Classification and 3D Measurement in Unstructured Environments Based on ToF Cameras". In: *Sensors* 14.6, pp. 10753–10782. DOI: 10.3390/s140610753.

Zaman-Allah, M et al. (2015). "Unmanned aerial platform-based multi-spectral imaging for field phenotyping of maize." In: *Plant methods* 11.1, p. 35. ISSN: 1746-4811. DOI: 10.1186/s13007-015-0078-2.

Zarco-Tejada, P. J., V. González-Dugo, and J. A J Berni (2012). "Fluorescence, temperature and narrow-band indices acquired from a UAV platform for water stress detection using a micro-hyperspectral imager and a thermal camera". In: *Remote Sensing of Environment* 117, pp. 322–337. ISSN: 00344257. DOI: 10.1016/j.rse.2011.10.007.

Zeltner, Felix (2016). "Autonomous Terrain Classification Through Unsupervised Learning". Master´s Thesis. Universität Würzburg, p. 52.

Zhao, Chuanyuan, Won Suk Lee, and Dongjian He (2016). "Immature green citrus detection based on colour feature and sum of absolute transformed difference (SATD) using colour images in the citrus grove". In: *Computers and Electronics in Agriculture* 124, pp. 243–253. ISSN: 01681699. DOI: 10.1016/j.compag.2016.04.009.

Zins, Matthieu (2017). "Color Fusion and Super-resolution for Time-of-flight Cameras". PhD thesis. Linkpöing University, p. 88.

Zou, Yuhua et al. (2014). "Comparison of different approaches to visual terrain classification for outdoor mobile robots". In: *Pattern Recognition Letters* 38, pp. 54–62. ISSN: 0167-8655. DOI: 10.1016/j.patrec.2013.11.004. URL: http://dx.doi.org/10.1016/j.patrec.2013.11.004.